

# III-2

Materials Sciences



BL1B

## Terahertz Reflectivity Spectra of Superionic Conductors

T. Awano

Faculty of Engineering, Tohoku Gakuin University, Tagajo 985-8537, Japan

Superionic conductors are solids which have high ionic conductivity as liquids or electrolyte solutions. I have measured their reflectivity spectra at millimeter wave and far-infrared region to investigate motions of mobile and immobile ions [1-7]. Ionic plasmonic feature in energy loss function spectra were observed in millimeter wave region of these superionic conductors.

Terahertz spectral region is the frequency region between vibration and translation motion of the mobile ion. The “attempt mode” of conduction ion were also observed in these superionic crystals. This vibrational mode is directly connected with translational movement of conduction ion. Namely, silver ion surrounded by iodine tetrahedron try to move out at this frequency, c.a.  $20\text{ cm}^{-1}$ .

On the other hand, the attempt mode was not clear in AgI-based superionic conductive glasses. Therefore, precise measurement of reflectivity spectra of these glasses was executed at the new terahertz beam line BL1B.

Reflectivity spectra of  $(\text{AgI})_{0.5}(\text{AgPO}_3)_{0.5}$  glasses and  $(\text{AgI})_{0.75}(\text{Ag}_2\text{MoO}_4)_{0.25}$  glasses were measured by FARIS Martin-Puplett interferometer and QMC InSb hot electron bolometer. The spectral region is suitable for the observation of the attempt mode of silver ion.

Figure 1 shows spectra of four glass samples at room temperature. The attempt mode was observed in #1 sample of each glass. In contrast, #2 samples showed no such absorption at  $20\text{ cm}^{-1}$ . This difference seems to be due to the difference of glass structure. Much AgI-clusters may exist in the #1 glass samples. Characterization of the glass structure is necessary to make it clear.

Proton conductors are interested because of the use in fuel cells. The  $\text{Cs}_2(\text{HSO}_4)(\text{H}_2\text{PO}_4)$  crystal is a newly discovered room temperature proton conductor[8]. It keeps high ionic conductivity once after heating above 380 K. It is interesting to make clear the mechanism of such conductivity dependence by thermal history. Figure 2 shows reflectivity spectra of  $(\text{AgI})_{0.5}(\text{AgPO}_3)_{0.5}$  glasses at room temperature. Anisotropic peaks were observed as shown in the Fig. 2. The measurement of the change of these absorption bands after the heating is underway.

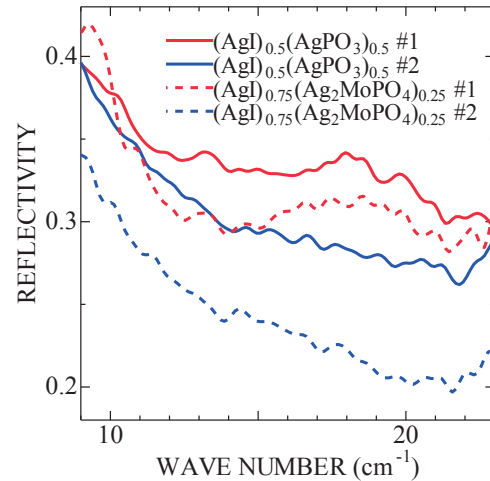


Fig. 1. Reflectivity spectra of  $(\text{AgI})_{0.5}(\text{AgPO}_3)_{0.5}$  and  $(\text{AgI})_{0.75}(\text{Ag}_2\text{MoO}_4)_{0.25}$  glasses.

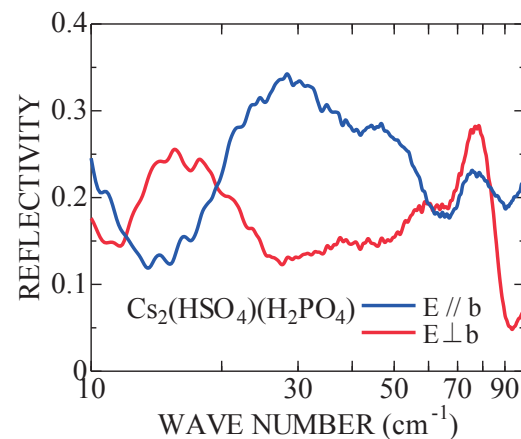


Fig. 2. Reflectivity spectra of  $\text{Cs}_2(\text{HSO}_4)(\text{H}_2\text{PO}_4)$  crystal.

- [1] T. Awano, T. Nanba, M. Ikezawa, T. Matsuyama and H. Yamaoka, *Solid State Ionics* **53-56** (1992) 1269.
- [2] T. Awano, *Infrared Phys. Tech.* **51** (2008) 458.
- [3] T. Awano and T. Takahashi, *J. Phys. Soc. Jpn.* **79** suppl.A (2010) 118.
- [4] T. Awano and T. Takahashi, *Journal of Physics: Conference Series* **148** (2009) 012040.
- [5] T. Awano and T. Takahashi, *Proc. 13<sup>th</sup> Asian Conference on Solis State Ionics*, World Scientific (2012) 569.
- [6] T. Awano, T. Nanba and M. Ikezawa, *UVSOR Activity Report 1992* **20** (1993) 146.
- [7] T. Awano, *UVSOR Activity Report 2011* **39** (2012) 91.
- [8] C. R. I. Chisholm and S.M. Haile, *Acta Cryst.* **B55** (1999) 937.

BL1B

## THz Spectra of Hole-Doped $\text{CeOs}_2\text{Al}_{10}$

H. Takao<sup>1</sup>, S. Kamei<sup>1</sup>, Y. Yamada<sup>2</sup>, J. Kawabata<sup>2</sup>, T. Takabatake<sup>2</sup> and S. Kimura<sup>3,1</sup>

<sup>1</sup>Department of Physics, Osaka University, Toyonaka 560-0043, Japan

<sup>2</sup>ADSM, Hiroshima University, Higashi-Hiroshima 739-8530, Japan

<sup>3</sup>Graduate School of Frontier Biosciences, Osaka University, Suita 565-0871, Japan

Kondo insulators/semiconductors (KIs) are materials with a tiny energy gap at the Fermi level ( $E_F$ ) owing to the hybridization between conduction and localized  $4f$  electrons, namely  $c$ - $f$  hybridization. Because of the strong  $c$ - $f$  hybridization intensity, KIs do not order magnetically by the Ruderman-Kittel-Kasuya-Yosida (RKKY) interaction. However, recently observed KIs,  $\text{Ce}M_2\text{Al}_{10}$  ( $M = \text{Ru}, \text{Os}$ ), have an antiferromagnetic magnetic ordering at the temperature ( $T_0$ ) of about 27 K [1]. Since the ordering temperature is too high compared with that expected from the de Gennes factor [2], another mechanism of the magnetic ordering besides the RKKY interaction is anticipated.

One of such TIs,  $\text{CeOs}_2\text{Al}_{10}$  has a clear energy gap below the photon energy of about 50 meV [3].  $T_0$  of this material is strongly suppressed by the hole doping due to the substitution of Os by Re,  $\text{Ce}(\text{Os}_{1-x}\text{Re}_x)_2\text{Al}_{10}$ , and disappears at  $x = 0.05$  [4]. Then we have investigated the relation of the  $c$ - $f$  hybridization gap to the magnetic ordering using the material of  $x = 0.05$ .

$\text{Ce}M_2\text{Al}_{10}$ s have anisotropic crystal and electronic structures as well as the anisotropic  $c$ - $f$  hybridization intensity [5]. The energy gap owing to the  $c$ - $f$  hybridization clearly appears along the  $c$  axis. Then we measured the temperature-dependent polarized reflectivity [ $R(\omega, T)$ ] spectra of  $x = 0.05$  along the  $c$  axis at the beamline 1B using an automatic measurement system [6].

The obtained  $R(\omega, T)$  spectra divided by that at 80 K in the terahertz region of 3 – 10 meV (0.7 – 2.4 THz) are shown in Fig. 1. Since the spectrum at 80 K is almost unity in this energy region because of its metallic conductivity, the  $R(\omega, T)/R(\omega, 80 \text{ K})$  spectra are nearly equal to  $R(\omega, T)$ . The  $R(\omega, T)$  spectrum strongly depends on temperature in this region. This origin is considered to be the temperature-dependent Drude weight due to carriers excited over an energy gap. This is the evidence of the existence of the energy gap.

The energy gap originates from the  $c$ - $f$  hybridization, which remains at  $x = 0.05$  even though the magnetic ordering disappears. This suggests that the  $c$ - $f$  hybridization is not the sufficient condition for the magnetic ordering. However, in the case of other  $\text{RM}_2\text{Al}_{10}$  ( $R = \text{other rare-earth ions}$ ), which has no  $c$ - $f$  hybridization, magnetic ordering temperature obeys the de Gennes factor indicating the RKKY interaction [2]. Therefore the  $c$ - $f$  hybridization is basically

needed for the appearance of the high ordering temperature  $T_0$ . These facts suggest that the unusual magnetic ordering of  $\text{Ce}M_2\text{Al}_{10}$  does not directly originate from but indirectly relates to the  $c$ - $f$  hybridization.

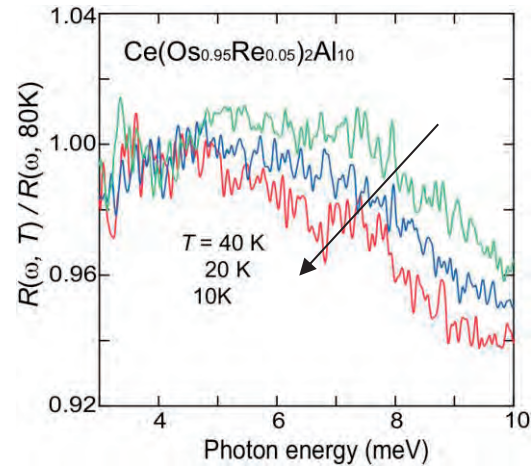


Fig. 1. Temperature dependence of relative reflectivity spectrum of  $\text{Ce}(\text{Os}_{0.95}\text{Re}_{0.05})_2\text{Al}_{10}$  divided by that at 80 K in the photon energy region of 3 – 10 meV (0.7 – 2.4 THz). The observed Drude spectral weight is suppressed with decreasing temperature.

[1] T. Nishioka, Y. Kawamura, T. Takesaka, R. Kobayashi, H. Kato, M. Matsumura, K. Kodama, K. Matsubayashi and Y. Uwatoko, *J. Phys. Soc. Jpn.* **78** (2009) 123705.

[2] Y. Muro, J. Kajino, T. Onimaru and T. Takabatake, *J. Phys. Soc. Jpn.* **80** (2011) SA021.

[3] S. Kimura, T. Iizuka, H. Miyazaki, A. Irizawa, Y. Muro and T. Takabatake, *Phys. Rev. Lett.* **106** (2011) 056404.

[4] J. Kawabata, T. Takabatake, K. Umeo and Y. Muro, *Phys. Rev. B* **89** (2014) 094404.

[5] S. Kimura, Y. Muro and T. Takabatake, *J. Phys. Soc. Jpn.* **80** (2011) 033702.

[6] S. Kimura, *JASCO Report* **50** (2008) 6 [in Japanese].

BL2A

## Local Structure Investigation around P Atom in Ag and Cu Doped Hydroxyapatite

M. Sato<sup>1</sup>, H. Sakaguchi<sup>2</sup>, Y. Inoue<sup>2</sup> and A. Nakahira<sup>2,3</sup>

<sup>1</sup>Institute for Materials Research, Tohoku University, Sendai 980-8577, Japan

<sup>2</sup>Graduate school of Engineering, Osaka Prefecture University, Sakai 599-8531, Japan

<sup>3</sup>Kansai Center for Industrial Materials Research, Tohoku University, Sakai 599-8531, Japan

Hydroxyapatite ( $\text{Ca}_{10}(\text{PO}_4)_6(\text{OH})_2$ , HAp) is a chief inorganics of our hard tissue and it has been widely used in medical field as artificial hard tissue due to its excellent biocompatibility and osteo-conductivity. However, there is the most significant problem of infection during the displacement surgery or after the operation[1]. When such infections occurred, it is necessary to repeat a surgery to replace the alternate implants. This is a significant burden for patient. In order to overcome these problems, imparting the antibacterial property to the implants is expected as one of the efficient method, and the development of alternate materials of hard tissue having antibacterial property have been strongly desired [2]. Therefore, Cu and Ag doped HAp, which are expected having an excellent antibacterial property, has been prepared by hydrothermal technique to prevent some infections during surgery, and the local structure around P atom of these sample was investigated by XAFS measurement at BL-2A in UVSOR.

Ag and Cu doped HAp samples were prepared by 0.1 mol/L  $\text{Ca}(\text{NO}_3)_2$ ,  $(\text{NH}_4)_2\text{HPO}_4$ ,  $\text{CuCl}_2$  and  $\text{AgNO}_3$  solutions, respectively. The Ca/P ratio was fixed at 1.67 and the amount of Ag and Cu changed in the range from 0 mol% to 10 mol% for Ca concentration of HAp. The pH value of each solutions were regulated by ammonia solution and tris buffer solution, respectively. Obtained slurry was filtrated and then dried at 323 K for overnight. The P K-edge XAFS spectra was corrected in BL-2A of UVSOR. The XAFS data of sample was obtained by fluorescence mode using InSb double crystal monochrometer and SDD detector. In a present study, unfortunately, the EXAFS spectra did not obtained due to the influence of absorption of M-edge of Au mesh which is using as an  $I_0$  measurement.

Figure 1 shows P K-edge XANES spectra of Ag-HAp prepared by HT process. The obtained XANES spectra resembled to that of commercial HAp (HAp-200, Taihei Chemical Industrial Co., Ltd.), and the shape of XANES spectra did not change by increasing the Ag ratio. This result indicate that the secondary phase such as silver phosphate does not generate and the local structure around P atom does not changed by Ag addition.

Figure 2 shows P K-edge XANES spectra of Cu-HAp samples prepared by HT process. The P-K edge spectra of sample showed similar spectra to HAp-200 and  $\text{Cu}_3(\text{PO}_4)_2$ . This result means that the added Cu ion exists into HAp structure or forms

$\text{Cu}_3(\text{PO}_4)_2$ . It is thought that since the local structure around P atom in both HAp and  $\text{Cu}_3(\text{PO}_4)_2$  resembles each other, the obtained XANES spectra of HAp-200 and  $\text{Cu}_3(\text{PO}_4)_2$  had similar shape. Therefore, it is difficult to decide that the Cu ion exists into HAp structure or forms  $\text{Cu}_3(\text{PO}_4)_2$  from P-K XANES spectra only. In order to obtain the structural knowledge of Cu-HAp in detail, the measurement in EXAFS region is necessary in a future study. In Ag-L edge measurement, good spectra could not obtain in this measurement period.

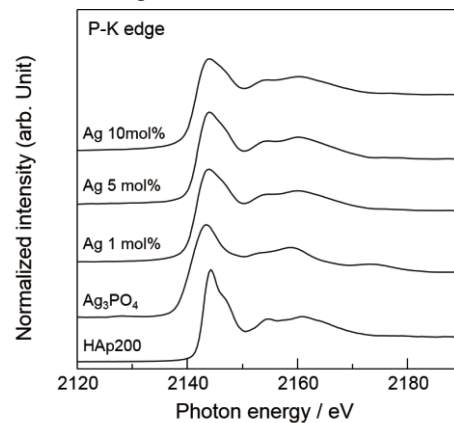


Fig. 1. P K-edge XANES spectra of Ag-HAp samples.

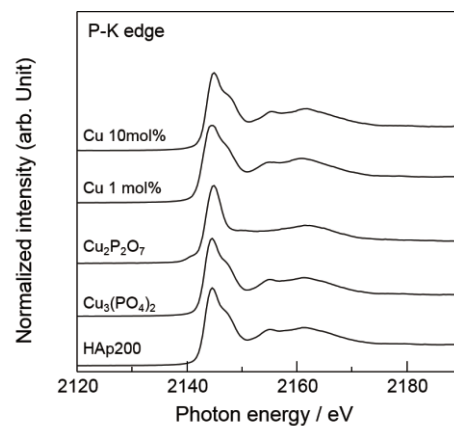


Fig. 2. P K-edge XANES spectra of Cu-HAp samples.

[1] M. Stigter, J. Bezemer, K. de Groot and P. Layrolle, *Journal of Controlled Release* **99** (2004) 127.

[2] L. Zhao, P. K. Chu, Y. Zhang and Z. Wu, *Journal of Biomedical Materials Research Part B: Applied Biomaterials* **91** (2009) 470.

BL2A

## Study of Formation Processes of Active Mo Species over V-Doped Mo/H-AlGaMFI by Mo L<sub>III</sub>-Edge XANES

H. Aritani<sup>1</sup>, S. Mogi<sup>1</sup>, N. Naijo<sup>1</sup>, T. Sugawara<sup>1</sup>, T. Kawai<sup>1</sup> and A. Nakahira<sup>2</sup>

<sup>1</sup>Department of Life Science & Green Chemistry, Saitama Institute of Technology, Fukaya 369-0293 Japan

<sup>2</sup>Graduate School of Engineering, Osaka Prefecture University, Sakai 599-8531 Japan

Mo-modified H-MFI is a typical catalyst for MTB (Methane to Benzene) reaction, *i.e.*, methane dehydroaromatization. Although the MTB reaction is revolutionary for direct conversion of natural gas, deactivation due to coking over the catalyst cannot be avoided during the methane conversion. Clarification of the deactivation process over the catalysts is one of an important point for develop of highly active and durable MTB catalysts. In this study, time course of the formation and activation of active Mo species on H-MFI supports is investigated. The effects of Ga-doping onto MFI (GaAlMFI) support and Mo-V co-doping on GaAlMFI are also studied.

Catalyst samples were prepared by impregnation of each H-GaAlMFI (Si/Al<sub>2</sub>=40) support with MoO<sub>2</sub>(acac)<sub>2</sub>-VO(C<sub>5</sub>H<sub>7</sub>O<sub>2</sub>)<sub>3</sub>-CHCl<sub>3</sub> solution (5wt% as MoO<sub>3</sub>), and followed by dried and calcined at 773 K. GaAlMFI (Al/Ga=50-100) supports were synthesized hydro-thermally at 413 K for a week, and followed by ion-exchanging with NH<sub>4</sub>Cl and calcined at 873 K. The catalytic MTB reactivity was evaluated by means of fixed-bed flow reaction at 1023 K, as described in a separate paper [1]. Mo L<sub>III</sub>-edge XANES spectra were measured in BL2A of UVSOR-IMS in a total-electron yield mode using InSb double-crystal monochromator. Photon energy was calibrated by using Mo metal-foil, and normalized XANES spectra and their derivatives are presented. REX-2000 (Rigaku Co.) software was used by normalization of each XANES spectrum.

Figure 1 shows the XANES spectra of various Mo-V/GaAl-MFI catalysts after MTB reaction for 60 and 200 min. After the reaction for 60 min with highly catalytic activity, the edge energy (shown in Table 1) is almost as same as that of  $\alpha$ -Mo<sub>2</sub>C over the whole catalysts. At the same instant, the white lines peaked at ca. 2524 eV can be shown, indicating the formation excess carbonized Mo species. It suggests the formation of Mo-carbonaceous species in catalytically active state. After the reaction for 200min in deactivated state, the edge energy values over Mo/H-MFI and Mo-V/GaAlMFI, which are highly active and durable catalysts, are almost kept on at ca. 2522 eV. For significantly deactivated catalysts, Mo/GaAl-MFI and Mo-V-H-MFI, the edge energy values are almost as same as that of  $\alpha$ -Mo<sub>2</sub>C. Indeed, the Mo-V/GaAlMFI is the most highly active and durable catalyst for MTB, which is the least amount of deposited carbonaceous species analyzed by thermogravimetry. In contrast, Mo/H-MFI (V- and

Ga-free) catalysts show high activity only an initial state, and large amount of deposited carbonaceous species are shown over the catalysts. It is concluded that Both Ga-doping onto H-MFI and V-doping with Mo bring about the high and durable activity for MTB reaction by way of stable Mo-carbonaceous species without carbon deposition.

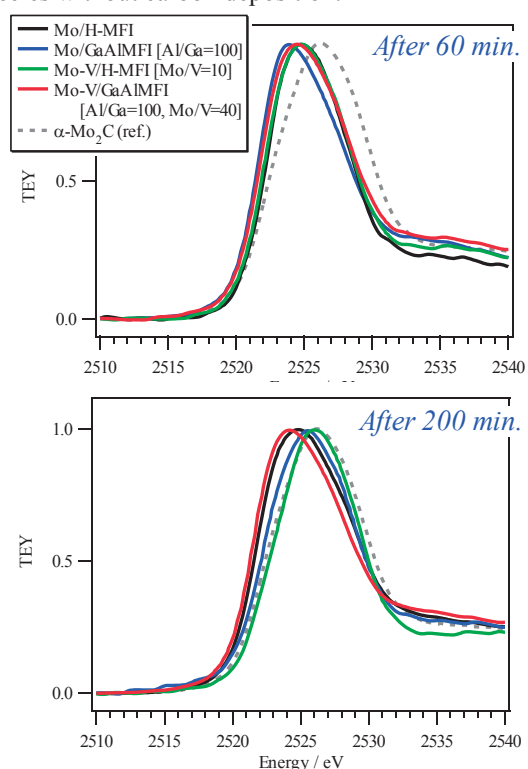


Fig. 1. Mo L<sub>III</sub>-edge XANES of Mo-V/H-GaAlMFI catalysts after MTB reaction for 60 (top) and 200 (bottom) minutes at 1023 K.

Table 1. Edge energy value of the catalysts after MTB reaction for 60/200 min.

Catalyst	Time / min.	Edge Energy / eV
Mo/H-MFI40	60	2522.63
	200	2521.75
Mo/Ga(100)Al-MFI40	60	2521.75
	200	2522.35
Mo-V(10)/H-MFI40	60	2521.98
	200	2523.52
Mo-V(40)/Ga(100)Al-MFI40	60	2521.87
	200	2521.65
$\alpha$ -Mo <sub>2</sub> C		2522.13

[1] H. Aritani, H. Shibasaki, H. Orihara and A. Nakahira, J. Environm. Sci. **21** (2009) 736.

BL2A

## Local Environment Analysis of Mg Ions Doped in CaZrO<sub>3</sub>:Tb

H. Fukaya<sup>1</sup>, Y. Kubo<sup>1</sup> and T. Yamamoto<sup>1,2</sup>

<sup>1</sup>Faculty of Science and Engineering, Waseda University, Tokyo 169-8555, Japan

<sup>2</sup>Institute of Condensed-Matter Science, Waseda University, Tokyo 169-8555, Japan

Phosphor is a very attractive material in the combined use of the light emitting device (LED) and then a lot of researches have been already carried out for this material. One of the common strategies to synthesize stable phosphors for the industrial applications is the doping of the rare-earth ions in the matrix oxides. Among these, Tb doped CaZrO<sub>3</sub> was found to show bright green-light emission by UV irradiations [1]. In addition, it was reported that Mg co-doping into this material can increase the brightness of the green-light emission [1]. In order to understand the mechanism of this kind of change in brightness, it is important to know the local environment of doped ions in the matrix oxides. For such purpose, XANES analysis is quite powerful and we could successfully analyze wide variety of functional materials [2, 3]. In the current study, local environment of co-doped Mg ions in CaZrO<sub>3</sub>:Tb is investigated by the X-ray absorption near-edge structure measurements at Mg K-edge.

Mg co-doped CaZrO<sub>3</sub>:Tb was prepared by the conventional solid-state reaction method. Reagent grade CaCO<sub>3</sub>, ZrO<sub>2</sub>, Tb<sub>4</sub>O<sub>7</sub> and MgO powders were used as starting materials. These powders were weighed changing the molar ratio of cations and mixed in an agate mortar. These mixed powders were pressed into cylindrical pellets, which were sintered in air at 1673 K for 6 hrs. Resultant specimens were ground and were provided to photoluminescence measurements. A concentration of the dopants with the most bright luminescence was 0.03 for both Tb and Mg, i.e., CaZr<sub>0.94</sub>Tb<sub>0.03</sub>Mg<sub>0.03</sub>O<sub>3</sub>. This sample was examined by the XRD measurements, which showed its crystal structure is single-phased and orthorhombic perovskite structure without any precipitates.

Mg-K XANES spectra of Mg co-doped CaZrO<sub>3</sub>:Tb, MgO and Mg(OH)<sub>2</sub> were observed at BL2A in UVSOR by total electron yield method. The incident beam was monochromatized with a beryl (10T0) (2d = 15.965 Å) double crystal monochromator. Sample powders were put on the carbon adhesive tape, which are attached on the first Cu-Be dinode of the electron multiplier.

Observed Mg-K XANES spectra of Mg co-doped CaZrO<sub>3</sub>:Tb (CaZr<sub>0.94</sub>Tb<sub>0.03</sub>Mg<sub>0.03</sub>O<sub>3</sub>) is shown in Fig. 1 together with those of MgO and Mg(OH)<sub>2</sub>. Mg-K XANES profile of the Mg co-doped CaZrO<sub>3</sub>:Tb shows similar one as that of MgO, but is quite different from that of Mg(OH)<sub>2</sub>. From this comparison, it is suggested that the local environment of Mg ions in Mg co-doped CaZrO<sub>3</sub>:Tb is similar to that in MgO, which is the 6-coordination of oxygen

ions. Such environment exists in CaZrO<sub>3</sub> as Zr<sup>4+</sup> site. Finally, we could determine the local environment of Mg ions in CaZrO<sub>3</sub>:Tb by the Mg-K XANES analysis.

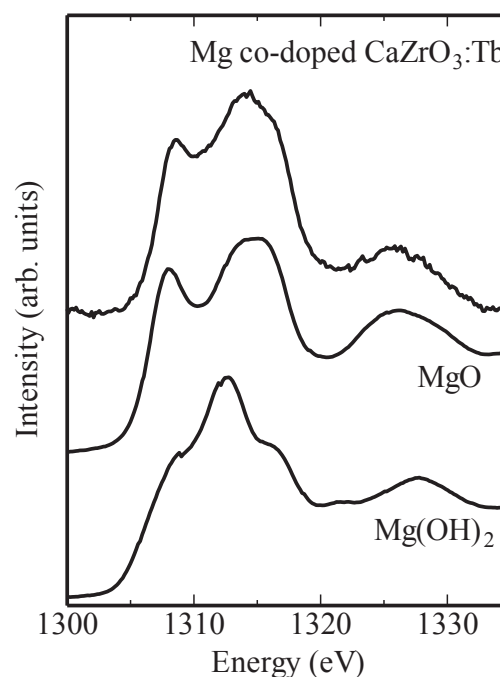


Fig. 1. Mg-K XANES spectra of Mg co-doped CaZrO<sub>3</sub>:Tb, MgO and Mg(OH)<sub>2</sub>.

- [1] Y. Shimizu *et al.*, Mater. Sci. Eng. B **161** (2009) 100.
- [2] T. Yamamoto, *et al.*, J. Phys.: Condens. Matter **21** (2009) 104211.
- [3] I. Tanaka *et al.*, J. Am. Cer. Soc. **88** (2005) 2013.

BL2A

## Local Structure Analysis of the Charge-Discharge Process for Conversion Reaction of the Binary Metal Oxide Containing Aluminum Ion by XAFS Measurement

N. Sonoyama<sup>1</sup>, Y. Ogasawara<sup>1</sup>, T. Mizuno<sup>1</sup> and T. Tukada<sup>2</sup>

<sup>1</sup>Graduate School of Engineering Science, Nagoya Institute of Technology, Nagoya, 466-8555, Japan

<sup>2</sup>Nagoya Institute of Technology Institute for Molecular Science, Okazaki 444-8585, Japan

Tarascon et al. reported that 3d transition metal oxides (MO, where M is Fe, Co, Ni, and Cu etc.) nanoparticles could reversibly react with lithium to achieve high theoretic capacities as high as 700 mAh g<sup>-1</sup> in 2000 [1–4]. The mechanism of the “conversion reaction” involves the formation and decomposition of Li<sub>2</sub>O accompanied by a large amount of lithium ion reaction toward metal oxide nano particles. In this study, we have investigated the electrochemical reaction of Al<sup>3+</sup> ion doped NiO which was synthesized using layered double hydroxide as a precursor by ex-situ XAFS measurement.

The solid solution of multiple metal oxides, Al<sup>III</sup> dissolved NiO was prepared according to the method mentioned in the previous papers [9,10]. The ratio of divalent metal and other valent metals (Ni<sup>2+</sup>:Al<sup>3+</sup>) is 2:1 otherwise noted. X-ray absorption spectroscopy measurements were performed at the BL-2 in UV-SOR under the vacuum condition. Measurements are carried out by fluorescence method and photoelectric yield method. The electrochemical reacted samples are removed from the cell and rinsed with dimethyl carbonate and set in transfer vessel.

In Fig. 1, XANES spectra of as prepared Ni-Al oxide comparing with alumina power and aluminum foil. The absorption edge of as prepared Al-Ni oxide appeared at lower energy region than alumina power. This would be brought by the crystal structure of Ni-Al oxide.

In Fig. 2, XANES spectra of Ni-Al oxide reduced by discharging until 30 mV. The XANES spectrum of Ni-Al oxide hardly changed in comparison with pristine sample. This result is inconsistent with the increased capacity by aluminum introduction. This suggests that the reduction of aluminum ion is limited, not until metal state.

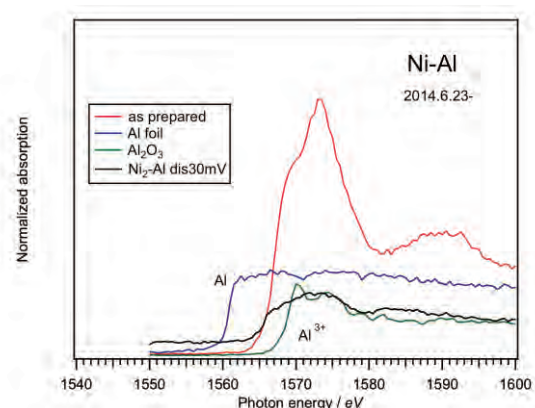


Fig. 1. Al k edge XANES spectra of as prepared Al-Ni oxide, Al foil and alumina.

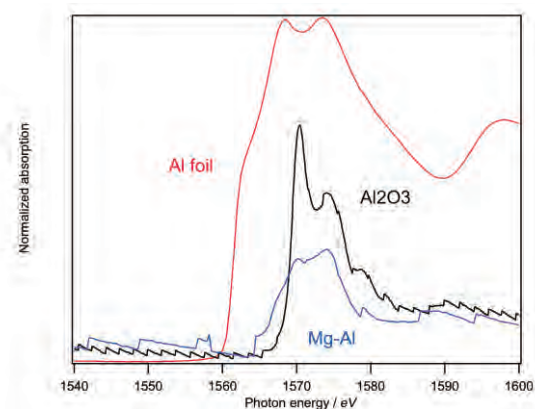


Fig. 2. Al k edge XANES spectra of as prepared Al-Ni oxide and reduced one.

- [1] P. Poizot, S. Laruelle, S. Grugeon, L. Dupont and J. Tarascon, *Ionics* **6** (2000) 321.
- [2] P. Poizot, S. Laruelle, S. Grugeon, L. Dupont and J.-M. Tarascon, *Nature* **407** (2000) 496.
- [3] S. Grugeon, S. Laruelle, R. Herrera-Urbina, L. Dupont, P. Poizot and J. M. Tarascon, *J. Electrochem. Soc.* **148** (2001) A285.
- [4] S. Laruelle, S. Grugeon, P. Poizot, M. Dollé L. Dupont and J.-M. Tarascon, *J. Electrochem. Soc.* **149** (2002) A627.

BL2A

## Evaluation of Local Structure of Si for Perlite Synthesized from Natural Mineral

A. Nakahira<sup>1,2</sup>, S. Togo<sup>1</sup>, M. Kasai<sup>1,3</sup>, Y. Kobayashi<sup>3</sup>, T. Morinaga<sup>1</sup>, Y. Inoue<sup>1</sup>,  
M. Sato<sup>4</sup> and H. Aritani<sup>5</sup>

<sup>1</sup>Faculty of Engineering, Osaka Prefecture University, Sakai 599-8531, Japan

<sup>2</sup>Osaka Center, IMR, Tohoku University, Sakai 599-8531, Japan

<sup>3</sup>Mitsui Mining & Smelting Co., Ltd., Perlite Division, Tokyo 141-8584, Japan

<sup>4</sup>Institute of Materials Research, Tohoku University, Sendai 980-8577, Japan

<sup>5</sup>Saitama Institute of Technology, Fukaya 369-0293, Japan

In general, perlite is considered to be a volcanic glass typically formed by the hydration of obsidian. Therefore, perlite minerals have a relatively high water content and soften by heat-treatments on rotary kiln furnace around the temperatures range of 1000 °C. Since on the heat-treatments water trapped in the perlite structure is vaporized, the rapid foam phenomena for perlite material arise. As a consequence, inorganic foam materials with unique porous-structures are easily produced in large amounts. Perlite is one of most versatile natural products. Large amounts of porous foam with amorphous structure is commercially useful for its significantly light weight and low thermal conductivity due to the unique porous structure and its compositions. These perlites are used in a lot of commercial fields as lightweight plasters, mortar, concrete, tiles and thermal insulation materials. In special, the large amounts of consumption of LNG leads to the construction of LNG tanks and consequently the usage of perlite for heat insulation in LNG tanks rapidly increase. Furthermore, the recycle of waste material from perlite insulator in LNG tanks emerges as a severe problem in Japan and other countries.

In order to solve the recycle of perlite waste after insulator usage, we have continued to develop the efficient use of perlite wastes. For example, perlite wastes may be used for a silica source for inorganic materials and ceramics like silica, mullite, zeolite, glass and so on.

In this study, we attempted to investigate the structure for naturally perlite products. However, perlite has amorphous structures and the detailed characterization of perlite microstructures are insufficiently carried out. In special, the relations of perlite structure and synthetic parameter for useful ceramics are not well clarified.

Powders of natural perlite ore were prepared by the crushers and the ball-milling process before the rotary heat-treatments from natural ore minerals. Several perlite powders were prepared for rotary heat-treatments. Perlite powders were thrown into the heat-treatment furnace at 1073K to 1273K under air atmosphere. Foamed perlites were crashed by ball-milling and aligned to some grades of average

particle size.

Obtained products were characterized by XRD method, FT-IR and TG-DTA. The microstructures of products were observed by SEM. The local structures around Si for the obtained products were characterized by measuring X-ray adsorption near edge structure (XANES) at BL02A in UV-SOR.

Various foamed perlite powders were synthesized though heat-treatments at 1073 to 1273K in air atmosphere. The evaluation of XRD for foamed perlite powders was done. XRD results showed that foam products obtained from perlite powders were amorphous. Figure 1 shows XANES spectra of products and reference materials. As shown in Fig. 1, XANES spectra of sample obtained the same spectra as amorphous silica gel. These results suggest that LTA products obtained from perlite possess the same local structure of Si for commercial amorphous silica gel.

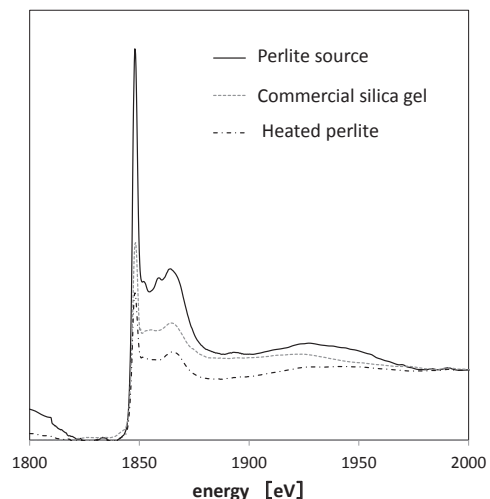


Fig. 1. Si XANES spectra of perlite and reference materials: product and silica gel.

BL2A

## XANES Analysis of Methylene Blue Adsorbed on WO<sub>3</sub> Nanomaterials

T. Yoshida<sup>1</sup>, K. Komori<sup>2</sup>, M. Yamamoto<sup>2</sup>, C. Tsukada<sup>2</sup>, S. Yagi<sup>1</sup>, M. Yajima<sup>2</sup>, S. Kajita<sup>1</sup> and N. Ohno<sup>2</sup>

<sup>1</sup>EcoTopia Science Institute, Nagoya University, Nagoya 464-8603, Japan

<sup>2</sup>Graduate School of Engineering, Nagoya University, Nagoya 464-8603, Japan

Recently, formation of dendritic nanostructures was found on W surface by He plasma irradiation in certain plasma conditions [1]. We have applied the dendritic nanostructured W to a photocatalyst which can mineralize the organic compounds in water or atmosphere under light irradiation.

In our previous research, we partially oxidized the surface of the nanostructured W and obtained a nanostructured WO<sub>3</sub>/W composite material. The material showed photocatalytic decolorization reaction of methylene blue (MB: C<sub>16</sub>H<sub>18</sub>ClN<sub>3</sub>S nH<sub>2</sub>O, n≈3) aqueous solution under near infrared light irradiation. However, we should confirm whether MB decolorization reflects the photoinduced mineralization of MB molecules or the sensitization effect of MB adsorbed on WO<sub>3</sub>/W composite material. Therefore, in the present study, we investigate the chemical state of MB molecules after photoinduced reaction by XAFS measurements.

The dendritic nanostructure was fabricated by He plasma irradiation to a monocrystal W plate. After the plasma irradiation, the surface of the sample was partially oxidized on exposure to air at room temperature. We prepared two samples in this manner through the oxidation for 90 days, and the surface oxidation ratios (*x*) of the samples were estimated by XPS measurements as 70 %. Another two samples with *x* =100 % were prepared by further heat-treatment at 773 K for 2 hour in air. These samples are referred to as WO<sub>3</sub>(*x*)/W.

S K-edge XANES measurements were conducted for the adsorbed species on the surfaces of WO<sub>3</sub>(70)/W and WO<sub>3</sub>(100)/W after photocatalytic decolorization reaction of MB by total electron yield or fluorescence X-ray yield method at BL2A in UVSOR and BL6N1 in Aichi Synchrotron Radiation Center.

Figure 1 shows S K-edge XANES spectra of a MB solid powder and a MB aqueous solution. The peaks at 2471.4 eV and 2473.4 eV are respectively assigned to  $\pi^*(S-C)$  and  $\sigma^*(S-C)$  excitations [2]. Noticeable difference among the two spectra is observed for the  $\pi^*(S-C)$  peak. The XANES spectrum of a MB powder shows a sharp  $\pi^*(S-C)$  peak, because MB molecules in the solid state are stacked each other by the  $\pi-\pi$  interaction [3] to form a high symmetric structure. On the other hand,  $\pi^*(S-C)$  peak is lower in the spectrum of a MB aqueous solution rather than the solid state

Figure 2 shows S K-edge XANES spectra of the surfaces of WO<sub>3</sub>(70)/W and WO<sub>3</sub>(100)/W kept with

MB aqueous solutions under light irradiation or in the dark. The  $\pi^*(S-C)$  peaks for both samples in the dark are much higher than the peak for MB molecule in aqueous solution (Fig. 1). Such characteristic feature of XANES spectra is similar to that of a MB solid powder. Therefore, in the dark reaction, MB molecules would be aggregated and stacked by  $\pi-\pi$  interactions each other. The intensities of  $\pi^*(S-C)$  and  $\sigma^*(S-C)$  peaks decrease by the light irradiation for both samples, indicating the break of S-C bonds of MB molecules adsorbed on the samples. Thus, XANES measurements clearly demonstrate the difference in the chemical state of MB molecules between the photoinduced reaction under NIR light irradiation and the adsorption reaction in the dark.

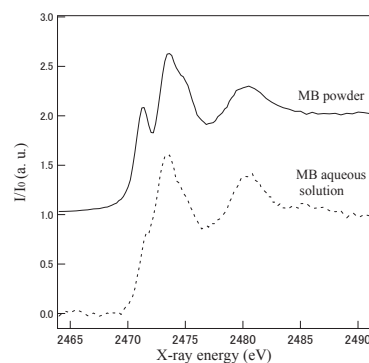


Fig. 1. S K-edge XANES spectra of a MB solid powder and a MB aqueous solution.

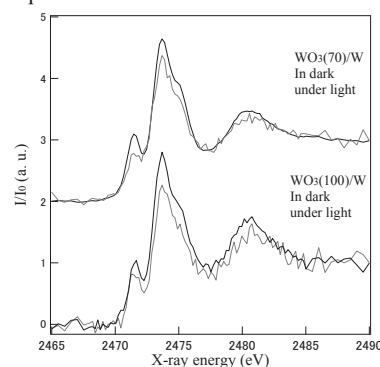


Fig. 2. S K-edge XANES spectra of the MB adsorbates on the surfaces of WO<sub>3</sub>(70)/W and WO<sub>3</sub>(100)/W. These samples were kept with MB aqueous solutions under near infrared light for 225 min (black) or in the dark for 350 min (gray).

[1] S. Takamura, N. Ohno, D. Nishijima and S. Kajita, *J. Plasma Fusion Res.* **1** (2006) 051.

[2] G. N. George *et al.*, *J. Phys. Chem. A* **118** (2014) 7796.

[3] H. E. Marr III and J. M. Stewart, *Acta Cryst.* **B29** (1973) 847.

BL2A

## Local Structure Investigation around P Atom in Mn Substituted LiFePO<sub>4</sub>

M. Sato<sup>1</sup>, M. Togo<sup>2</sup>, Y. Inoue<sup>2</sup> and A. Nakahira<sup>2,3</sup>

<sup>1</sup>Institute for Materials Research, Tohoku University, Sendai 980-8577, Japan

<sup>2</sup>Graduate school of Engineering, Osaka Prefecture University, Sakai 599-8531, Japan

<sup>3</sup>Kansai Center for Industrial Materials Research, Tohoku University, Sakai 599-8531, Japan

Lithium-ion battery has been used in many mobile devices as high performance battery due to its high energy density and repeatable property. However, there are some problems to be overcome such as a stability in harsh environment and a significant cost saving. LiFePO<sub>4</sub> is anticipated as a novel positive electrode material to reduce the materials cost and to exhibit the high thermal stability. Among the 3d transition elements, which are essential for the cathode active material, iron is the one of ideal elements in terms of cost and resources. LiFePO<sub>4</sub> has reversible potential of 3.5 V and theoretical capacity of 170 mAhg<sup>-1</sup>, which are comparable energy density to a bedded salt type LiCoO<sub>2</sub>. The doping of multiply-charged ion and the substitution of foreign element to Fe site are to be a good approach to improve the conductivity and to enhance the electrode potential of LiFePO<sub>4</sub>. In this study, Mn substituted LiFePO<sub>4</sub> was synthesized by hydrothermal process, and the effect of Mn substitution on the local structure around P atom was investigated by XAFS measurement.

LiOH/H<sub>2</sub>O, (NH<sub>4</sub>)<sub>2</sub>HPO<sub>4</sub>, FeSO<sub>4</sub>/7H<sub>2</sub>O and MnSO<sub>4</sub>/5H<sub>2</sub>O were used as starting materials. Each starting materials were weighted to become a molar ratio of Li : P : Fe : Mn = 2 : 1 : 1-x : x (x = 0, 0.25, 0.50, 0.75, 1.0). After measurement, they were put into distilled water in a Teflon vessel and vigorously mixed for a few minutes. Teflon vessel with mixed solution was encapsulated into autoclave and was hydrothermally treated at 473 K for 6 hours. Obtained slurry was filtrated and then dried at 323 K for overnight. The P K-edge XAFS spectra was corrected in BL-2A of UVSOR. The XAFS data of sample was obtained by fluorescence mode using InSb double crystal monochromator and SDD detector. In a present study, unfortunately, the EXAFS spectra did not obtained due to the influence of absorption of M edge of Au mesh which is using as an I<sub>0</sub> measurement.

Figure 1 shows P K-edge XANES spectra of LiMn<sub>x</sub>Fe<sub>1-x</sub>PO<sub>4</sub> (x = 0, 0.25, 0.5, 0.75, 1). Obtained sample had similar XANES spectra to that of commercial LiFePO<sub>4</sub>, and the XANES spectra of sample did not change by Mn addition. These results indicate that the Mn based secondary phase such as MnPO<sub>4</sub> does not generated by Mn addition during a synthesis and the local structure around P atom does not change by Mn substitution.

Figure 2 shows P K-edge XANES spectra of samples after charge-discharge cycle test. The

shoulder was appeared around 2148 eV on the XANES spectra of after 100 cycles, and it was observed more clearly after 1000 cycles. This result indicate the generation of FePO<sub>4</sub> phases and the quantitative increment of FePO<sub>4</sub> phase with increasing the cycles. Therefore, it is suggested that the reaction of eq.1 became difficult to occur by repeating the charge-discharge cycle test.

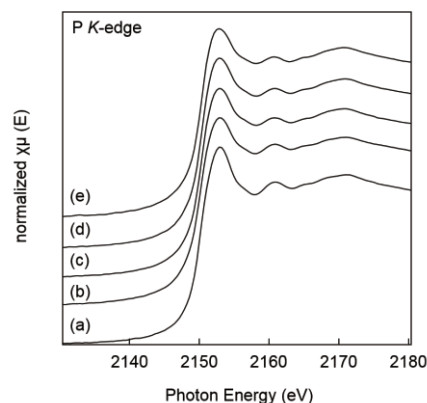
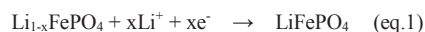


Fig. 1. P K-edge XANES spectra of LiMn<sub>x</sub>Fe<sub>1-x</sub>PO<sub>4</sub> samples prepared by hydrothermal process. (a) x = 0, (b) x = 0.25, (c) x = 0.5, (d) x = 0.75, (e) x = 1.

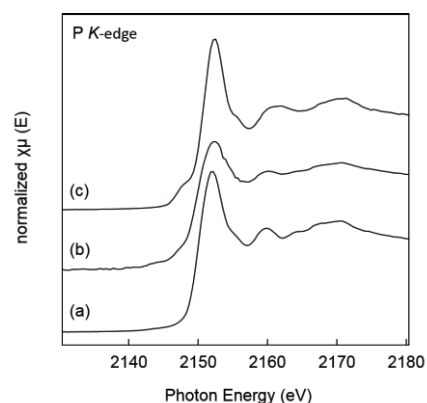


Fig. 2. P K-edge XANES spectra of samples after charge-discharge cycle test. (a) 0 cycle, (b) 100 cycles, (c) 1000 cycles.

[1] Aniruddha Deb *et al.*, J. Synchrotron Rad. **11** (2004) 497.

BL2A

## Structural Evaluation of Local Structure of Si for LTA-Type Zeolite from Perlite Source

A. Nakahira<sup>1,2</sup>, M. Kasai<sup>1,3</sup>, S. Togo<sup>1</sup>, Y. Kobayashi<sup>3</sup> and H. Aritani<sup>4</sup>

<sup>1</sup>Faculty of Engineering, Osaka Prefecture University, Sakai 599-8531, Japan

<sup>2</sup>Osaka Center, IMR, Tohoku University, Sakai 599-8531, Japan

<sup>3</sup>Mitsui Mining & Smelting Co., Ltd., Perlite Division, Tokyo 141-8584, Japan

<sup>4</sup>Saitama Institute of Technology, Fukaya 369-0293, Japan

Perlite is a volcanic glass that is typically formed by the hydration of obsidian. Perlite with a relatively high water content softens at temperatures of 1000 °C and water trapped in the perlite structure of the material vaporizes, leading to the expansion of the material and unique porous-structure. Because perlite has a high water content and amorphous structure, it is commercially applicable to many fields from the advantage of its significantly light weight after foam processing. Many commercial applications for perlite have been developed as lightweight plasters, mortar and concrete, ceiling tiles and insulation materials.

In this study, we attempted to synthesize the zeolite from naturally perlite products. Zeolites have the unique 3D microporous networks. They are one of aluminosilicate minerals commonly used as various commercial adsorbents and other applications in petroleum industry as a catalyst and oxygen purification and water purification. In this experiments, perlite was used for a silica source for zeolite. Especially we focused on LTA-type zeolite with low Si/Al zeolite having unique properties such as high ion exchange capacity, catalytic activity, and sorption ability etc.[1-2] In case of synthesis of zeolite, the microstructure of perlite plays an important role for stability of many zeolite phase. As, however, perlite has amorphous structures, the relations of perlite structure and synthetic parameter for LTA-type zeolite are not well clarified.

Perlite powders were prepared by the ball-milling process for rotary heat-treatments from natural products. Foamed perlites were crashed by ball-milling and aligned to some grades of average particle size. Sodium aluminate (NaAlO<sub>2</sub>) was used as an alumina source and added into perlite powder for the adjustment of Si/Al ratio. Perlite powder and sodium aluminate were mixed in NaOH solution and aged for 6 hours. Then mixed solution was poured into vessel and heated at 363K Hydrothermal synthesis for perlite was carried out at 363K for 24 hours. After hydrothermal treatments under some synthetic conditions, the products were filtered and sufficiently washed with de-ionized water and dried.

Obtained products were characterized by XRD method, FT-IR and TG-DTA. The microstructures of products were observed by SEM. The local structures around Si for the obtained products were characterized by measuring X-ray adsorption near

edge structure (XANES) at BL02A in UV-SOR.

Various zeolites were synthesized though hydrothermal treatment of perlite with alkaline solutions in order to facilitate effective use of the discarded perlite. The evaluation of XRD for products was carried out. XRD results showed that products obtained from perlite powders with 2.5 micron of average particle size were also identified to be LTA type without another phase. These results indicated that the obtained fine-zeolite products were LTA type zeolites. Using perlites powders after the mechanical mixing by ball-milling process monolithic LTA zeolite powders were successfully synthesized by after the mechanical mixing processing for 24 hours.

Figure 1 shows the XANES spectra of products and reference materials. As shown in Fig. 1, XANES spectra of sample obtained the same spectra as the commercial LTA. These results suggest that LTA products obtained from perlite possess the good crystallinity and also the same local structure of Si for commercial LTA.

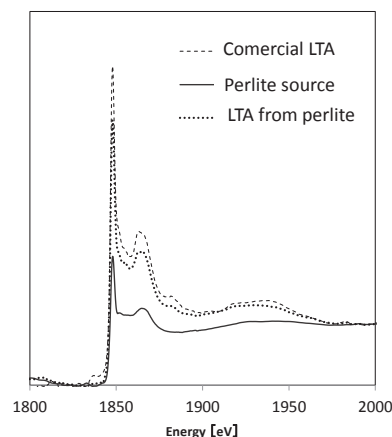


Fig. 1. Si XANES spectra of zeolites and reference materials: perlite, product and commercial LTA.

[1] D. Novembre, B. D.Sabatino, D. Gimeno and C. Pace, "Synthesis and characterization of Na-X, Na-A and Na-P zeolites and hydroxysodalite from metakaolinite", *Clay Minerals* **46** (2011) 339.

[2] G.M. Khan, D.M.Y. Arafat, S.M.S. Razzaque and Md. S. Alam, *Indian Journal of Chemical Technology* **17** (2010) 303.

BL2A

## Studies on Electronic Structure of Aluminum Oxide Thin Film under Voltage Applied Conditions by Near-Edge X-Ray Absorption Fine Structure

E. Kobayashi<sup>1</sup>, K. K. Bando<sup>2</sup>, O. Takahashi<sup>3</sup> and T. Okajima<sup>1</sup>

<sup>1</sup>Kyushu Synchrotron Light Research Center, Tosu 841-0005, Japan

<sup>2</sup>National Institute of Advanced Industrial Science and Technology, Tsukuba 305-8565, Japan

<sup>3</sup>Institute for Sustainable Science and Development, Hiroshima University, Higashi-Hiroshima, 739-8526, Japan

Aluminum oxide is recognized as an important material because it is the prototype of metal oxides and of wide-gap insulator. The aluminum oxide is also used in a wide field of industrial applications such as an insulating material. However, there is no report on the electronic structure of aluminum oxide under voltage applied conditions. Although Al *K*-edge NEXAFS spectra of aluminum oxide have been obtained in total electron yield mode, the method is difficult under voltage applied conditions. Then we have observed an electronic state by detecting x-ray fluorescence from the sample while scanning photon energy.

Al *K*-edge NEXAFS spectra of aluminum oxide thin film were measured at the beamline 2A of the UVSOR in the Institute of Molecular Science. An alumina film was made on a stainless steel plate by dip-coating with a diluted alumina sol (Kawaken Fine Chemicals, F1000). The coated plate was dried at 333 K and calcined at 573 K in an oven. The NEXAFS spectra were obtained using the partial fluorescence yield (PFY) mode at room temperature.

Figure 1 shows the Al *K*-edge NEXAFS spectra of aluminum oxide obtained from PFY mode at various applied voltage. This sample was discharged at 160 V. Two strong peaks are observed at around 1569.3 eV (A) and 1571.8 eV (B), respectively. The spectral features are also similar to the obtained for Gibbsite [1]. The intensity of peak A and peak B change gradually with applied voltage. Figure 2 shows the applied voltage dependence of the intensity of peak A and peak B for aluminum oxide thin film. The intensity of the two peaks tends to become weak with increasing applied voltage and the peaks become broad. This result indicates that the content of an amorphous phase increased in alumina with applied voltage.

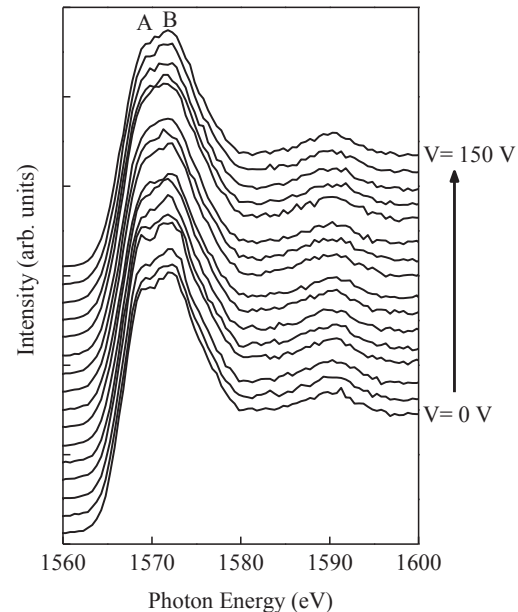


Fig. 1. Al *K*-edge NEXAFS spectra of aluminum oxide thin film obtained from PFY mode at various applied voltage.

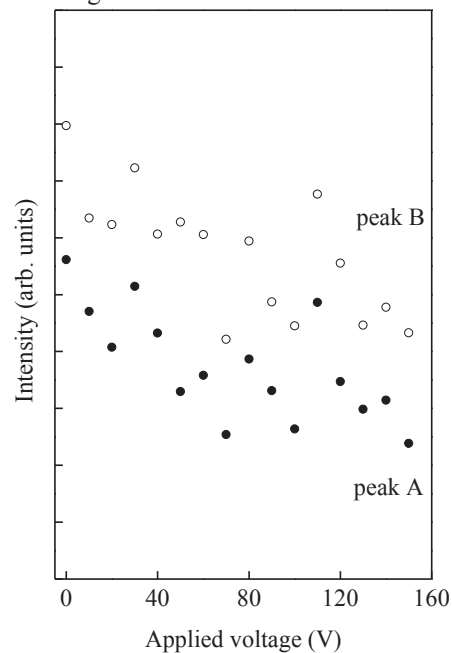


Fig. 2. Applied voltage dependence of the intensity of peak A and peak B for aluminum oxide thin film.

[1] C. S. Doyle *et al.*, *J. Synchrotron Rad.* **6** (1999) 621.

## Temperature Dependence of Self-Trapped Exciton Emission and Energy Transfer in Binary Rare-Earth Borates upon Vacuum UV Excitation

N. Kodama, A. Abe, M. Kudo and T. Takahashi

Graduate School of Engineering and Resource Science, Akita University, Akita 010-8502, Japan

We report the temperature and material dependence of the intrinsic luminescence from self-trapped excitons (STEs) and energy transfer to  $RE^{3+}$  ( $RE^{3+} = Sm^{3+}, Gd^{3+},$  or  $Tb^{3+}$ ) ions observed in three kinds of undoped binary borates  $LaSc_3(BO_3)_4$  (LSB),  $YSc(BO_3)_2$  (YSB), and  $LuSc(BO_3)_2$  (LuSB) under vacuum ultraviolet (VUV) excitation. In addition, we examine the temperature dependence and the dynamics of energy transfer from STEs in  $RE^{3+}$ -doped LSB, YSB, and LuSB samples.

The time-resolved spectra were measured using a pulse with a width of 10 ns from an  $F_2$  pulsed laser operating at 157 nm, and the decay times were determined.

Figures 1(a), 1(b), and 1(c) show the temperature dependence of the luminescence spectra in undoped LSB, YSB, and LuSB, respectively. As can be seen, at 293 K, three, two, and one distinct emission bands were observed for LSB, YSB, and LuSB, respectively, and were located at energies corresponding to the STE bands. The peaks of the STE luminescence bands in all samples (LSB, YSB, LuSB) shifted to longer wavelengths with increasing temperature from 15(or 14) to 293 K.

Figure 2 shows the temperature dependence of the STE intensities for the undoped samples. In the undoped LSB, the STE(I) intensity decreased gradually from 15 to 160 K, and then remained nearly constant. Accompanying this decrease in the STE(I) intensity, the intensities of STE(II) and (III) increased, reached their maxima at 180 K, and then decreased monotonically for higher temperatures. This decrease in the STE(II) and STE(III) intensity likely resulted from a thermal quenching process, such as an intrinsic quenching or a partial energy transfer to nonradiative “killer” centers due to the presence of defects or impurities. Undoped YSB exhibited an STE(I) intensity that increased gradually as the temperature increased to 125 K, above which the intensity decreased. The STE(II) luminescence appeared at 180 K, and the intensity increased with increasing temperature to 293 K. In the undoped LuSB, the intensity of STE(I) passed through a maximum at 200 K, which is similar to the temperature dependence of the STE(II) and STE(III) luminescence for LSB and that of STE(I) for YSB. As the STE(I) emission intensity decreased in LSB and YSB, the STE(II) and STE(III) emission intensity increased, accompanied by the appearance of the STE(II) emissions. These facts suggest that there are multiple (three in LSB, two in YSB) local minima on the adiabatic potential energy surfaces, i.e., the barriers for the exciton self trapping in LSB and YSB. Multi-step transitions correspond to the evolution from STE(I) to STE(II) and further to STE(III).

Figure 3 compares the temperature dependence of the rate of decrease in the STE(I), (II), and (III) emissions in the  $RE^{3+}$ -doped and undoped samples of LSB and YSB.

For a high  $RE^{3+}$  doping concentration (5%), the rate of decrease did not show notable changes, or gradually decreased up to approximately 200 K, followed by a gradual increase as temperature rose, whereas for low  $Sm^{3+}$  doping (1%), the rate of decrease increased monotonically with increasing temperature. These results suggest that for the low  $RE^{3+}$  doping, the thermally assisted energy transfer process related to the exciton (STE) mobility was activated as the temperature increased.

In the case of LSB at a temperature of 293 K, the energy transfer rates determined from time-resolved measurements were  $1.9 \times 10^6 s^{-1}$  (STE(II)) and  $1.8 \times 10^5 s^{-1}$  (STE(III)) for 5 at.%  $Sm^{3+}$  doping,  $1.6 \times 10^6 s^{-1}$  (STE(II)) and  $0.8 \times 10^5 s^{-1}$  (STE(III)) for 5 at.%  $Gd^{3+}$  doping, and  $2.2 \times 10^6 s^{-1}$  (STE(II)) and  $0.8 \times 10^5 s^{-1}$  (STE(III)) for 5 at.%  $Tb^{3+}$  doping. The energy transfer rates in the YSB at 293 K were  $1.9 \times 10^7 s^{-1}$  (STE(I)) and  $5.6 \times 10^5 s^{-1}$  (STE(II)) for 5 at.%  $Gd^{3+}$  doping and  $6.5 \times 10^6 s^{-1}$  (STE(II)) and  $1.5 \times 10^5 s^{-1}$  (STE(III)) for 1 at.%  $Tb^{3+}$  doping. The observed energy transfer rates were the same magnitude as, or within an order of magnitude of, the estimates based on dipole-dipole energy transfer.

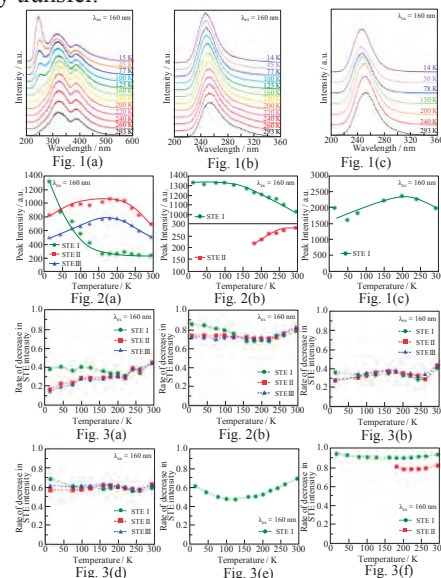


Fig. 1. Temperature dependence of intrinsic luminescence spectra in (a) undoped LSB, (b) YSB, and (c) LuSB in the range 15(or 14)–293 K.

Fig. 2. Temperature dependence of STE intensity for undoped samples: (a) LSB, (b) YSB, and (c) LuSB.

Fig. 3. Temperature dependence of rate of decrease in STE(I), (II), and (III) emissions in  $RE^{3+}$ -doped and undoped samples for LSB and YSB: (a) 1%  $Sm$ -doped LSB, (b) 5%  $Sm$ -doped LSB, (c) 5%  $Gd$ -doped LSB, (d) 5%  $Tb$ -doped LSB, (e) 5%  $Gd$ -doped YSB, and (f) 5%  $Tb$ -doped YSB.

BL3B

## Charging States of Oxygen Vacancies in Yttria-Stabilized Zirconia Analyzed by the Decay of Photoluminescence

S. Kaneko, T. Morimoto and Y. Ohki  
Waseda University, Tokyo 169-8555, Japan

In yttria-stabilized zirconia (YSZ),  $ZrO_2$  is partly replaced by  $Y_2O_3$ . This means that oxygen vacancies are present in YSZ with the same ratio as that of  $Y_2O_3$  [1]. In order to examine the electronic energy structure of the oxygen vacancy in YSZ, the decaying behavior of photoluminescence (PL) was observed in YSZ.

It has been known that the PL with a peak energy of 2.8 eV appearing in YSZ as shown in Fig. 1 is due to the oxygen vacancy and that the oxygen vacancy can take three different charging states [1-3]. However, the charging state from which the PL is emitted is unclear.

Using the single-bunch mode of synchrotron radiation at BL3B line in the UVSOR facility as an excitation photon source, we observed the decay of the 2.8-eV PL excited by 5.2-eV photons in a ns-range. As shown in Fig. 2(a), the decay constant of the PL can be estimated as 7 ns. In addition, we measured the decay in a ms-range using a fluorescence spectrometer FP-8500 (Jasco). As shown by the black open circles in Fig. 2(b), the 2.8-eV PL decays with a lifetime of around 0.3 ms. Note that red open squares show the decay in intensity of the excitation photons induced by the movement of a mechanical shutter.

When an oxygen atom is removed from a certain site, the site would be effectively charged positively. Therefore, the site attracts electrons. Regarding this, the oxygen vacancy capturing no electrons is called the  $F^{2+}$  center, while the ones capturing one and two electrons are called the  $F^+$  center and the F center, respectively.

The PL, which has been attributed to oxygen vacancies, has been reported for many oxides. It has been known that the F centers in alumina [4] and  $YAlO_3$  [5] induce phosphorescence with a time constant of the order of ms, while the  $F^+$  centers have been assigned to the origin of fluorescence with a time constant of the order of ns. Taking these facts into account, the 2.8-eV PL in YSZ would be ascribable to both the  $F^+$  and F centers.

However, it is unlikely that both the  $F^+$  and F centers with different charging states emit photons with the same energy. In this regard, we assume the following luminescent mechanism as a plausible model. Namely, the 2.8-eV PL in YSZ is induced by the  $F^+$  centers with the decay constant of 7 ns. One important fact is that the  $F^+$  centers can be generated if one electron is released from the F centers in addition to those originally present in YSZ. If the

release of electrons needs a certain long time, the 2.8-eV PL must have a large decay constant like 0.3 ms when it is originated from the F centers.

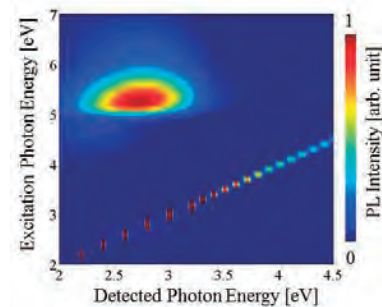
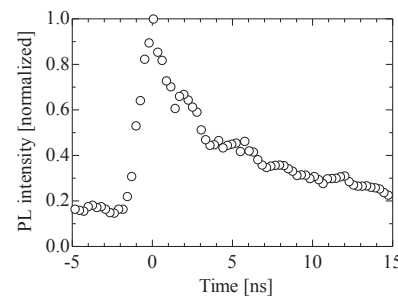
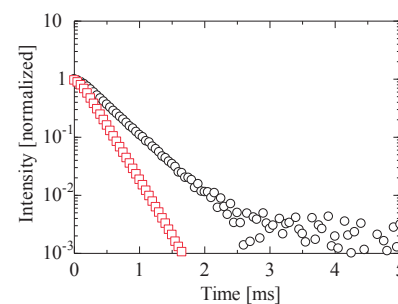


Fig. 1. Distribution of PL energy and PL excitation energy observed for YSZ at 10 K.



(a)



(b)

Fig. 2. Decay profiles of the 2.8-eV PL observed in YSZ; (a) in a ns range and (b) in a ms range ( $\circ$ ) in comparison with the decay of excitation photons with an energy of 5.2 eV ( $\square$ ), normalized by their respective initial values.

- [1] J. M. Costantini, *et al.*, *J. Nucl. Mater.* **440** (2013) 508.
- [2] H. Nakajima, *et al.*, *J. Alloys Compd.* **408** (2006) 728.
- [3] T. Morimoto, *et al.*, *Jpn. J. Appl. Phys.* **47** (2008) 6858.
- [4] A. I. Surdo, *et al.*, *Radiat. Meas.* **33** (2001) 587.
- [5] Y. V. Zorenko, *et al.*, *Opt. Spectrosc.* **96** (2004) 532.

BL3B

## Band Gap of B1-Type $M_xZn_{1-x}O$ ( $M = Mg, Mn, Fe, Co, Ni$ ) Synthesized under High Pressures

K. Takahama<sup>1</sup>, K. Usui<sup>1</sup>, D. Shimada<sup>2</sup>, M. Kato<sup>1</sup>, K. Niwa<sup>2</sup>, K. Kusaba<sup>2</sup>,  
M. Hasegawa<sup>2</sup> and K. Soda<sup>1</sup>

<sup>1</sup>Department of Quantum Engineering, Graduate School of Engineering, Nagoya University,  
Nagoya 464-8603, Japan

<sup>2</sup>Department of Crystalline Materials Engineering, Graduate School of Engineering, Nagoya University,  
Nagoya 464-8603, Japan

Wide gap semiconductor ZnO is one of promising materials for light emitting devices, transparent conducting electrodes, catalysis, solar cells, and so on [1]. There have been many proposals and efforts for controlling such as a band gap width and energy positions of conduction band minimum and valence band maximum, and hence its functional properties, by forming mixed crystals with other metal oxides [2, 3]. Recently B1(NaCl)-type mixed crystals  $M_xZn_{1-x}O$  ( $M = Mg, Mn, Fe, Co, Ni$ ) have been successfully synthesized under high pressures [4], where ZnO transforms the B4(wurtzite)-type structure to B1-type. In this report, we have investigated their reflectance spectra to estimate their band gaps.

Measurement of reflectance spectra was performed at BL3B for polycrystalline specimens of about 1 mm in thickness and  $\sim 2$  mm in diameter synthesized at 1173 K under a pressure of 6.5 GPa with DIA-type cubic anvil cell. The band gaps were estimated with the Tauc plot for an indirect transition [5].

Figure 1 compares the estimated band gap (red circle) with those experimentally evaluated from valence band photoelectron measurements (PES, blue circles) [6, 7] for the present specimens as well as experimental values of ZnO and MgO (black circles) in ref. [3] and calculated with the first principle calculations [2, 7, 8]. Here, theoretical direct and indirect band gaps are shown by solid and broken lines, respectively, which were calculated with full potential linearized augmented plane wave method with generalized gradient approximation (GGA) by Perdew-Burke-Ernzerhof (PBE) and Engle-Vosko (EV) [2] and with full potential linear muffin-tin orbital method (LMTO) [8]. Experimental results are also presented by open black circles for B1-type  $Mg_xZn_{1-x}O$  films grown by pulsed laser deposition [9].

The present band gaps agree quantitatively well with those obtained by PES and qualitatively with theoretical predictions, taking into account that the underestimation of the band gap is well known for these calculations. The agreement of both the present and PES experimental estimations of the band gap indicates the n-type nature of the specimens, which was assumed for the previous estimation from PES. For  $x = 0.75$ , band gaps for the bulk specimens are considerably different from those reported for the

film. This may be due to effects of Zn as an impurity for the Mg-rich films or different crossover between indirect and direct band gaps of the films on a substrate from the bulk specimens, although the reason has not been clarified at present yet.

Results will be reported elsewhere on other mixed crystals.

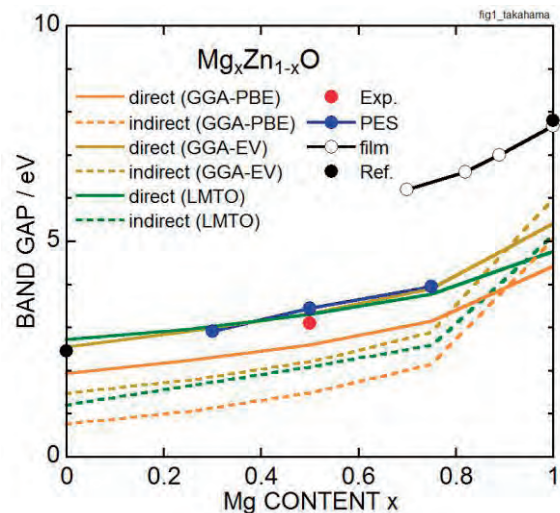


Fig. 1. Band Gaps of B1-type  $Mg_xZn_{1-x}O$ .

- [1] H. Q. Ni *et al.*, *J. Appl. Phys.* **91** (2002) 1339.
- [2] B. Armani *et al.*, *Compt. Mater. Sci.* **40** (2007) 66.
- [3] D. K. Kanan and E. A. Carter, *J. Phys. Chem. C* **116** (2012) 9876.
- [4] D. Simada, Master thesis (Nagoya University, 2013).
- [5] J. Tauc *et al.*, *Phys. Status Solidi* **15** (1966) 627.
- [6] K. Takahama *et al.*, UVSOR Activity Report 2013 **41** (2014) 83.
- [7] K. Soda *et al.*, Aichi SR Report (2013) 2504026.
- [8] F. Z. Aoumeur-Benkabou *et al.*, *Model. Num. Sim. Mater. Sci.* **2** (2012) 60.
- [9] R. Schmidt-Grund *et al.*, *AIP Conf. Proc.* **772** (2005) 201.

BL3B

## Energy Transfer from $Tl^+$ Centers to $In^+$ Centers in Co-Doped $NaCl:Tl^+, In^+$ Crystals

A. Iguchi and T. Kawai

Graduate School of Science, Osaka Prefecture University, Sakai 599-8531, Japan

Alkali halide crystals have the wide band-gap up to the vacuum ultraviolet energy region and are a suitable candidate host for doping of impurity ions. Among a lot of impurity ions,  $Tl^+$ -type ions that have the  $ns^2$  electronic configuration in their ground state are well-known as impurity ions doped in alkali halides [1,2]. Although many experimental studies have been performed on  $Tl^+$ -type centers in alkali halides, energy transfer between  $Tl^+$ -type centers in alkali halides are comparatively less studied. In this study, we have investigated the energy transfer from  $Tl^+$  centers to  $In^+$  centers in  $NaCl$  crystals co-doped with the  $Tl^+$  and  $In^+$  ions at the BL-3B line of UVSOR.

Figure 1 shows the absorption spectrum of  $NaCl:In^+$  and the luminescence spectrum of  $NaCl:Tl^+$  in the energy range from 3.6 to 4.8 eV. In  $NaCl:In^+$ , the A absorption band having doublet structure and the B absorption band appearing as a shoulder are observed at 4.1 and 4.6 eV, respectively. The C absorption band is located around 5.1 eV in the higher energy region than the B absorption band. In  $NaCl:Tl^+$ , the A' luminescence band due to the  $Tl^+$  centers is observed around 4.25 eV. The A' luminescence band in  $NaCl:Tl^+$  has a large overlap with the A absorption band in  $NaCl:In^+$ . The fact indicates the potential of the energy transfer from the  $Tl^+$  centers to the  $In^+$  centers in co-doped  $NaCl:Tl^+, In^+$  crystals. According to the Förster model [3,4], the critical distance between both centers for resonant energy transfer is estimated to be 17.5 Å from the overlap with the luminescence and absorption bands.

Figure 2 shows the excitation spectra in  $NaCl:Tl^+$ ,  $NaCl:In^+$ , and co-doped  $NaCl:Tl^+, In^+$  crystals at room temperature (RT). The A' luminescence band in  $NaCl:Tl^+$  is efficiently excited in the energy region around 4.8 eV and 6.1 eV, where the A, B, and C absorption bands of the  $Tl^+$  centers are located. In  $NaCl:In^+$ , the luminescence band at 3.00 eV, which corresponds to the A' luminescence band of the  $In^+$  centers, is efficiently excited at the A, B, and C absorption bands of the  $In^+$  centers.

In the co-doped  $NaCl:Tl^+, In^+$  crystal, the excitation spectrum for the A' luminescence band of the  $In^+$  centers has the broad band around 6.10 eV in addition to the A, B, and C bands of the  $In^+$  centers. Since the 6.10 eV band corresponds to the excitation band for the A' luminescence band in  $NaCl:Tl^+$ , the fact implies the existence of the energy transfer from the  $Tl^+$  centers to the  $In^+$  centers in the co-doped  $NaCl:Tl^+, In^+$  crystal. In order to clarify the energy

transfer mechanism from the  $Tl^+$  centers to the  $In^+$  centers in the co-doped  $NaCl:Tl^+, In^+$  crystals, the measurements of the decay kinetics of the luminescence are needed.

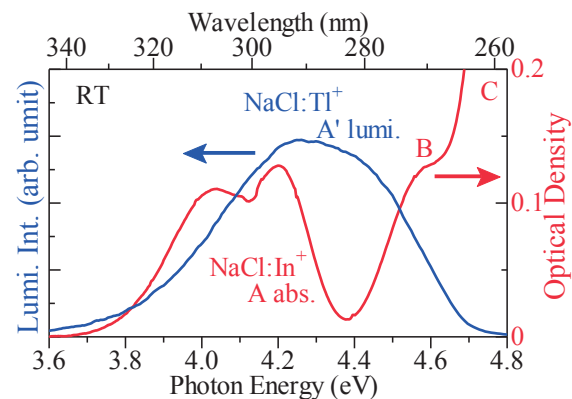


Fig. 1. Luminescence spectrum (blue) of  $NaCl:Tl^+$  and absorption spectrum (red) of  $NaCl:In^+$  at RT.

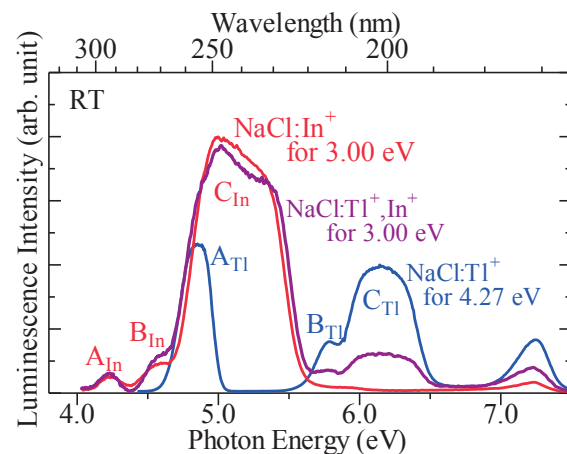


Fig. 2. Excitation spectra of  $NaCl:Tl^+$  (blue),  $NaCl:In^+$  (red), and co-doped  $NaCl:Tl^+, In^+$  (purple).

[1] A. Ranfagni *et al.*, *Advances in Physics* **32** (1983) 823.

[2] P. W. M. Jacobs, *J. Phys. Chem. Solids* **52** (1991) 35.

[3] T. Förster, *Disc. Faraday Soc.* **27** (1959) 7.

[4] D. L. Dexter, *J. Chem. Phys.* **21** (1953) 836.

BL3B

## Luminescence Band with a Zero-Phonon Line in NaCl:TI<sup>+</sup> Crystals

T. Kawai

Graduate School of Science, Osaka Prefecture University, Sakai 599-8531, Japan

TI<sup>+</sup> centers in alkali halide crystals are well-known as a strong electron-phonon interaction system and exhibit the broad luminescence band with a large Stokes shift. Though lots of the optical studies have been performed for the TI<sup>+</sup> centers in alkali halides [1,2], the optical measurements with high-resolution are considerably less. We have performed the optical measurements with high-resolution for NaCl:TI<sup>+</sup> crystals at the BL-3B line of UVSOR.

Figure 1 shows the absorption spectrum up to the vacuum ultraviolet energy region at low temperature in NaCl:TI<sup>+</sup>. The broad absorption bands called A, B, and C are observed at 4.87, 5.77, and 6.19 eV, respectively. The A, B, and C absorption bands are attributed to the intra-ionic transitions from the ground <sup>1</sup>A<sub>1g</sub> state to the excited <sup>3</sup>T<sub>1u</sub>, <sup>3</sup>T<sub>2u</sub>+<sup>3</sup>E<sub>u</sub>, and <sup>1</sup>T<sub>1g</sub> states in the TI<sup>+</sup> centers, respectively[1,2].

Figure 2 shows the luminescence and absorption spectra measured by high-resolution spectroscopy in the vicinity of the A band in NaCl:TI<sup>+</sup>. The broad luminescence band called A' appears with a Stokes shift. It should be noted that the A' luminescence band has a weak zero-phonon line at 4.622 eV. On the other hand, the A absorption band has no zero-phonon line and no overlap with the A' luminescence band. This odd spectra can be explained on the basis of a fact that the A' luminescence band is composed of two luminescence bands.

In general, the A' luminescence band of the TI<sup>+</sup> centers comes from the radiative transitions from the relaxed excited states of <sup>3</sup>A<sub>1u</sub> and <sup>3</sup>T<sub>1u</sub>. The excited <sup>3</sup>A<sub>1u</sub> state is located at the slightly lower energy position than the <sup>3</sup>T<sub>1</sub> state. Since the transition from the <sup>1</sup>A<sub>1g</sub> state to the <sup>3</sup>A<sub>1u</sub> state is strongly forbidden, the absorption band due to the <sup>3</sup>A<sub>1u</sub> state is not usually observed on the absorption spectrum. Therefore, the A absorption band observed in the absorption spectra comes from the transition from the <sup>1</sup>A<sub>1g</sub> state to the <sup>3</sup>T<sub>1u</sub> state. On the other hand, the radiative transition from the relaxed excited state of <sup>3</sup>A<sub>1u</sub> occurs with the long decay time constant of a few milliseconds. If the lattice-relaxation of the excited <sup>3</sup>A<sub>1u</sub> state is considerably smaller than that of the excited <sup>3</sup>T<sub>1u</sub> state, the luminescence band from the relaxed excited state of <sup>3</sup>A<sub>1u</sub> would appear at the higher energy position than that from the excited relaxed state of <sup>3</sup>T<sub>1u</sub>. Then, the luminescence band with a zero-phonon line might be observed with an apparent Stokes shift, as shown in Fig. 2. Therefore, the zero-phonon line at 4.622 eV in NaCl:TI<sup>+</sup> is attributed to the radiative transition from the <sup>3</sup>A<sub>1u</sub> state.

The luminescence band from the relaxed excited

state of <sup>3</sup>T<sub>1u</sub> has the shorter decay time constant of a few ten nanoseconds. The fact implies that the time-resolved luminescence spectroscopy would allow us to decompose the A' luminescence band into the slowly decaying luminescence band and the fast-decaying luminescence band, which correspond to the luminescence bands from the relaxed excited states of <sup>3</sup>A<sub>1u</sub> and <sup>3</sup>T<sub>1u</sub>, respectively. In order to confirm the above idea, we are planning to perform a time-resolved luminescence spectroscopy.

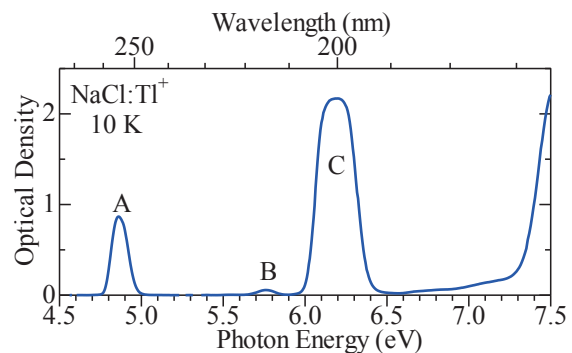


Fig. 1. Absorption spectrum of a NaCl:TI<sup>+</sup> crystal.

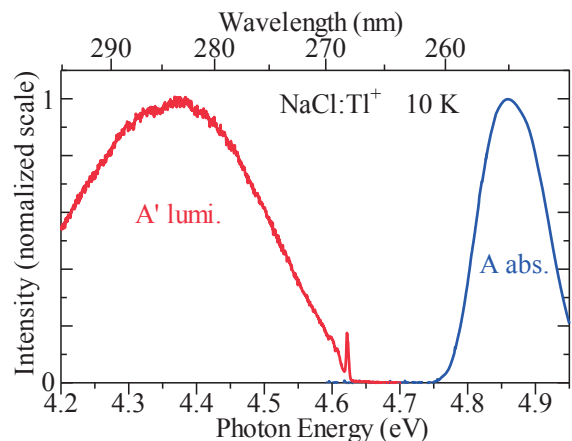


Fig. 2. The A' luminescence band and the A absorption band obtained by using a high-resolution spectroscopy.

[1] A. Ranfagni *et al.*, *Advances in Physics* **32** (1983) 823.

[2] P. W. M. Jacobs, *J. Phys. Chem. Solids* **52** (1991) 35.

BL3B

## Anomalous Excitons and Screenings Unveiling Strong Electronic Correlations in $\text{SrTi}_{1-x}\text{Nb}_x\text{O}_3$

P. K. Gogoi<sup>1,2,3</sup>, L. Sponza<sup>4</sup>, D. Schmidt<sup>1</sup>, T. C. Asmara<sup>1,2,3</sup>, C. Diao<sup>1</sup>, J. C. W. Lim<sup>1,2</sup>, S. M. Poh<sup>1</sup>, S. Kimura<sup>6</sup>, P. E. Trevisanutto<sup>1,3,5</sup>, V. Olevano<sup>7</sup> and A. Rusydi<sup>1,2,3</sup>

<sup>1</sup>Singapore Synchrotron Light Source, National University of Singapore, 117603, Singapore

<sup>2</sup>NUSNNI-NanoCore, National University of Singapore, 117576, Singapore

<sup>3</sup>Department of Physics, National University of Singapore, 117542, Singapore

<sup>4</sup>Laboratoire des Solides Irradiés, École Polytechnique, CNRS, F-91128 Palaiseau, France

<sup>5</sup>Centre for Advanced 2D Materials and Graphene Research Centre, National University of Singapore, 117546, Singapore

<sup>6</sup>Graduate School of Frontier Biosciences, and Department of Physics, Osaka University, Suita 565-0871, Japan

<sup>7</sup>Institut Néel, CNRS, BP 166, F-38042 Grenoble, France

Strong electronic correlations in transition metal oxides are known to drive rich phenomena such as superconductivity, colossal magnetoresistance and metal insulator transitions [1]. An example of a model transition metal oxide is the perovskite-type  $\text{SrTiO}_3$  (STO). Indeed, STO in various bulk forms and recently its heterostructures with other oxides, have shown exotic phenomena such as superconductivity, magnetisms, metal-insulator transitions and two-dimensional electron gas. However the role of electronic correlations, particularly electron-hole (e-h) and electron-electron (e-e) interactions, remains unclear. Then we measured the temperature dependence of the optical conductivity spectra of STO and  $\text{SrTi}_{1-x}\text{Nb}_x\text{O}_3$  with  $x = 0.005$  (STNO) and obtained the spectral weight transfer.

In Fig. 1a (1b), the real part of the optical conductivity, is plotted for STO (STNO) for temperatures of 4.2, 200 and 350 K. The energy range is divided into 9 separate ranges for convenience of analysis. As can be seen in Fig. 1c (1d) the spectral weight of the first excitonic region (Ex1) (shown as Region 2) decreases monotonically with a slight dip in the temperature range of 75 – 150 K. STO has a phase transition from cubic to tetragonal around 105 K with a very slight change of the  $c$  axis [2]. These dips, both in STO and STNO, could be due to this phase change which has been reported to occur over a range of 60 K previously [3]. Here the spectral weight of the band-edge region (shown as Region 3) remains almost constant for both STO and STNO. A similar trend is seen for the second excitonic region (Ex2) (shown as Region 5) and the corresponding next region (shown as Region 6) respectively in Fig. 1e (1f). Also plotted are the spectral weight functions for the energy range before the excitonic region in this case (as Region 4). Importantly it has opposite spectral weight transfer as that of the excitonic region and it is seen that the spectral weight for Region 4 and Region 5 are almost conserved together. These spectral weight analysis sheds further light on the various general aspects of the excitonic effects present in STO and STNO.

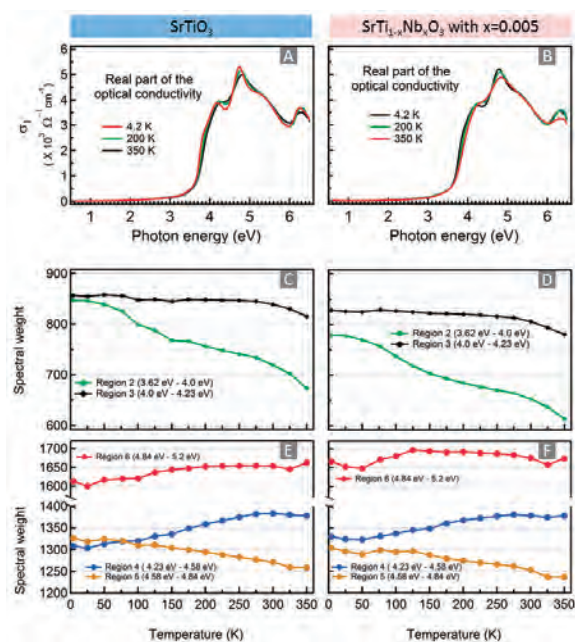


Fig. 1. Real part of the optical conductivity and spectral weight transfer. Real part of the optical conductivity at selected temperatures for (a) STO and (b) STNO. Temperature dependence of spectral weight for the first direct inter-band (Region 3) transition and for associated excitonic spectra around peaks Ex1 (Region 2) for (c) STO and (d) STNO. Temperature dependence of spectral weight for regions around and including excitonic peak Ex2 for (e) STO and (f) STNO.

[1] D. N. Basov *et al.*, *Rev. Mod. Phys.* **83** (2011) 471.

[2] K. A. Müller, W. Berlinger and F. Waldner, *Phys. Rev. Lett.* **21** (1968) 814.

[3] K. W. Blazey, *Phys. Rev. Lett.* **27** (1971) 146.

BL3B

## Ultraviolet Photoluminescence of $Gd^{3+}$ in $Gd^{3+}$ - $Pr^{3+}$ Co-Doped Yttrium Aluminate under Vacuum Ultraviolet Excitation

K. Ueda<sup>1</sup>, Y. Shimizu<sup>1</sup>, A. Takiguchi<sup>1</sup>, Y. Taira<sup>2</sup> and Y. Inaguma<sup>2</sup>

<sup>1</sup> Department of Materials Science, Graduate school of Engineering, Kyushu Institute of Technology, Kitakyushu 804-8550, Japan

<sup>2</sup> Department of Chemistry, Faculty of Science, Gakushuin University, Tokyo 171-8588, Japan

It is known that a  $Gd^{3+}$  center shows a sharp emission peak at approximately 310 nm in UV-B region, which is attributed to the 4f-4f transition from  ${}^6P_J$  to  ${}^8S_{7/2}$  states. The sharp emission from  $Gd^{3+}$  is anticipated as a new light source for medical application such as phototherapy for skin disease [1] and transilluminator for DNA analysis [2]. In the recent studies,  $Pr^{3+}$  co-doping was found to give a large excitation band for  $Gd^{3+}$  emission in some materials such as  $LaPO_4$  [2] and  $YAlO_3$  [3]. Although the excitation band is considered to be derived from the  $Pr^{3+}$  4f-5d absorption, the details are unknown yet. In this study,  $Gd^{3+}$  and  $Pr^{3+}$  co-doped  $YAlO_3$  were prepared and the fundamental UV photoluminescence (PL) properties were investigated by VUV excitation.

The polycrystalline samples of  $(Y_{1-x-y}Gd_xPr_y)AlO_3$  ( $x=0.00-0.07$  and  $y=0.00-0.03$ ) were prepared by a polymerized complex method, using  $Y_2O_3$ ,  $Gd_2O_3$ ,  $Pr_6O_{11}$ ,  $Al(NO_3)_3 \cdot 9H_2O$  as starting materials. Citric acid monohydrate and propylene glycol were used to form the polymerized complex gels. The sample powders were obtained by heating at 1400 °C in air. The obtained powders were pressed into pellets and sintered at 1400 °C in air. The phases in the samples were identified by the powder X-ray diffraction (XRD) using a Rigaku RINT 2500 diffractometer (CuK $\alpha$  radiation). The emission and excitation spectra were measured at the beamline BL3B in UVSOR.

Each sample was identified as a distorted perovskite type phase with a space group Pnma. Because no impurity phases were observed in their XRD patterns, it was confirmed that both  $Gd^{3+}$  and  $Pr^{3+}$  were dissolved into the host lattices. Figure 1 shows PL spectra observed in  $(Y_{1-x-y}Gd_xPr_y)AlO_3$  at room temperature along with the PL intensities as a function of x or y. All  $Gd^{3+}$  doped samples showed  $Gd^{3+}$  emission peaks at 314 nm originating from  ${}^6P_{7/2}$  to  ${}^8S_{7/2}$  transition. The maximum PL intensity was observed at  $x=0.07$  and  $y=0.03$ . It is noteworthy that even a small amount of  $Pr^{3+}$  co-doping such as  $y=0.01$  enhanced the  $Gd^{3+}$  emission.

Figure 2 shows PL excitation spectra of  $(Y_{1-x-y}Gd_xPr_y)AlO_3$ . An intense band, that was assignable to host lattice excitation, was observed at 157 nm for a  $Gd^{3+}$  single doped sample. In contrast, another intense band was observed at approximately 220 nm for  $Gd^{3+}$  and  $Pr^{3+}$  co-doped samples. The shape of the excitation spectra for  $Gd^{3+}$ - $Pr^{3+}$  co-doped

samples agreed well with the one for a  $Pr^{3+}$  single doped sample that monitored  $Pr^{3+}$  5d-4f emission at 243 nm. As the result, the  $Gd^{3+}$  emission mechanism in  $Gd^{3+}$ - $Pr^{3+}$  co-doped samples was found to be considerably different from that in the  $Gd^{3+}$  single doped one. The  $Gd^{3+}$  emission in  $Gd^{3+}$ - $Pr^{3+}$  co-doped samples occurred through energy transfer from  $Pr^{3+}$  to  $Gd^{3+}$ , even on the excitation of the host lattices.

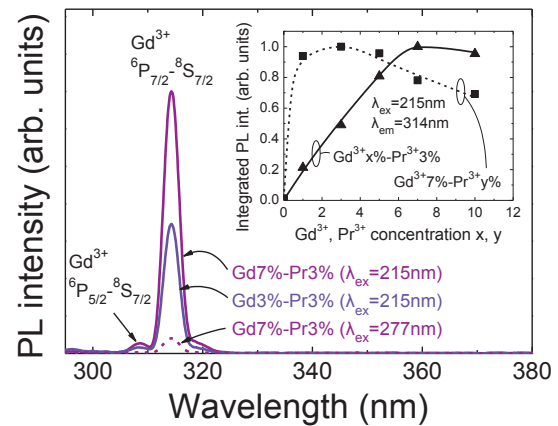


Fig. 1.  $Gd^{3+}$  PL spectra in  $(Y_{1-x-y}Gd_xPr_y)AlO_3$ . Inset shows the PL intensities as a function of  $Gd^{3+}$  and  $Pr^{3+}$  concentration x, y.

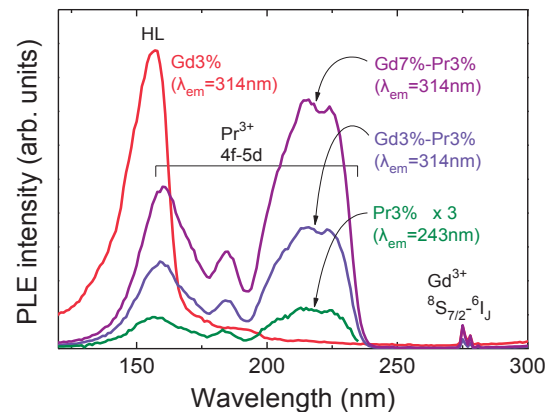


Fig. 2. PL excitation spectra of  $(Y_{1-x-y}Gd_xPr_y)AlO_3$ . Only the spectrum of  $(Y_{0.97}Pr_{0.03})AlO_3$  is magnified.

[1] R. P. Sonekar, S. K. Omanwar, S. V. Moharil, S. M. Dhopte, P. L. Muthal and V. K. Kondawar, *Opt. Mater.* **30** (2007) 622.

[2] S. Okamoto, R. Uchino, K. Kobayashi and H. Yamamoto, *J. Appl. Phys.* **106** (2009) 013522.

[3] Y. Shimizu, Y. Takano and K. Ueda, *J. Lumin.* **141** (2013) 44.

BL3B

## Excitation and Emission Spectra of $\text{Ce}^{3+}$ in $\text{Ba}_3\text{Y}_2\text{B}_6\text{O}_{15}$

M. Yoshino, M. Hotta and S. Watanabe

Graduate School of Engineering, Nagoya University, Nagoya 464-8603, Japan

The trivalent lanthanide ions (e.g.,  $\text{Nd}^{3+}$ ,  $\text{Er}^{3+}$ ,  $\text{Yb}^{3+}$ ) in Oxide crystals have drawn attentions due to their application for luminescent materials in NIR to UV regions such as solid-state lasers or phosphors. The trivalent cerium ion,  $\text{Ce}^{3+}$ , has also attracted attentions as luminescence centers. In this work, the  $4f-5d$  excitation spectra and emission spectra for  $\text{Ce}^{3+}$  in  $\text{Ba}_3\text{Y}_2\text{B}_6\text{O}_{15}$  crystal have been measured. For the comparison, the excitation spectra and emission spectra for  $\text{Pr}^{3+}$ -doped  $\text{Ba}_3\text{Y}_2\text{B}_6\text{O}_{15}$  have been also measured. The Ce doped and Pr doped samples are produced by solid state reactions. The concentration of dopants in the samples are 0.5 and 1.0 mol%. Figure 1 shows the excitation spectrum monitored 440 nm for  $\text{Ba}_3(\text{Y}_{0.995}\text{Ce}_{0.005})_2\text{B}_6\text{O}_{15}$ . The peaks B and C originate in the absorption of the  $4f-5d$  transitions of  $\text{Ce}^{3+}$ . The peak A originates in the absorption of the  $\text{Ba}_3\text{Y}_2\text{B}_6\text{O}_{15}$  host crystal. The peaks related to the absorption in the host and the  $4f-5d$  transition of lanthanide ion are seen also in the excitation spectrum for  $\text{Pr}^{3+}$ -doped sample. They are shown as A and B in Fig. 2, respectively. The emission spectra for  $\text{Ce}^{3+}$  in  $\text{Ba}_3\text{Y}_2\text{B}_6\text{O}_{15}$  are shown in Fig. 3 and 4. The emission intensity in 0.5 mol% sample is higher than in 1.0 mol% sample due to the concentration quenching. Each emission spectra have shoulder and may consist of two peaks due to the two final states of  $4f$  energy levels. As shown in Fig. 4, the shape of the two emission spectra with excited in other  $\text{Ce}^{3+}$  absorption wavelength, 336 and 356 nm, are different. From this result, these two transitions occur in  $\text{Ce}^{3+}$  on the different sites. On the other hand, similarity in the emission excited with 336 and 187 nm indicates preferential energy transfer from host to  $\text{Ce}^{3+}$  in the particular site.

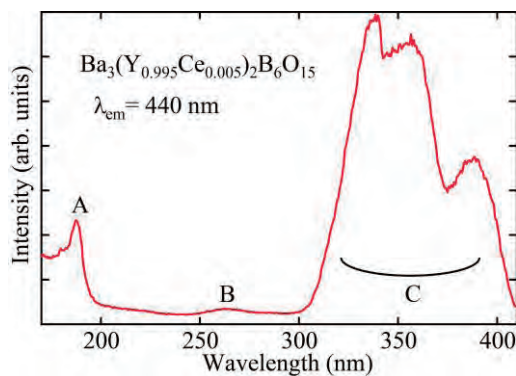


Fig. 1. Excitation spectrum of  $\text{Ba}_3(\text{Y}_{0.995}\text{Ce}_{0.005})_2\text{B}_6\text{O}_{15}$ .

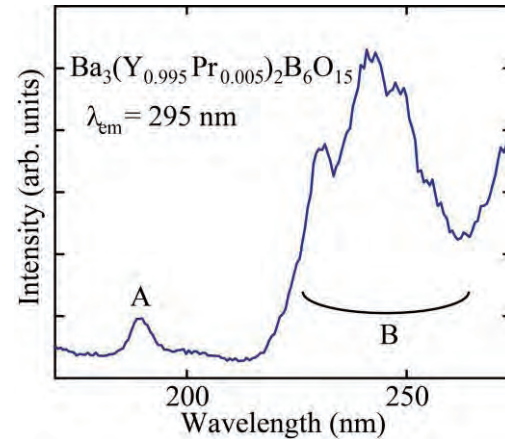


Fig. 2. Excitation spectrum of  $\text{Ba}_3(\text{Y}_{0.995}\text{Pr}_{0.005})_2\text{B}_6\text{O}_{15}$ .

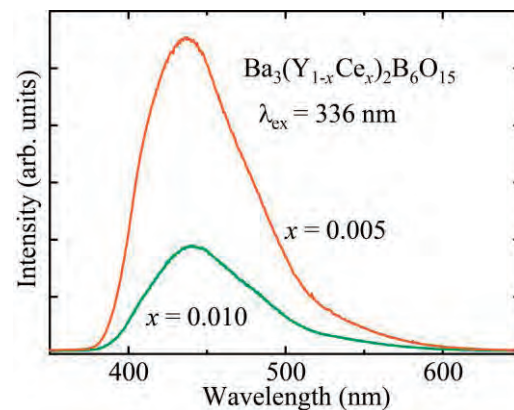


Fig. 3. Emission spectra of Ce-doped  $\text{Ba}_3\text{Y}_2\text{B}_6\text{O}_{15}$ .

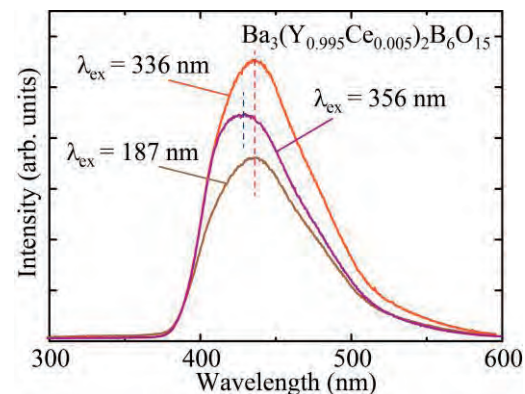


Fig. 4. Emission spectra of  $\text{Ba}_3(\text{Y}_{0.995}\text{Ce}_{0.005})_2\text{B}_6\text{O}_{15}$ .

BL3B

## Optical Spectroscopy of Nd and Cr Codoped $Y_3Sc_xGa_yAl_{5-x-y}O_{12}$ Single Crystals

M. Yamaga, T. Kishita, S. Fujiwara, Y. Takeda and A. Ogata

*Department of Mathematical and Design Engineering, Gifu University, Gifu 501-1193, Japan*

Garnet crystals codoped with Nd and Cr are a candidate of solar-pumped laser materials. In order to improve pumping efficiency of  $Nd^{3+}$  luminescence and energy transfer of  $Cr^{3+}$  to  $Nd^{3+}$ , substitutional disordered crystals  $Y_3Sc_xGa_yAl_{5-x-y}O_{12}$  were prepared. The prepared garnet crystals were denoted by YAG ( $x=0, y=0$ ), YSAG ( $x=0.2, y=0$ ), YGAG ( $x=0, y=0.2$ ). The substitution produces inhomogeneous broadening of the  $Nd^{3+}$  and  $Cr^{3+}$  optical spectra. Enhancement of overlapping between the  $Cr^{3+}$  absorption and solar spectra and between the  $Cr^{3+}$  luminescence bands and the  $Nd^{3+}$  absorption lines lead to an increase of the pumping efficiency and the energy transfer rates, respectively.

Figure 1 shows the absorption spectra of Nd:Cr:YGAG, Nd:Cr:YSAG in comparison with that of Nd:Cr:YAG. The base lines are shifted for clarity. The sharp lines observed in the ultraviolet (UV), visible, and near infrared (IR) regions for three crystals are due to the optical transitions from the  $^4I_{9/2}$  multiplet ground state of  $Nd^{3+}$  to the multiplet excited states. Three broad bands with peaks at 270, 430, and 600 nm are assigned to the optical transitions from the  $^4A_2$  ground state of  $Cr^{3+}$  to the  $^4T_1(2)$ ,  $^4T_1(1)$ , and  $^4T_2$  excited states, respectively. The difference in the absorption spectra of (Nd:Cr:YGAG, Nd:Cr:YSAG) and Nd:Cr:YAG in Fig. 1 is inhomogeneous broadening of the  $Nd^{3+}$  lines in Nd:Cr:YGAG or Nd:Cr:YSAG caused by substitution of  $Ga^{3+}$  or  $Sc^{3+}$  for  $Al^{3+}$ , respectively. The absorption coefficients of  $Cr^{3+}$  bands and  $Nd^{3+}$  lines in Nd:Cr:YGAG and Nd:Cr:YSAG were (2.5, 0.7) or (0.7, 0.1) times compared with those in Nd:Cr:YAG, respectively. This estimated ratios are nearly equal to the concentration ratios of Cr and Nd contained in these samples, respectively.

Figure 2 shows the normalized luminescence spectra excited at 430 nm in the  $^4T_1(1)$  absorption band of  $Cr^{3+}$  for three crystals. These spectra consist of sharp intense R lines around 690 nm and phonon-absorbed and phonon-emitted side bands around 678 and 707 nm of  $Cr^{3+}$  and weak near IR lines around 885 nm due to the optical transitions from the metastable  $^4F_{3/2}$  excited state of  $Nd^{3+}$  to the  $^4I_{9/2}$  lowest state.

Figure 3 shows the excitation spectra of the  $Nd^{3+}$  luminescence lines at 885 nm for three crystals. The excitation spectra are the superposition of the  $Cr^{3+}$  absorption bands and the  $Nd^{3+}$  absorption lines. The observation of the  $Cr^{3+}$  bands in the  $Nd^{3+}$  excitation spectrum gives evidence on the energy transfer from  $Cr^{3+}$  to  $Nd^{3+}$ .

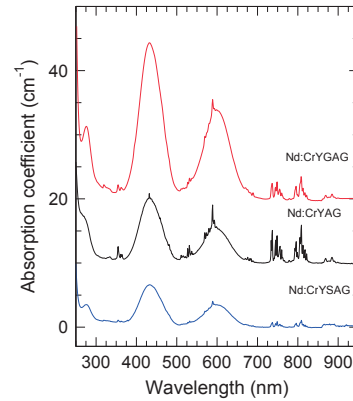


Fig. 1. Absorption spectra for three garnet crystals.

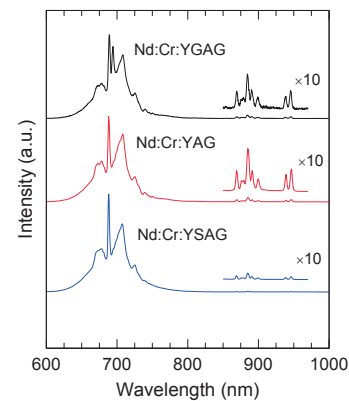


Fig. 2. Emission spectra for three garnet crystals.

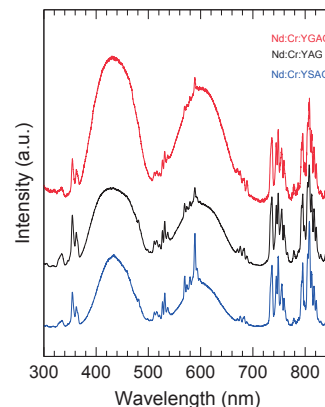


Fig. 3. Excitation spectra for three garnet crystals.

BL3B

## Relaxed Exciton Luminescence of RbCl Heavily Doped with RbI

N. Ohno and K. Sakae

Graduate School of Engineering, Osaka Electro-Communication University, Neyagawa 572-8530, Japan

Extensive studies have been made on luminescence arising from localized relaxed excitons in alkali chlorides containing iodine impurities. Dilute  $\Gamma$ -doped crystals stimulated with VUV light or X-rays produces characteristic luminescence bands. The luminescence bands have been well explained in terms of localized relaxed excitons at  $\text{ICl}^-$  molecule ( $\Gamma^-$  monomer) and a complex of two iodine ions ( $\Gamma^-$  dimer) [1,2]. However, optical and luminescence properties of heavily iodine-doped alkali chloride crystals have not been examined sufficiently so far. Recently our group have studied luminescence properties of KCl heavily doped with KI as reported in ref. [3]. The present report describes the results of RbCl heavily doped with RbI.

The crystals of RbCl:I were grown by the Bridgeman method from reagent grade RbCl added with an appropriate amount of RbI (up to 5 mol %). The optical measurements were made at 15 K at BL3B station.

In dilute crystals, the photoluminescence spectra were almost the same as those of the previous studies [4,5]: three luminescence bands peaking at 2.46 eV (monomer emission), 4.38 eV (dimer emission) and at 5.76 eV (NE emission). Photoexcitation spectra for the dimer emission are shown in Fig. 1 for various RbI mol % crystals detected at 4.38 eV. The each spectrum has been normalized at unity at the maximum. The excitation peaks at 6.25 and 6.78 eV of 0.01 mol % crystal move toward the lower energy side with increasing RbI concentration. The low energy shift of the excitation bands suggests that there coexist dimers, trimers and larger sizes of  $\text{I}^-$  ions (RbI cluster) in heavily-doped RbCl:I crystal as can be observed in heavily-doped KCl:I [3].

The luminescence energies of the trimers and clusters of  $\text{I}^-$  ions in heavily doped RbCl:I crystals are expected to be different from that of  $\Gamma^-$  dimers. We have examined the photoluminescence spectra excited at various photon energies. The results for 1 mol % crystal are shown in Fig. 2. It is clearly confirmed that the peak energy of the luminescence band moves towards the low energy side when excited with lower photon energy. These luminescence bands are supposed to be the composite bands due to radiative annihilation of the relaxed exciton at dimers, trimers and clusters of  $\text{I}^-$  ions [3].

In RbCl crystals containing RbI around 1 mol %, there exists a small amount of dimer centers as compared with monomers, and moreover the amount of trimers and clusters of RbI is extremely smaller than

those of monomers and dimers. However, the

luminescence intensities of such large-sized centers are found to be comparable with that of the dimer emission. This fact suggests that the excitons trapped in RbI clusters in heavily doped RbCl:I crystals would give the high luminescence efficiency.

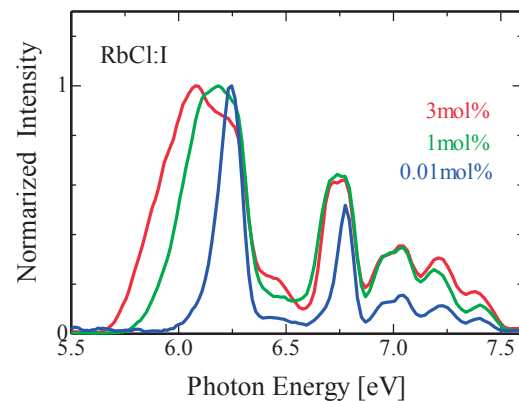


Fig. 1. Photoexcitation spectra of RbCl:I crystals detected at 4.38 eV for various RbI mol % at 15 K.

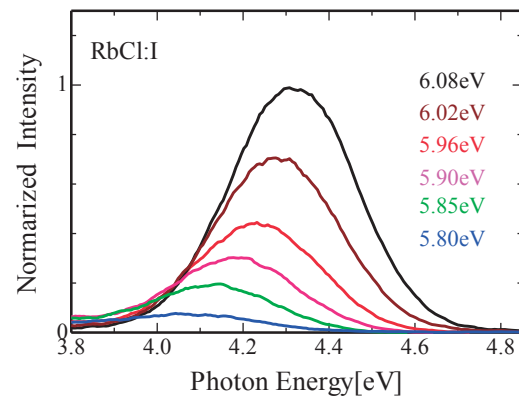


Fig. 2. Photoluminescence spectra of RbCl:I (1 mol%) crystal excited with various photon energies at 15 K.

- [1] N. Nagasawa, *J. Phys. Soc. Jpn.* **27** (1969) 1535.
- [2] K. Kan'no, K. Tanaka and T. Hayashi, *Rev. Solid State Sciences* **4** (1990) 383, and references therein.
- [3] A. Ohno and N. Ohno, *Phys. Status Solidi C* **8** (2011) 112.
- [4] O. Arimoto, K. Sasaki, H. Nakatani, K. Kan'no and Y. Nakai, *J. Lumin.* **31&32** (1984) 333.
- [5] K. Kan'no, H. Nakatani, T. Mukai, O. Arimoto, and Y. Nakai, *J. Phys. Soc. Jpn.* **55** (1986) 2433.

BL3B

## Near Band Edge Absorption Spectra and Green Band Excitation Spectrum of Boron-Doped Diamond Films

S. Kondou<sup>1</sup>, K. Fukui<sup>1</sup>, K. Yamamoto<sup>2</sup> and T. Inushima<sup>3</sup>

<sup>1</sup>Department of Electrical and Electronics Engineering, University of Fukui, Fukui 910-8507, Japan

<sup>2</sup>FIR Center, University of Fukui, Fukui 910-8507, Japan

<sup>3</sup>Department of Electronics, Tokai University, Hiratsuka 259-1292, Japan

Boron (B) is one of the best elements for p-type impurity of the diamond semiconductor devices. Boron-doped diamond (BDD) is also known as the blue diamond. Then, we have been measuring the CEES (Combined Excitation Emission Spectroscopy) around the band-gap (excitation energy 4.5 ~ 7.0eV) in order to clarify the electron state of BDD whose B concentrations is in the metal like - semiconductor transition region. In this study, we have focused on the CEES pattern differences of between BDDs and non B doped diamond (substrate) around the H3 emission band which consists of several sharp peaks and has the maximum peak at 2.47 eV.

The BDD films used in this study are grown on Ib-synthesized diamond substrates by the MPCVD (Microwave Plasma Chemical Vapor Deposition) method and their B concentration are 1000, 5000 and 10000 ppm [1]. All CEES measurements including the diamond substrate (0 ppm) have been performed at BL3B (and BL7B).

Figure 1 show the CEES patterns of both 1000 ppm and 10000 ppm BDD samples at 9 K. The horizontal and the vertical axes correspond to the emission photon energy and the excitation photon energy, respectively. Strong emissions around 2.4eV at low excitation photon energy region (<~6.0eV) are H3 emission band which are due to the nitrogen dimer defect (H3) centers in the substrate. The drastic intensity increases of the H3 emissions at 5.5 eV in Fig. 1 suggest that the indirect band gap locates at about 5.5 eV. On the other hand, at high excitation photon energy region (>~6.0eV), no H3 emission band has been observed in any samples without 0 ppm, because the excitation light cannot reach substrates through BDD thin films due to the strong absorption of BDD at high excitation photon energy region. However, 1000 ppm only show a different Gaussian type emission band whose peak locates at 2.3 eV. This emission band is probably assigned as the Green emission band that is often observed in the BDD. Figure 2 shows the excitation spectrum of the Green emission band. We believe that this is the first excitation spectrum of this emission band.

From the above description, the excitation photon energy dependence of the H3 emission band intensity represents the photon energy dependence of the transmittance of the BDD thin film. Then, we try to make the near band edge absorption spectra of the BDD thin films. Figure 3 shows the absorption

spectra of 1000 ppm, 5000 ppm and 10000 ppm BDD thin films.

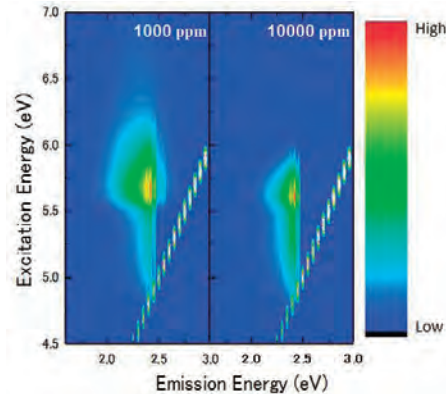


Fig. 1. CEES patterns of 1000 ppm (left) and 10000 ppm (right) BDD samples at 9 K.

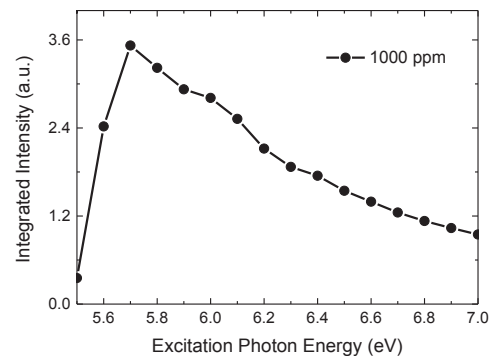


Fig. 2. Excitation spectrum of the Green emission band.

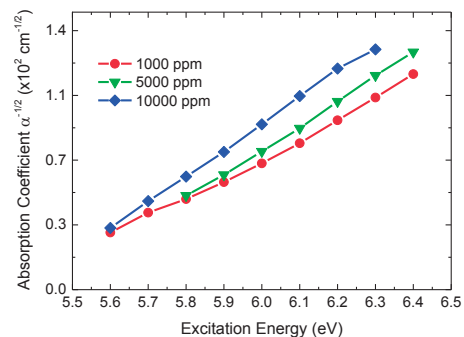


Fig. 3. Absorption spectra of 1000 ppm, 5000 ppm and 10000 ppm BDD thin films.

[1]A. Ogasawara, T. Inushima, T. Shiraishi, S. Ohya, S. Karasawa and H. Shiomi, *Diamond Related Mater.* **6** (1997) 835.

BL3B

## Optical Properties of SrCeO<sub>3</sub> Crystals

H. Numata<sup>1</sup>, M. Kitaura<sup>2</sup>, S. Watanabe<sup>3</sup>, S. Kurosawa<sup>4</sup>, K. Yubuta<sup>4</sup> and A. Ohnishi<sup>2</sup>

<sup>1</sup>School of Science and Technology, Yamagata University, Yamagata 990-8560, Japan

<sup>2</sup>Department of Physics, Faculty of Science, Yamagata 990-8560, Japan

<sup>3</sup>Department of Materials, Physics and Energy Engineering, Graduate School of Engineering, Nagoya University, Nagoya 464-8063, Japan

<sup>4</sup>Institute for Materials Research, Tohoku University, Sendai 980-8577, Japan

From analogy with CeO<sub>2</sub>, the electronic state of SrCeO<sub>3</sub> is considered to be in the mixed-valence state due to mixing between  $4f^0$  and  $4f^1L^{-1}$  configurations, where  $L^{-1}$  denotes the hole in valence band mainly composed O-2p orbitals [1]. The mixed valence state results from hybridization between O-2p and Ce-4f orbitals. Basically, Ce-4f electrons have localized character. However, it is considered that they have itinerant character, owing to the mixed valence state. Since either localization or itinerancy should be reflected in the conductive behavior of Ce-4f electrons, photoconductivity experiment is favorable to investigate the dynamical behavior of Ce-4f electrons in photoexcited SrCeO<sub>3</sub>. As a first step, we have measured photoabsorption (PA), photoluminescence (PL), PL excitation (PLE) spectra of SrCeO<sub>3</sub> crystals, in order to obtain fundamental optical properties. These data provide us information on creation and relaxation processes of Ce-4f electrons and O-2p holes.

SrCeO<sub>3</sub> crystals were grown in air by a Floating zone method. They were annealed under oxygen atmosphere for 24h at 1070K. Crystal surfaces were mechanically polished. Experiment was performed at the beamline BL3B in UVSOR facility. PA spectra were obtained by detecting incident and transmitted light with a calibrated silicon photodiode. PL and PLE spectra were measured using the combination of a grating monochromator and a CCD detector or a photomultiplier, respectively. PLE spectra were corrected for the energy distribution of excitation light source.

Figure 1 shows PA (green line), PL (blue line) and PLE (red line) spectra, which were measured at 9 K. The PA spectrum exhibits the fundamental absorption edge at 2.46 eV. According to the electronic structure calculation reported previously, such a rapid increase is ascribed to the formation of the charge transfer (CT) excitons which are composed of Ce-4f electrons and O-2p holes. A PL band appears around 2.30 eV under excitation at 4.81 eV. A similar band is observed in PL spectra of Sr<sub>2</sub>CeO<sub>4</sub> [4]. The PLE spectrum for the 2.30 eV band shows that it is excited in the energy region above 3.46 eV. The intensity of the 2.30 eV band reaches the maximum at 4.07 eV, and is gradually decreased with increasing photon energy.

The 2.30 eV band is excited in the fundamental absorption region. This result suggests that the 2.30

eV band is an intrinsic feature in SrCeO<sub>3</sub>. This band has the Stoke shift of 0.30 eV. It is likely to consider that the 2.30 eV band originates from the relaxed state of a CT exciton, which may localizes on a octahedral (CeO<sub>6</sub>)<sup>8-</sup> complex ion.

The threshold for excitation of the 2.30 eV band is not agreement with the fundamental absorption edge. Such a disagreement implies that CT excitons annihilate nonradiatively under photoexcitation near the fundamental absorption edge. There are two possible explanations for this. One is that CT excitons transfer their energy to lattice imperfections before lattice relaxation. The other is that CT excitons immediately relax to the ground state without emitting 2.30 eV band. The missing of 2.30 eV band is an open problem to be solved, and details of it will be clarified by photoconductivity experiment.

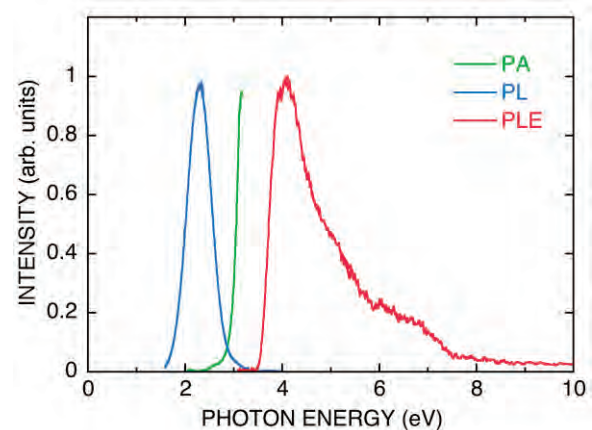


Fig. 1. PA (green line), PL (blue line), and PLE (red line) spectra of SrCeO<sub>3</sub> crystals measured at 9K.

- [1] A. Fujimori *et al.*, Phys. Rev. B **28** (1983) 2281.
- [2] M. Niwano *et al.*, J. Phy. Soc. Jpn. **57** (1988) 1489.
- [3] H. Numata *et al.*, UVSOR Activity Report 2013 **41** (2014) 63.
- [4] L. V. Peterson *et al.*, J. Electrochem. Soc. **147** (2000) 4688.

BL3B

## VUV Absorption Spectra of Alanine Single Crystals

S. Tanaka, M. Kitaura, A. Ohnishi and M. Sasaki

Department of Physics, Faculty of Science, Yamagata University, Yamagata 990-8560, Japan

Amino acids are simple chiral molecules with L- and D-forms. Protein molecules are composed of only L-amino acids. This is called “homochirality”, which has attracted much attention in relation to the mystery of life. It has been generally accepted that the homochirality of proteins come from the creation of L-amino acids by circularly polarized VUV light in outer space region. So far, VUV absorption spectra of amino acids have been studied using their aqueous solutions [2] and thin films [3]. To our knowledge, there is no report on VUV absorption spectra of amino acid single crystals. In the present study, VUV absorption spectra of alanine crystals have been measured to provide the true absorption spectrum of it, and to verify the validity of natural circular dichroism spectra already reported [4].

The alanine single crystals were obtained by the slow evaporation from saturated aqueous solution of commercial L-alanine reagent (SIGMA-ALDRICH, purity > 99.5%). The photograph of an alanine single crystal used in our experiment is shown in Fig. 1. The crystal structure of alanine is orthorhombic, and orthogonal crystalline axes exist in the cleavage place. They were distinguished by two polarizers arranged in a cross Nicole alignment. However, it could not be determined which are they among *a*, *b* and *c* crystalline axes.

Figure 2 shows the VUV absorption spectra of an alanine single crystal for different configurations of linearly polarized light. These data were obtained by the Kramers-Kronig analysis from the VUV reflectivity spectra in 5-30 eV range measured at room temperature. A number of peaks are observed in 5-10 eV range. They show remarkable linear dichroism, which has not been found in Refs. 2 and 3. A broad peak is observed in around the 14.0 eV. This peak has been reported in Ref. 4. The VUV absorption spectra of an alanine crystal are shown in an expanded scale of 5-12 eV. They are composed of peaks around 6.0, 6.8, 7.5, 8.0, 9.2, and 10.0 eV. In Ref. 4, the natural circular dichroism spectrum of a L-alanine deposit thin film exhibited peaks at 6.8 and 8.0 eV and dips at 6.2 and 7.5 eV. Since the energies are in good agreement with those of absorption peaks in Fig. 3, we can say that there is no doubt on the validity of natural circular dichroism spectra in Ref. 4.



Fig. 1. Photograph of an alanine crystal used in our experiment.

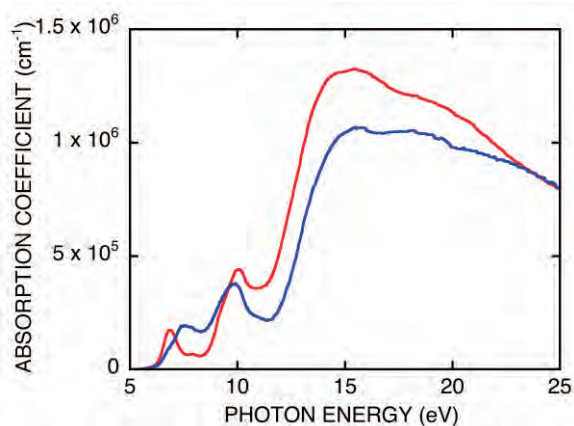


Fig. 2. VUV absorption spectra of an alanine crystal, which were obtained by the Kramers-Kronig analysis from reflectivity spectra in 5-30 eV range measured at room temperature.

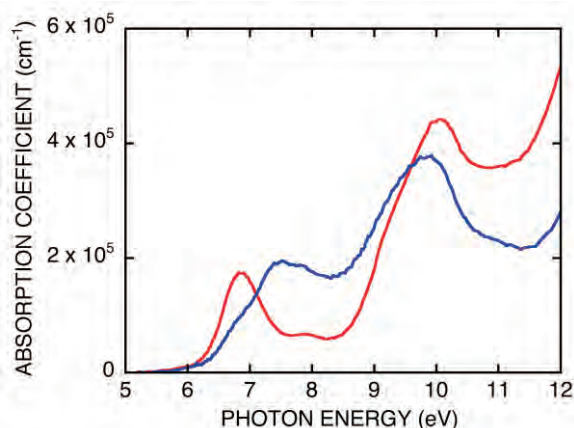


Fig. 3. VUV absorption spectra of an alanine crystal in an extended scale of 5-12 eV.

- [1] P. A. Snyder *et al.*, *Biopolymers* **12** (1973) 975.
- [2] T. Inagaki *et al.*, *Biopolymers* **12** (1973) 1353.
- [3] M. Tanaka *et al.*, *J. Electron Spectrosc. Relat. Phenom.* **181** (2001) 177.
- [4] F. Kaneko *et al.*, *J. Phys. Soc. Jpn.* **78** (2009) 013001.

BL3B

## Temperature Dependence of Absorption Spectra for Ce<sup>3+</sup>-Doped Y<sub>3</sub>Al<sub>5</sub>O<sub>12</sub> Single Crystals

S. Watanabe<sup>1</sup>, M. Nakaya<sup>1</sup>, J. Onoe<sup>1</sup>, M. Kitaura<sup>2</sup>, K. Kamada<sup>3</sup> and A. Ohnishi<sup>2</sup>

<sup>1</sup>Department of Materials, Physics and Energy Engineering, Graduate School of Engineering, Nagoya University, Nagoya 464-8603, Japan

<sup>2</sup>Department of Physics, Faculty of Science, Yamagata University, Yamagata 990-8560, Japan

<sup>3</sup>New Industry Creation Hatchery Center, Tohoku University, Sendai 980-8579, Japan

Ce<sup>3+</sup>-doped Y<sub>3</sub>Al<sub>5</sub>O<sub>12</sub> (Ce:YAG) have been widely studied for application as a yellow phosphor used in white light LEDs. The basic research on optical properties for Ce:YAG is important issues for development of luminescent materials. In addition, the detailed analysis based on a first-principles calculation is useful for understanding the optical properties of luminescent materials.

In this study, we have performed experimental and theoretical investigation of the temperature dependence of the 4*f*-5*d* absorption spectra for Ce:YAG single crystals.

The single crystals of Ce:YAG were grown by the micro pulling down method. The concentration of Ce<sup>3+</sup> was 1 mol%. The 4*f*-5*d* absorption spectra were measured at 9 and 312 K. These absorption spectra were analyzed by using a first-principles configuration interaction calculation [1,2]. The effects of lattice relaxation due to the substitution of Y<sup>3+</sup> by Ce<sup>3+</sup> were considered using the optimized structure estimated by a first-principles DFT calculation.

Figure 1 shows the experimental 4*f*-5*d* absorption spectra of Ce:YAG at 9 and 312 K, respectively. Three major peaks A, B and C were observed in both spectra. These peaks can be attributed to the Ce<sup>3+</sup> 4*f*-5*d* absorption peaks. The peak intensities depend upon temperature. As shown in Fig. 1, the intensity of peak B at 9 K increases, compared with that at 312 K. In order to investigate the effects of thermal excitation, we calculated the oscillator strengths for the transitions from two different initial states since the Ce<sup>3+</sup> 4*f*<sub>5/2</sub> level slightly splits due to the crystal field. Figure 2 shows the theoretical 4*f*-5*d* absorption spectra of Ce:YAG. Figure 2(a) shows the oscillator strengths from the lowest 4*f*<sub>5/2</sub> level, and Fig. 2(b) shows the oscillator strengths from the higher-lying 4*f*<sub>5/2</sub> level which is 0.108 eV higher than the lowest level. The oscillator strength of the peak B for the transition from the higher-lying 4*f*<sub>5/2</sub> level is significantly strong, compared to that from the lowest level. This result clearly indicates that the origin of the strong temperature dependence of the peak B in the experimental spectra can be ascribed to the change of re-distribution of electron population inside the 4*f*<sub>5/2</sub> level by the initial state due to the thermal excitation.

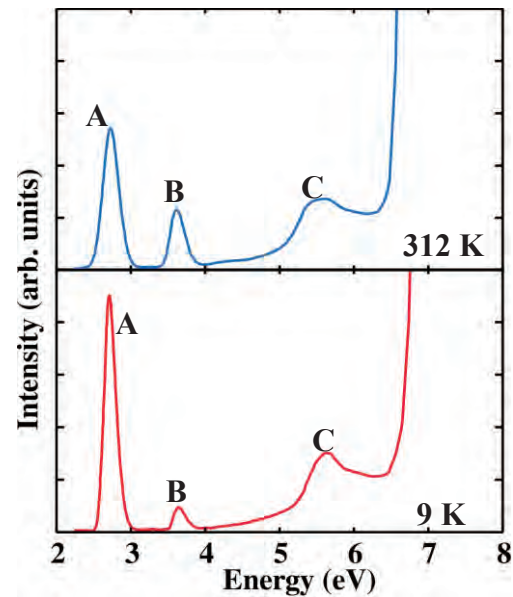


Fig. 1. Experimental absorption spectra of Ce:YAG at 9 and 312 K.

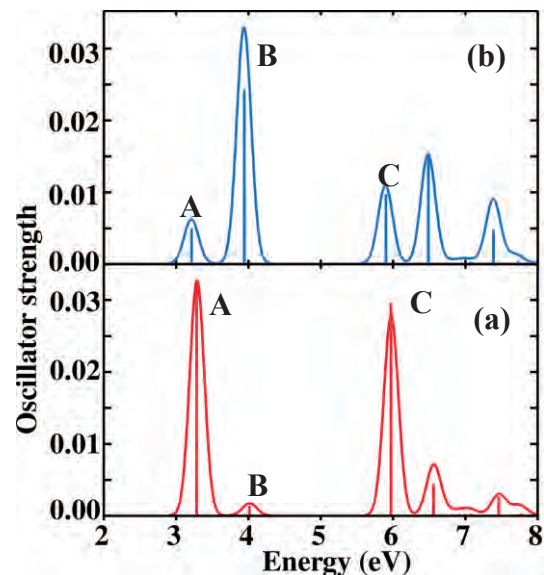


Fig. 2. Theoretical absorption spectra of Ce:YAG. (a) Oscillator strengths from the ground state of 4*f*<sub>5/2</sub> level. (b) Oscillator strengths from second-lowest 4*f*<sub>5/2</sub> level.

[1] K. Ogasawara *et al.*, Phys. Rev. B **64** (2001) 143.

[2] S. Watanabe *et al.*, Phys. Rev. B **81** (2010) 125128.

BL3B

## Two-Band Luminescence from an Intrinsic Defect in Spherical and Terraced MgO Nanoparticles

P. V. Pikhitsa<sup>1</sup>, C. Kim<sup>1</sup>, S. Chae<sup>1</sup>, S. Shin<sup>1</sup>, S. Jung<sup>1</sup>, M. Kitaura<sup>2</sup>,  
S. Kimura<sup>3</sup>, K. Fukui<sup>4</sup> and M. Choi<sup>1</sup>

<sup>1</sup>Global Frontier Center for Multiscale Energy Systems, Division of WCU Multiscale Mechanical Design, School of Mechanical and Aerospace Engineering, Seoul National University, Seoul 151-744, Korea

<sup>2</sup>Department of Physics, Faculty of Science, Yamagata University, Yamagata 990-8560, Japan

<sup>3</sup>UVSOR Facility, Institute for Molecular Science and the Graduate University for Advanced Studies, Okazaki 444-8585, Japan

<sup>4</sup>Department of Electrical and Electronics Engineering, Faculty of Engineering, University of Fukui, Fukui 910-8507, Japan

Magnesium oxide nanocubes obtained by the self-combustion of Mg metal have long exhibited only a broad 2.9 eV cathodoluminescence (CL) band owing to oxygen vacancies ( $F$  centers). In our work, a room-temperature ultraviolet 4.8 eV CL band has been observed coincident with a 2.5 eV band of the same intensity from an unexplored intrinsic defect in MgO terraced nanocubes and nanospheres produced from Mg metal during combustion in an  $H_2/O_2$  flame. Synchrotron radiation excitation spectra reveal that the excitation energy at the onset of both bands is just above the bandgap energy of 7.7 eV, where electrons and holes are generated (see Fig. 1).

Figure 1 compares the PL spectra, taken at 8 K, for photon excitation energies swept through the forbidden band and up to 10 eV from the UV-MgO (Fig. 1(a)) and the non-UV-MgO cubes (Fig. 1(b)). It is clear that the two PL bands observed in CL arise simultaneously at 7.7 eV and persist as the excitation energy sweeps deeper into the conduction band (Fig. 1(a)). This is a strong indication that both bands (marked by red circles in Fig. 1(a)) have the same origin and that electrons and holes from the conduction band are solely responsible and necessary for the excitation of the two bands, similar to the electron and hole “shower” in CL, when it is understood that a photon of 8 eV leads to the formation in MgO of a conduction electron and a hole that do not undergo transformation into a self-trapped state.

We determine that a defect, responsible for both emission bands, creates proximal anion-cation vacancy pairs named  $P$  centers that may appear instead of  $F$  centers because of changes in the MgO nanoparticle growth conditions.

The discovery of two-band room-temperature CL from spherical and terraced MgO nanoparticles may find applications in defect-center lasers based upon MgO and in spectral transformers.<sup>1</sup> The two-band CL may also have applications in the geosciences because its presence or absence should be useful to distinguish the history of MgO formation in the Earth's mantle or in planetary nebula.

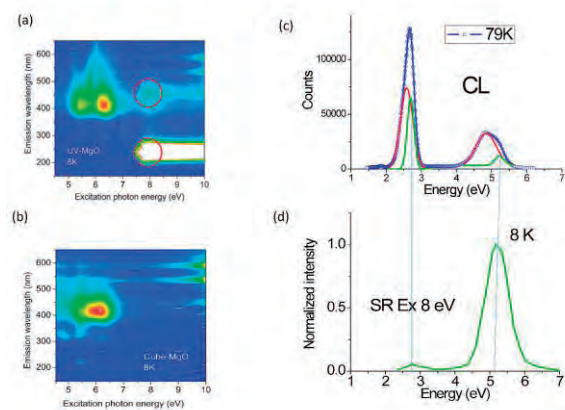


Fig. 1. Photoluminescence spectra vs. excitation energy from synchrotron radiation (intensity grows from blue to red). (a) Red circles marking correlated emission bands at 4.8 eV (upper) and 2.5 eV (lower) from UV-emitting MgO. The  $F^+$  band at 420 nm is from the non-UV-MgO present in the powder sample. (b) Emission from non-UV-MgO cubes, where the  $F^+$  band at 420 nm is present but the 4.8 and 2.5 eV bands are absent. (c) CL spectrum for UV-MgO taken at 79 K (blue) and the deconvoluted spectral peaks (red and green curves). The additional two-band spectrum (green curve) is compared with (d) the two-band synchrotron radiation spectrum (not corrected for intensity magnitude) excited at 8 eV and 8 K taken from (a).

[1] A. Lushchik, E. Feldbach, R. Kink, Ch. Lushchik, M. Kirm and I. Martinson, Phys. Rev. B **53** (1996) 5379.

BL4U

## Scanning Transmission X-Ray Microscopy Study on Fluorescence Mechanism of Nanocarbon-Silica Composites

S. Kawasaki, H. Song and Y. Takeuchi

*Nagoya Institute of Technology, Nagoya 466-8555, Japan*

Mesoporous carbon-silica (MPCS) composites synthesized by tri-constituent co-assembly method have fascinating nano-space structures. We have investigated Li-ion battery anode and EDLC electrode properties of the composites. In the course of the investigation we found that mesoporous carbon-silica composites exhibit very intense visible photoluminescence under low-energy ultra-violet light irradiation.[1-5] Now, a class of stable, efficient, inexpensive and less toxic photoluminescent materials which emit white light under long-wavelength UV light is strongly required to replace fluorescent lamps by LED lamps. The composites we synthesized satisfy the required conditions and are the promising materials from the environmental point of view. However, detailed mechanism of the fluorescence property of MPCS has not been understood well. Then, in order to understand the mechanism, we performed scanning transmission x-ray microscopy (STXM) measurements of MPCS samples.

MPCS samples were prepared by tri-constituent co-assembly method. Tetraethyl orthosilicate (TEOS) and resol are used as silica and carbon sources, respectively. Tri-block co-polymer (BASF F-127) was used as a soft template. Carbonization was done in nitrogen atmosphere at 1170 K. Oxidation was done in air at 720 K. The obtained MPCS samples were characterized by TEM, SEM, XRD, Raman, and N<sub>2</sub> adsorption measurements. STXM measurements were performed at BL-4U of UV-SOR of Institute for Molecular Science, Okazaki, Japan.

Figure 1 shows the observed C K-edge X-ray absorption spectrum of MPCS sample. For usual bulk carbon samples, sharp  $\pi^*$  absorption peak is observed at around 285 eV. However, as shown in Fig. 1, for MPCS sample, the peak at around 285 eV is very broad and the peak-top is observed at about 288 eV. The cluster size of nanocarbons remained in MPCS sample after the oxidation treatment should be very small. If  $\pi$  conjugation scale is decreased,  $\pi$ - $\pi^*$  gap should be widen. This would be the reason why the peak-top of  $\pi^*$  absorption of MPCS sample is observed at higher energy than usual bulk carbon samples. To confirm the validity of this hypothesis, we should perform STXM measurements of several kinds of MPCS samples having different carbon cluster sizes.

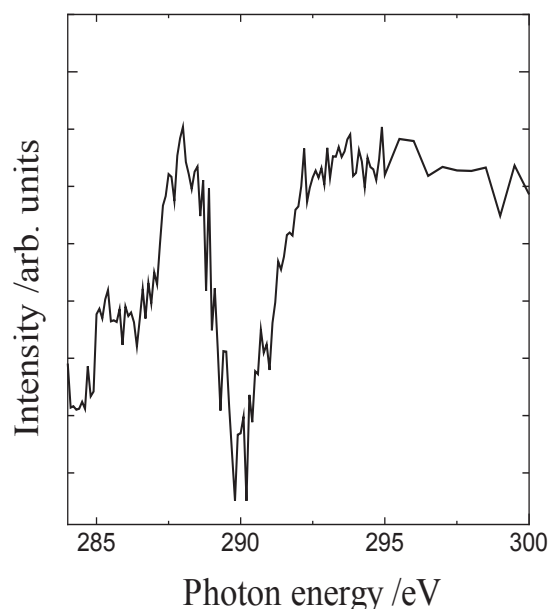


Fig. 1. Carbon K-edge X-ray absorption spectra of mesoporous carbon-silica composite sample.

- [1] Y. Ishii, A. Matsumura, Y. Ishikawa and S. Kawasaki, *Jpn J. Appl. Phys.* **50** (2011) 01AF06-1.
- [2] Y. Ishikawa, K. Sato, S. Kawasaki, Y. Ishii, A. Matsumura and S. Muto, *physica status solidi (a)* **209** (2012) 1022.
- [3] K. Sato, Y. Ishikawa, Y. Ishii, S. Kawasaki, S. Muto and Y. Yamamoto, *Jpn. J. Appl. Phys.* **51** (2012) 08240.
- [4] Y. Ishikawa, S. Kawasaki, Y. Ishii, K. Sato and A. Matsumura, *Jpn. J. Appl. Phys.* **51** (2012) 01AK02.
- [5] Y. Ishii, Y. Nishiwaki, A. Al-zubaidi and S. Kawasaki, *J. Phys. Chem. C* **117** (2013) 18120.

BL4U

## The Effect of Carbon Bombardment of ZnO Probed by Scanning Transmission X-Ray Microscopy

Y. F. Wang<sup>1</sup>, S. H. Hsieh<sup>1</sup>, J. W. Chiou<sup>2</sup>, W. F. Pong<sup>1</sup>, T. Ohigashi<sup>3</sup> and N. Kosugi<sup>3</sup>

<sup>1</sup>Department of Physics, Tamkang University, Tamsui 251, Taiwan

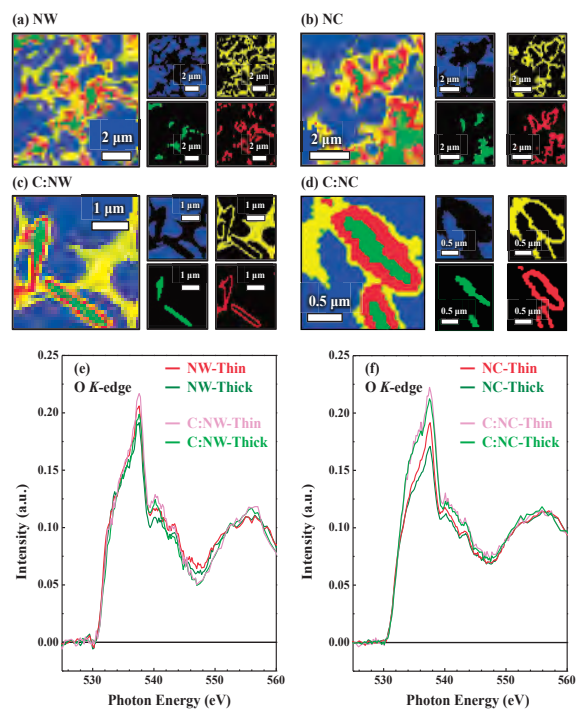
<sup>2</sup>Department of Applied Physics, National University of Kaohsiung, Kaohsiung 811, Taiwan

<sup>3</sup>UVSOR Facility, Institute for Molecular Science, Okazaki 444-8585, Japan

In the present work, the effect of carbon bombardment of ZnO nanowires (NW) and nanocactus (NC) has been studied using X-ray-based microscopic and spectroscopic techniques. Figures 1(a-d) display the O *K*-edge scanning transmission X-ray microscopy (STXM) stack mappings of randomly selected sample regions of ZnO NW and NC before and after carbon bombardment (C:NW and C:NC). The stack mappings are decomposed into blue, yellow, red and green maps (right panels), which correspond to the regions that are associated with different thickness and spectroscopic variations of the samples. Overall, the divisions of the mappings into thick (green), thin (red), carbon lacing (yellow) and background (blue) regions were generated via principle component analysis (PCA) for cluster analysis based on spectroscopic differences. The O *K*-edge STXM-XANES (X-ray Absorption Near-Edge Structure) spectra in the Figs. 1(e) and 1(f) are the sum of the corresponding XANES spectra of the thick (green) and thin (red) regions of ZnO NW and NC before and after C bombardment, respectively.

As displayed in Figs. 1(e) and 1(f), according to the dipole-transition selection rule, the near features at ~535-550 eV in the O *K*-edge STXM-XANES spectra are attributed to the electron excitations from O *1s*-derived states to *2p<sub>σ</sub>*-derived (along the bilayer) and O *2p<sub>π</sub>*-derived (along the *c* axis) states, which are approximately proportional to the density of the unoccupied O *2p*-derived states. The O *K*-edge STXM-XANES spectra clearly reveal that the intensities of near features in the thin regions are higher than those in the thick regions of ZnO NC/NW and C:NC/C:NW. The enhanced intensities of the near features in the O *K*-edge STXM-XANES spectra can result in a higher population of defects in the thin or surface/edge regions because of the non-stoichiometric chemical composition or dangling bonds.[1]

Additionally, the intensities of near features of ZnO C:NC/C:NW samples (after C bombardment) are also higher than those in ZnO NC/NW samples (before C bombardment), further suggesting that the bombarding C atoms may play an important role to enhance density of the unoccupied O *2p*-derived states.



Figs. 1. (a)-(d): O *K*-edge scanning transmission X-ray microscopy (STXM) stack mappings of randomly selected sample regions of ZnO NW and NC before and after carbon bombardment (C:NW and C:NC). The spatial distribution of background (blue), carbon lacing (yellow), thick (green) and thin (red) regions of samples. (e) and (f): The O *K*-edge STXM-XANES spectra are the sum of the corresponding XANES spectra between the thin (red) and thick (green) regions of ZnO NW and NC before and after C bombardment, respectively.

[1] S. B. Singh *et al.*, *Nanoscale* **6** (2014) 9166.

BL4U

## Chemical Redox of Mesoscopic NiO/CH<sub>3</sub>NH<sub>3</sub>PbI<sub>3</sub> Perovskite Heterojunction by Scanning Transmission X-Ray Microscopy

M. W. Lin<sup>1</sup>, K. C. Wang<sup>2</sup>, L. T. Chang<sup>1</sup>, Y. L. Lai<sup>1</sup>, T. Ohigashi<sup>3</sup>, N. Kosugi<sup>3</sup>, P. Chen<sup>2</sup> and Y. J. Hsu<sup>1,2</sup>

<sup>1</sup>National Synchrotron Radiation Research Center, Hsinchu 300, Taiwan

<sup>2</sup>Department of Photonics, National Cheng Kung University 701, Tainan, Taiwan

<sup>3</sup>Institute for Molecular Science, Okazaki 444-8585, Japan

Organometal trihalide perovskite-based solar cells have exhibited high power conversion efficiencies when incorporated into mesoscopic NiO (NiO<sub>nc</sub>) hole-transport layers [1]. Herein we studied the origin of such high efficient carrier transport in terms of electronic and chemical properties of perovskite-NiO<sub>nc</sub> heterojunction by x-ray photoelectron spectroscopy (XPS), Near-edge X-ray absorption fine structure (NEXAFS), and scanning transmission X-ray microscopy (STXM).

From our previous studies, we found a pronounced chemical redox between CH<sub>3</sub>NH<sub>3</sub>PbI<sub>3</sub> perovskite-NiO<sub>nc</sub> heterojunction that PbI<sub>2</sub> is oxidized to PbO and subsequently produce hole-dopant CH<sub>3</sub>NH<sub>3</sub>PbIO at the heterojunction. From the O *K*-edge spectra in an auger-electron-yield (AEY) mode, we observed an extra distinct peak at 535 eV for ITO/NiO<sub>nc</sub>/CH<sub>3</sub>NH<sub>3</sub>PbI<sub>3</sub> in comparison to pristine NiO<sub>nc</sub>. This additional peak is apparently produced by the contact reaction at heterojunction of NiO<sub>nc</sub>/CH<sub>3</sub>NH<sub>3</sub>PbI<sub>3</sub>. As a result, the generation of hole-doping CH<sub>3</sub>NH<sub>3</sub>PbIO at NiO<sub>nc</sub>/perovskite heterojunction plays a critical role to facilitate the carrier transport, and thus enhance the solar cell efficiencies.[2]

To further confirm the redox reaction at NiO<sub>nc</sub> and CH<sub>3</sub>NH<sub>3</sub>PbI<sub>3</sub> perovskite heterojunction, chemical maps of oxygen distributions within microaggregates of SiN/NiO<sub>nc</sub>/CH<sub>3</sub>NH<sub>3</sub>PbI<sub>3</sub> are studied by STXM. Figure 1 displays the STXM images of SiN/NiO<sub>nc</sub>/CH<sub>3</sub>NH<sub>3</sub>PbI<sub>3</sub>, which are optical density (OD) maps obtained at (a) 532.1 eV and (b) 535.1 eV, the characteristic absorption peaks of NiO<sub>nc</sub> and CH<sub>3</sub>NH<sub>3</sub>PbIO, respectively as mentioned above. The Pb OD map of the SiN/NiO<sub>nc</sub>/CH<sub>3</sub>NH<sub>3</sub>PbI<sub>3</sub> as shown in Figure 1b is obtained at 610 eV. These image mappings of O and Pb on SiN/NiO<sub>nc</sub>/CH<sub>3</sub>NH<sub>3</sub>PbI<sub>3</sub> show similar elemental distribution in morphology and size except the contrast. As a result, we anticipate that the Pb is bonded with O and located on the mesoporous structure of NiO<sub>nc</sub>. The image acquired at 532.1 eV which is composed of major characters of O 2p and Ni 3d orbitals, exhibits weaker image contrast than that obtained at 535.1 eV, indicating the NiO<sub>nc</sub> is involved in the interfacial redox reaction at heterojunction. The more redox occurs, the lower the peak intensity of 532.1 eV and thus the weaker the contrast displays.

The corresponding micro NEXAFS spectra as the cross marks shown in Figure 1 are displayed in Figure 2a and 2b for O *K*-edge and Pb *N*-edge, respectively. In comparison with pristine NiO<sub>nc</sub> (as shown in the inset of Figure 2b), the spectra show decreased peak intensity at 532.1 eV and broader peak width between 535-545 eV. The micro NEXAFS of Pb *N*-edge in Figure 2c express similar shape and intensity. Our results suggest that the redox is occurred at heterojunction and the formation of perovskite is located in the mesoporous structure of NiO<sub>nc</sub>.

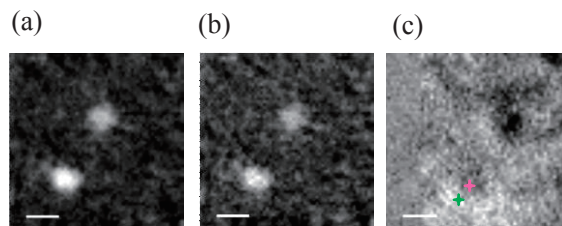


Fig. 1. The OD images of O *K*-edge at (a) 532.1 eV, (b) 535.1 eV, and (c) Pb *N*-edge at 654 eV from SiN/NiO<sub>nc</sub>/CH<sub>3</sub>NH<sub>3</sub>PbI<sub>3</sub>.

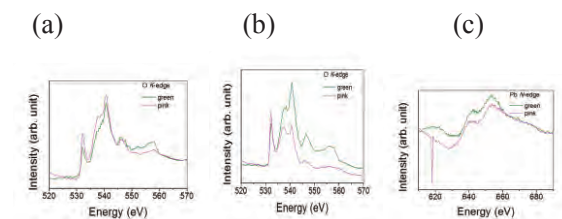


Fig. 2. Micro-NEXAFS spectra of the O *K*-edge and Pb *N*-edge extracted from the Figure 1a, 1b, and 1c, respectively. The inset in Figure 2a shows the O *K*-edge NEXAFS of pristine NiO<sub>nc</sub>.

[1] K. C. Wang, J. Y. Jeng, P. S. Shen, Y. C. Chang, E. W.-G. Diau, C. H. Tsai, T. Y. Chao, H. C. Hsu, P. Y. Lin, P. Chen, T. F. Guo and T. C. Wen, *Sci. Rep.* **4** (2014) 4756.

[2] Ming-Wei Lin, Kuo-Chin Wang, Yu-Ling Lai, Takuji Ohigashi, Nobuhiro Kosugi, Peter Chen, Tzung-Fang Guo and Yao-Jane Hsu, "Chemical Redox of Mesoscopic NiO/CH<sub>3</sub>NH<sub>3</sub>PbI<sub>3</sub> Perovskite Interfaces for High Efficient Solar Cell", in preparation.

BL4U

## Characterization of Monolithic Polymers Containing Nanoparticles by Scanning Transmission X-Ray Microscopy (STXM)

D. Arrua<sup>1</sup>, C. Desire<sup>1</sup>, A. Khodabandeh<sup>1</sup>, T. Ohgashi<sup>2</sup>, N. Kosugi<sup>2</sup> and E. Hilder<sup>1</sup>

<sup>1</sup>Australian Centre for Research on Separation Science (ACROSS), School of Chemistry, University of Tasmania, Private Bag 75, Hobart 7001, Australia

<sup>2</sup>UVSOR Facility, Institute for Molecular Science, Okazaki 444-8585, Japan

Monolithic polymers are a new generation of stationary phases for chromatography, offering significant benefits over currently particle-based materials. The main characteristic of these materials is the presence of large through-pores which permits the use of high flow rates at low backpressures [1]. However, improvements in this technology rely on being able to accurately characterize the porous structure and new characterization techniques are needed to better understand the polymer morphology and its optimization. In this sense, the relatively high penetration power of X-rays would allow a comprehensive analysis of the radial and longitudinal heterogeneity of the monolithic materials developed in our research group.

The characterization by STXM of polymer monoliths was performed at the BL4U beamline of the UVSOR synchrotron radiation facility. To obtain a suitable sample for STXM studies, the macroporous styrene-divinylbenzene (Sty-DVB) monolith with encapsulated hydroxyapatite (HAP) and titanium dioxide (TiO<sub>2</sub>) nanoparticles was embedded with an aliphatic epoxy resin specially designed for STXM analysis [2]. The experiments were performed at the C-K, Ca-L and Ti-L edges. Figure 1 shows the NEXAFS spectra for both the HAP and TiO<sub>2</sub> nanoparticles. Both spectra show several peaks which are a result of the combination of spin-orbit splitting between the 2p and 3d orbitals [3, 4].

The spectrum of the Sty-DVB polymer has a peak at 285.2 eV which corresponds to the C 1s → π\*<sub>C=C</sub> transition of aromatic systems (spectrum not shown).

These spectroscopic differences allowed identification and mapping of each type of nanoparticle within the polymer monolith. Figure 2 presents STXM optical density (OD) images at three different energies of a monolith containing 5% wt/wt of each nanoparticle. It is possible to see the HAP nanoparticles at 349 eV (Fig. 2. panels a and d), the TiO<sub>2</sub> nanoparticles at 460.4 eV (Fig. 2. panels b and e) and the polymer scaffold at 285.2 eV (Fig. 2. panels c and e). These OD images display the spatial distribution of each type of nanoparticle within the polymeric scaffold.

Ongoing studies in our research group are focused in the application of these composite materials as solid supports for liquid chromatography and solid phase extraction.

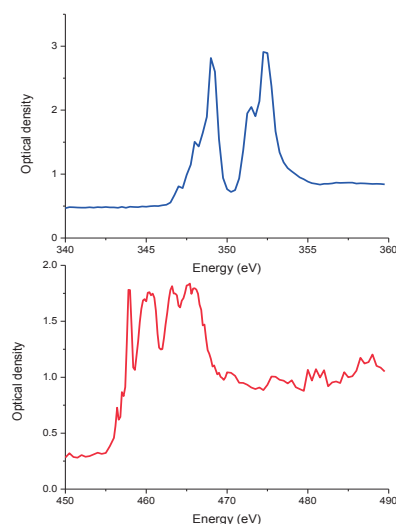


Fig. 1. NEXAFS spectra of HAP (top) and the TiO<sub>2</sub> (bottom) nanoparticles.

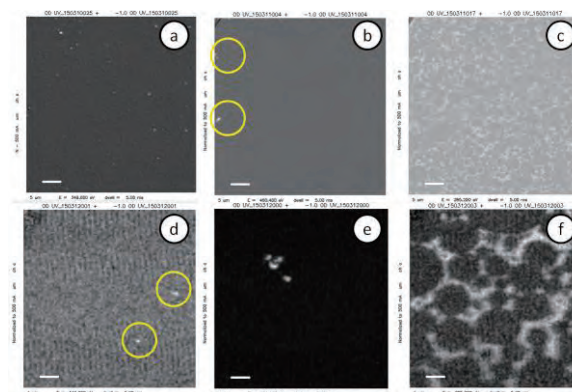


Fig. 2. STXM optical density (OD) images at (a and d) 349, (b and e) 460.4 and (c and f) 285.2 eV. Scale bars = 5 μm (a-c) and 1 μm (d-e).

- [1] R. D. Arrua *et al.*, *Analyst* **137** (2012) 5179.
- [2] A. P. Hitchcock *et al.*, *J. Electron Spectrosc.* **156** (2007) 467.
- [3] S. Hanhan *et al.*, *J. Electron Spectrosc. Relat. Phenom.* **172** (2009) 44.
- [4] H. Zhang *et al.*, *J. Chem. Phys.* **136** (2012) 174701.

BL4B

## O K-Edge Spectroscopy of High Valence State Mn(V) Oxides

Y. Aoki, T. Kobayashi, K. Kuroda, E. Tsuji and H. Habazaki  
 Faculty of Engineering, Hokkaido University, Sapporo 060-8628, Japan

In naturally occurring photosystem II (PSII), the water oxidation reaction proceeds with extraordinary high catalytic activity, where a  $\mu$ -oxo bridged tetrameric Mn cluster ( $\text{Mn}_4\text{CaO}_5$ ) serves as the multielectron oxidation catalyst within a complex protein environment [1,2]. Thus, the Mn clusters of photosynthetic organisms have triggered extensive research efforts to develop efficient water oxidation catalysts composed of the inexpensive and abundant element Mn. In a recent year, various manganese oxides, such as  $\text{MnO}_2$ ,  $\text{BaMnO}_3$ ,  $\text{LaMnO}_3$  etc. has been reported to show an excellent electrocatalytic properties for oxygen evolution by electrochemical water splitting [3, 4]. Suntivich *et al* reported that hole on oxygen make an important role for oxygen evolution catalysis of manganese oxide [4]. Such a hole probably evolves by mixing of ligand-to-metal charge transfer (LMCT) state which tends to be involved in high valence state metal oxides due to the covalency of metal-O bonding. In fact, it is reported high valence state  $\text{Mn}^{\text{V}}=\text{O}$  intermediates are involved during water oxidation cycle (S-cycle) and make an important role for O-O bond formation from two water molecules [5].

$\text{Ba}_3\text{Mn}_2\text{O}_8$  is Mn(V) oxides and is thermally stable in ambient atmosphere. Recently, we found that  $\text{Ba}_3\text{Mn}_2\text{O}_8$  electrodes facilitate O-O peroxide species under the anodic polarization in neutral solutions. K-edge XAS spectroscopy can direct evidence of unoccupied state of solids. Accordingly, it is of fundamental and technological important to study the manganese oxide system by using this technique in order to clarify the relationship between oxygen hole and electrocatalysis. In this study, we investigate O K-edge spectra of  $\text{Ba}_3\text{Mn}_2\text{O}_8$  samples treated by anodic polarization at various potentials.

$\text{Ba}_3\text{Mn}_2\text{O}_8$  powders were prepared by calcining  $\text{BaCO}_3$  and  $\text{MnO}_2$  mixture at  $950^\circ\text{C}$  in dry air.  $\text{Ba}_3\text{Mn}_2\text{O}_8$ -base electrodes were prepared by mixing  $\text{Ba}_3\text{Mn}_2\text{O}_8$  and carbon powders with a teflon binder and uniaxially-pressed at 100 MPa. The electrodes were polarized at a constant anodic potential with an Ag/AgCl (sat. KCl) reference electrode in neutral  $\text{NaClO}_4$  solution (0.1 M).

O K-edge XAS spectra were recorded in a total electron yield mode by measuring bulk current through the irradiated samples. The spectra of the manganese oxide samples were shown in Fig. 1. The Mn atoms in  $\text{Ba}_3\text{Mn}_2\text{O}_8$  take tetrahedral coordination with oxygen atoms. Therefore, the pre-edge peaks at around 529 eV can be assigned to the transition to anti-bonding  $t_{2g}$  states. In case of  $\text{KMnO}_4$ , the Mn-O clusters take tetrahedral coordination, so that the

peaks at around 530 eV can be assigned to the transition to anti-bonding  $t_2$  states. The apparent changes in O K-edge spectra are not observed in the samples after the polarization at various potentials, as shown in Fig. 1. This might be due to the deterioration of the polarized specimens by exposing to air.

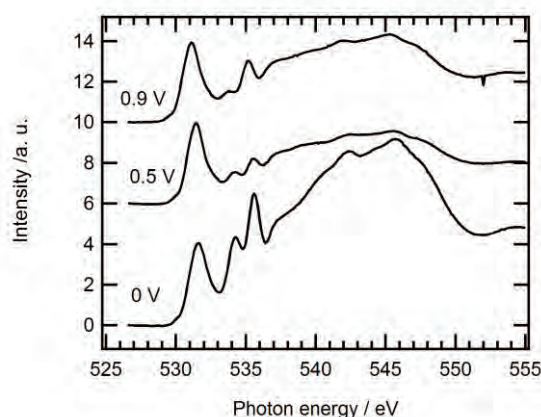


Fig. 1. O K-edge spectra of  $\text{Ba}_3\text{Mn}_2\text{O}_8$  treated by anodic polarization in neutral solution at various potentials.

- [1] J. H. Alstrum-Acevedo *et al.*, *Inorg. Chem.* **44** (2005) 6802.
- [2] G. C. Dismukes, R. Brimblecombe, G. A. N. Felton, R. S. Pryadun, J. E. Sheats, L. Spiccia and G. F. Swiegers, *Acc. Chem. Res.* **42** (2009) 1935.
- [3] F. Jiao and H. Frei, *Energy Environ. Sci.* **3** (2010) 1018.
- [4] J. Suntivich *et al.*, *J. Phys. Chem. C* **118** (2014) 1856.
- [5] F. A. Armstrong, *Phil. Trans. R. Soc. B* **363** (2007) 1263.

BL4B

## XANES Analysis of Valence State of Co Doped in CeO<sub>2</sub>

T. Oomori<sup>1</sup>, K. Tarui<sup>1</sup> and T. Yamamoto<sup>1,2</sup>

<sup>1</sup>Faculty of Science and Engineering, Waseda University, Tokyo 169-8555, Japan

<sup>2</sup>Institute of Condensed-Matter Science, Waseda University, Tokyo 169-8555, Japan

A lot of researches on dilute magnetic materials (DMMs), which are processed by doping dilute (a few at%) magnetic elements into the non-magnetic materials, have been carried out after the discovery of the ferromagnetism in InAs:Mn [1]. Among DMMs, there are two type of the models for the doped magnetic ions, i.e., substituted and precipitated ones. In order to understand the mechanism of the appearance of ferromagnetism in DMMs, it is essential to know the local environment of the doped magnetic elements. We have successfully studied the valence state of Mn and Fe ions by measuring the Mn and Fe-L<sub>3</sub> X-ray absorption near edge structure (XANES) analysis at BL4B in UVSOR [2]. In the present study, charge state of doped Co in Co-doped CeO<sub>2</sub>, which shows room-temperature ferromagnetism, was investigated by the XANES analysis at Co-L<sub>3</sub> edge.

Co doped CeO<sub>2</sub> was prepared by the conventional solid-state reaction method. Reagent grade CeO<sub>2</sub> and Co<sub>3</sub>O<sub>4</sub> powders were used as starting materials. These powders were firstly weighed with a molar ratio of Ce:Co = 0.95:0.05, which are mixed and ground in an agate mortar and fired in air at 1273 K for 10 hours. After cooling down to the room temperature, these specimen was annealed in Ar(97%)-H<sub>2</sub>(3%) atmosphere at 723 K for an hour. Co-L<sub>3</sub> XANES spectra of Co-doped CeO<sub>2</sub>, Co-foil and Co<sub>3</sub>O<sub>4</sub> were measured at BL4B in UVSOR by total electron yield method. The incident beam was monochromatized with a varied-line-spacing plane grating (800 lines/mm). Energy resolution (E/ΔE) of the incident beam was set to 3000. Sample powders and foil were put on the carbon adhesive tape, which are attached on the first Cu-Be diode of the electron multiplier.

Prior to the XANES analysis, synthesized specimen was examined by the X-ray diffraction. No extra peaks appeared after doping the Co and peak position did not change. If Co is substituted at Ce site, peak position should change, because ionic radius of Co is much smaller than that of Ce ion. This result suggests Co exists as nano-sized precipitates.

Observed Co-L<sub>3</sub> XANES spectra of Co<sub>3</sub>O<sub>4</sub>, Co-foil and Co-doped CeO<sub>2</sub> are shown in Fig. 1. Fine structures of the reference samples, i.e., Co and Co<sub>3</sub>O<sub>4</sub>, show different profiles and we can clearly distinguish these two. A profile of Co-L<sub>3</sub> XANES of Co-doped CeO<sub>2</sub> show similar profile as Co-foil, which suggests that doped Co exists as metallic charge state. Combining the results by XRD and XANES, we can conclude that doped Co exists as nano-sized metallic precipitate.

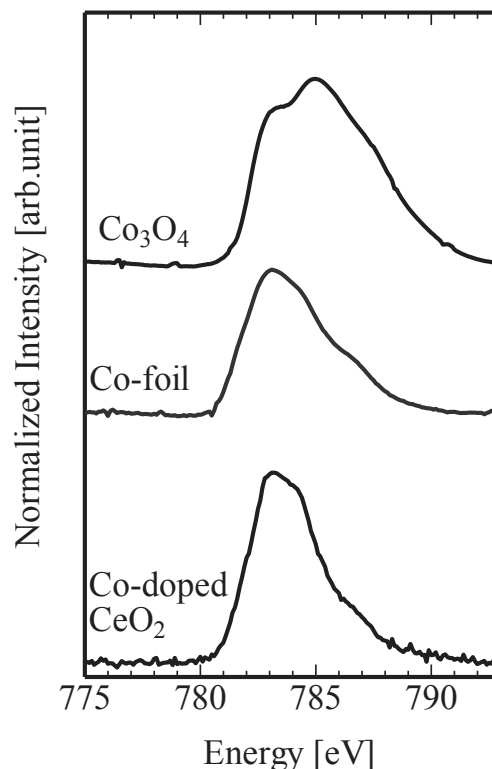


Fig. 1. Co-L<sub>3</sub> XANES spectra of Co<sub>3</sub>O<sub>4</sub>, Co-foil and Co-doped CeO<sub>2</sub>.

[1] H. Ohno *et al.*, Phys. Rev. Lett. **68** (1992) 2664.

[2] T. Okazaki *et al.*, Solid State Comm. **151** (2011) 1749.

BL4B

## Investigation on the Surface Structure of $\text{LiNbO}_3$ -Coated $\text{LiCoO}_2$ Using the Soft X-Ray XANES Measurement

H. Kobayashi, T. Okumura and M. Shikano

Research Institute for Ubiquitous Energy Devices, National Institute of Advanced Industrial Science and Technology (AIST), Ikeda, 563-8577, Japan

Realization of the all-solid-state Li-ion battery (LIB) consisting of non-flammable inorganic solid electrolytes is desired because of their high safety. To improve energy and power densities of the all-solid-state LIB, the decrease of the interfacial resistance between the electrode and solid electrolyte is required as well as the synthesis of solid electrolyte with high Li-ion conductivity. It has been reported that  $\text{Li}_4\text{Ti}_5\text{O}_{12}$ -coated  $\text{LiCoO}_2$  reduced the interfacial resistance between  $\text{LiCoO}_2$  positive electrode and sulfide electrolyte and enhanced the rate capability to be compatible to that of commercial LIB with liquid electrolyte [1]. Recently we also reported that the mechanochemical  $\text{Al}_2\text{O}_3$ -coating process was an effective way of improving the cycle performance at high temperature in the cell of  $\text{Li}/1\text{M LiPF}_6$  in  $\text{EC}:\text{DMC}$  (1:2)/ $\text{Li}_{1.20}\text{Mn}_{0.55}\text{Ni}_{0.16}\text{Co}_{0.09}\text{O}_2$  [2]. In this paper,  $\text{LiNbO}_3$ -coating  $\text{LiCoO}_2$  was prepared and these surface structure were investigated using the soft X-ray XANES measurement.

$\text{LiNbO}_3$ -coated  $\text{LiCoO}_2$  were prepared with an ethanol solution of ethoxides of Li and Nb using tumbling fluidized bed granulating-coating machines (POWREX Co.) and heated for 30 min. in air between 573 and 773 K. The particle morphology and containing transition metal were confirmed by SEM and EDAX measurements. Electronic structures were investigated by XANES measurement at the beamline BL4B in UVSOR.

The SEM and EDAX results clarified that the sizes of pristine  $\text{LiCoO}_2$  particles were in the range of 1-10  $\mu\text{m}$  (an average particle size: 6  $\mu\text{m}$ ) and no transition metal except Co was observed. The EDAX results showed the existence of Nb in the  $\text{LiNbO}_3$ -coated  $\text{LiCoO}_2$  particles, but gave no information of the distribution of Nb on the surface of  $\text{LiNbO}_3$ -coated  $\text{LiCoO}_2$  particle. Therefore, the soft X-ray XANES was measured to check the surface structure on  $\text{LiCoO}_2$ . The Co *L*-edge XANES spectra clarified that the samples after heat treatment showed weaker intensities of the A and B peaks compared with the pristine sample as shown in Fig. 1. The O *K*-edge XANES spectra clarified that the shape of the C and D peaks for the samples after heat treatment was close to that of  $\text{LiNbO}_3$  with increasing heat temperature as shown in Fig. 2. These results indicated that the surface of  $\text{LiNbO}_3$ -coated  $\text{LiCoO}_2$  after heat treatment at 773 K was covered uniformly by  $\text{LiNbO}_3$  layer and that the soft X-ray XANES measurement was an effective way of confirming the

surface structure of coated samples.

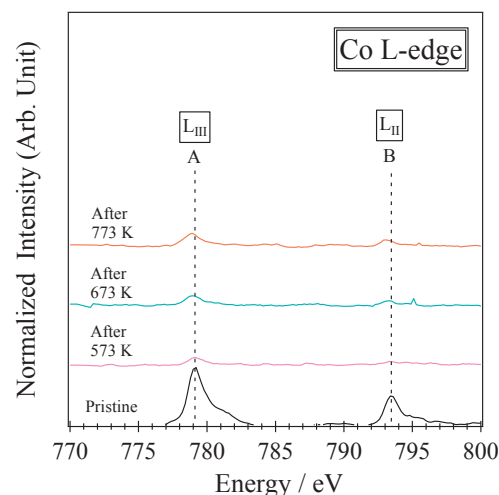


Fig. 1. Co *L*-edge XANES spectra for pristine and  $\text{LiNbO}_3$ -coated samples after heat treatment.

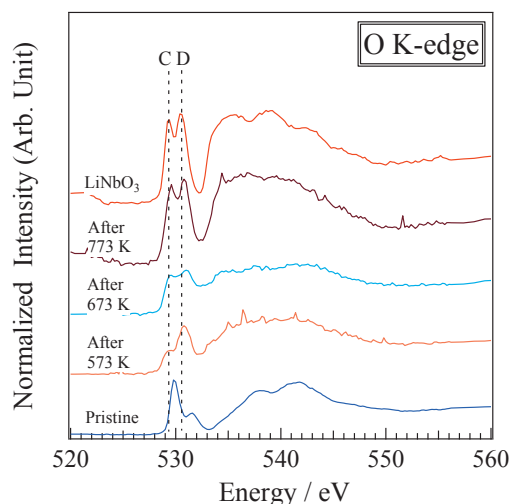


Fig. 2. O *K*-edge XANES spectra for pristine and  $\text{LiNbO}_3$ -coated samples after heat treatment together with  $\text{LiNbO}_3$ .

[1] N. Ohta *et al.*, *Adv. Mater.* **18** (2006) 2226.

[2] H. Kobayashi *et al.*, *Solid State Ionics* **262** (2014) 43.

BL4B

## Perpendicular Magnetic Anisotropy in Mn<sub>4</sub>N Studied by X-Ray Magnetic Circular Dichroism

G. Shibata<sup>1</sup>, J. Okabayashi<sup>2</sup>, A. Chikamatsu<sup>3</sup>, A. Fujimori<sup>1</sup> and T. Hasegawa<sup>3</sup>

<sup>1</sup>Department of Physics, The University of Tokyo, Tokyo 113-0033, Japan

<sup>2</sup>Research Center for Spectrochemistry, The University of Tokyo, Tokyo 113-0033, Japan

<sup>3</sup>Department of Chemistry, The University of Tokyo, Tokyo 113-0033, Japan

Transition-metal nitrides such as Co<sub>4</sub>N, Fe<sub>4</sub>N, and Mn<sub>4</sub>N have been investigated as novel materials for applications in spintronic devices because of the room-temperature ferro- or ferrimagnetism. Especially, the perpendicular magnetic anisotropy (PMA) in metallic Mn<sub>4</sub>N is one of the interesting topics since it has benefits of enhanced thermal stability and low current magnetization switching. Anti-perovskite type Mn<sub>4</sub>N consists of two kinds of inequivalent Mn sites (Mn<sub>A</sub>: 3.85  $\mu_B$ /f.u. and Mn<sub>B</sub>: -0.9  $\mu_B$ /f.u.) which occupy the corner and face-centered positions of the unit cell with tetragonal distortion. The large PMA energy of 0.16 MJ/m<sup>3</sup> in Mn<sub>4</sub>N was reported at room temperature [1]. However, the origin for the appearance of PMA in Mn<sub>4</sub>N has not been clarified yet. For fundamental understanding of PMA in Mn<sub>4</sub>N, the electronic and magnetic structures have to be clarified explicitly. In order to investigate PMA energy, it is necessary to evaluate the orbital magnetic moments along parallel and perpendicular directions to the surface. Here, we report the x-ray magnetic circular dichroism (XMCD) of Mn<sub>4</sub>N in order to discuss the origin of PMA.

Samples were grown by pulsed laser deposition method on MgO (001) substrates. The 40-nm-thick Mn<sub>4</sub>N was deposited under the substrate temperature of 500 °C. Although there is a lattice mismatch of 7.0 % at the interface, coherent growth was observed by transmission electron microscope [1]. It is reported that the 4-nm-thick MnO<sub>x</sub> layer is formed on the Mn<sub>4</sub>N surface [1]. In order to suppress the formation of such an oxidization layer, the sample surface was capped with 2-nm-thick Al<sub>2</sub>O<sub>3</sub>. The saturation magnetic field of the Mn<sub>4</sub>N thin film along the magnetically hard axis was estimated to be  $\sim 3$  T [1]. XMCD measurements were done at UVSOR BL-4B under the conditions of 5 K [2]. A magnetic field of  $\pm 5$  T using a superconducting magnet was applied along the incident polarized soft x-ray, which is enough to saturate the magnetization along the magnetically hard axis direction. The total electron yield mode was adopted. Normal incidence (NI) and grazing incidence (GI) geometries were employed to deduce the anisotropic orbital magnetic moments.

Figures 1(a) and 1(b) show Mn *L*-edge x-ray absorption spectra (XAS) and XMCD in the NI and GI setups, respectively. In XAS, a shoulder structure is observed at 632 eV. In the Mn *L*<sub>3</sub> XMCD spectra, in addition to the negative XMCD peak

located at the main absorption peak (628.5 eV), a positive XMCD signal is observed around 630 eV. In Mn<sub>4</sub>N, two kinds of XMCD components originating from the Mn<sub>A</sub> and Mn<sub>B</sub> sites are overlapped antiferromagnetically, which brings the complicated XMCD spectral line shapes. Since the decomposition into each component has not succeeded yet, magneto-optical sum rules cannot be applied at this moment. The asymmetry in XMCD between the *L*<sub>3</sub> and *L*<sub>2</sub> peaks at the NI setup is larger than that in the GI setup, suggesting that the anisotropic orbital magnetic moments are induced. These results suggest that the anisotropic orbital magnetic moments might be related to the PMA in this system as explained by Bruno's relationship [3]. In order to deduce the site specific spin and orbital magnetic moments, we are planning to measure the substitution dependence of XMCD spectral line shapes in (Mn<sub>1-x</sub>M<sub>x</sub>)<sub>4</sub>N (*M* = nonmagnetic metal), which will provide information about the electronic states and magnetism of each Mn site.

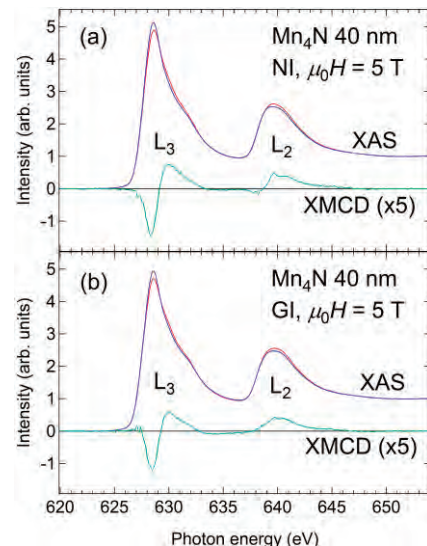


Fig. 1. X-ray absorption spectra (XAS) and XMCD of Mn<sub>4</sub>N thin film at the Mn *L* edge in (a) normal incidence (NI) and (b) grazing incidence (GI) setups at 5 K and 5 T.

[1] X. Shen, A. Chikamatsu, K. Shigematsu, Y. Hirose, T. Fukumura and T. Hasegawa, *Appl. Phys. Lett.* **105** (2014) 072410.

[2] T. Yokoyama, Y. Takagi and K. Nakagawa, *Int. Rev. Phys. Chem.* **27** (2008) 449.

[3] P. Bruno, *Phys. Rev. B* **39** (1989) 865.

BL4B

## Investigating Orbital Magnetic Moments in Spinel-Type $\text{MnV}_2\text{O}_4$ Using X-Ray Magnetic Circular Dichroism

J. Okabayashi<sup>1\*</sup>, S. Miyasaka<sup>2</sup>, K. Henmi<sup>2</sup>, K. Tanaka<sup>2,3</sup>, S. Tajima<sup>2</sup>,  
H. Wadati<sup>4</sup>, A. Tanaka<sup>5</sup>, Y. Takagi<sup>3</sup> and T. Yokoyama<sup>3</sup>

<sup>1</sup>Research Center for Spectrochemistry, University of Tokyo, Tokyo 113-0033, Japan

<sup>2</sup>Department of Physics, Osaka University, Toyonaka 560-0043, Japan

<sup>3</sup>Institute of Molecular Science, Okazaki, 444-8585, Japan

<sup>4</sup>Institute for Solid State Physics, University of Tokyo, Kashiwa, 227-8581, Japan

<sup>5</sup>Department of Quantum Matter, Hirshima University, Higashi-Hiroshima 739-8530, Japan

Couplings between orbital and spin degrees of freedom in transition metal (TM) oxides exhibit a wide variety of interesting physical phenomena studied in strongly correlated electron systems. The orbital degeneracy of  $t_{2g}$  or  $e_g$  orbitals, split by the crystal field in TM oxides, gives rise to the orbital ordering phenomena in perovskite-type Mn or V oxides accompanied by Jahn-Teller distortion. Spinel-type  $\text{MnV}_2\text{O}_4$  is a good candidate to study orbital ordering since orbital magnetic moments of  $\text{Mn}^{2+}$  ( $d^5$ ) are nearly quenched with relatively large spin moments in high spin states. An unresolved issue related to orbital ordering of spinel-type vanadium oxides is the relationship between the orbital magnetic moments in vanadium sites and orbital ordering. In this study, we investigated the element specific electronic and magnetic properties of  $\text{MnV}_2\text{O}_4$  using XAS and XMCD, and examined the relationship between orbital magnetic moments and orbital ordering.

Single crystals were grown by the floating-zone method. Details of the sample preparation and the fundamental physical properties are described in Ref. [1]. The magnetic and orbital ordering temperatures of  $\text{MnV}_2\text{O}_4$  were estimated to be 59 and 54 K, respectively. The XAS and XMCD measurements were performed at BL-4B, UVSOR, Institute of Molecular Science. Total photoelectron yield mode by directly detecting the sample current was adopted. A magnetic field of  $\pm 5$  T was applied along the direction of the incident polarized soft x-ray.

Figure 1(a) shows XAS, XMCD, and the integrated XMCD spectra of V  $L_{2,3}$ -edge regions taken at 5 K, which is sufficiently lower than the orbital ordered transition temperature. The resulting residuals from the XMCD integrals for both  $L_2$  and  $L_3$  edges are shown at the bottom of Fig. 1 (a), suggesting that the finite values of orbital magnetic moments remained in the  $\text{V}^{3+}$  states. Using the integrals over XAS spectra and assuming that the V  $3d$  electron number to be 2, we deduced the orbital magnetic moments ( $m_l$ ) to be less than  $0.01 \mu_B/(\text{V atoms})$  from the orbital sum rule. This value is close to zero but finite. This result indicates that unquenched orbital magnetic moments contribute to complex wave functions in V sites.

Figure 1(b) shows the calculated XAS and XMCD spectra of V  $L$ -edges obtained using the cluster

models with configuration interaction. In the case of V  $L$ -edges, qualitatively similar spectral line shapes with both XAS and XMCD spectra in Fig. 1(a) were reproduced by the cluster-model calculation. Tetragonal local lattice distortion around the V sites must also be considered. The  $t_{2g}$  states are split into two levels by the tetragonal distortion and the lowest  $xy$  states are occupied by one of the electrons. The other electron occupies the  $yz$  or  $zx$  states. We determined the tetragonal distortion value for the V  $3d$  states ( $D_{\text{tet}}$ ) to be 0.02 eV in order to reproduce the complicated XMCD spectral line shapes qualitatively. The existence of the small but finite orbital magnetic moments in the V sites can be explained by the (i) complex orbital ordering as discussed in the case of  $\text{FeV}_2\text{O}_4$ , (ii) domain formation, and (iii) mixing of the real and complex orbital orderings due to the trigonal distortion around the V sites [2].

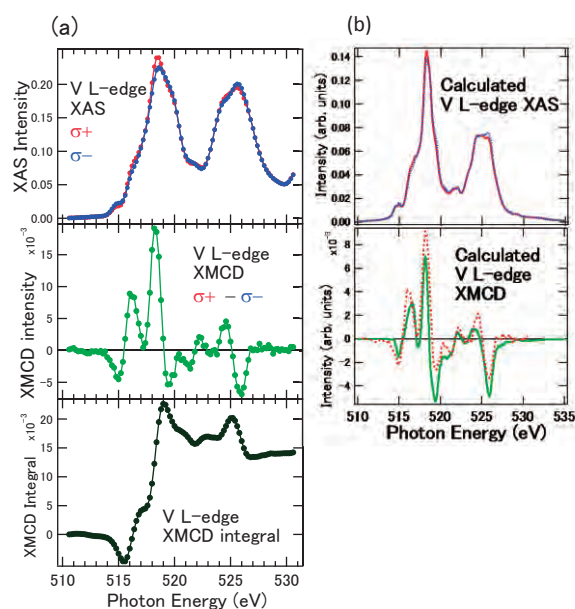


Fig. 1. V  $L$ -edge XAS, XMCD, and XMCD integrated spectra in  $\text{MnV}_2\text{O}_4$  (a). Cluster model calculations are also shown in (b).

[1] K. Henmi *et al.*, J. Phys. Soc. Jpn. **81** (2012) SB030.

[2] J. Okabayashi *et al.*, submitted.

\*e-mail: jun@chem.s.u-tokyo.ac.jp

BL5B

## Study of Ultrafast Spin-Switching of a Ferrimagnetic Alloy by Resonant Magneto-Optical Kerr Effect

S. Yamamoto<sup>1</sup>, M. Taguchi<sup>2</sup>, Y. Kubota<sup>1</sup>, S. Ito<sup>1</sup>, M. Hasumoto<sup>3</sup>,  
E. Shigemasa<sup>3</sup> and I. Matsuda<sup>1</sup>

<sup>1</sup>Institute for Solid State Physics, The University of Tokyo, Chiba 277-8581, Japan

<sup>2</sup>Nara Institute of Science and Technology (NAIST), Ikoma 630-0192, Japan

<sup>3</sup>UVSOR Facility, Institute for Molecular Science, Okazaki 444-8585, Japan

A crystal of GdFeCo is a ferrimagnetic metallic alloy, composed of rare-earth and transition metal sublattices that couple anti-ferromagnetically. It has been reported that the material shows ultrafast spin-switching by irradiation of a femtoseconds-pulse of either circularly or linearly polarized infrared light. Recently, we have carried out time-resolved measurement of resonant magneto-optical Kerr effect (RMOKE) [1] at the Fe *M*-shell absorption edge by soft x-ray free electron laser and succeeded in directly detecting dynamic variations of magnetic signal during the spin-switching. However, the RMOKE data have lacked spectroscopic information to make a proper interpretation of the phenomena.

In the present research, we carried out the RMOKE experiment at BL-5B at UVSOR to measure spectra of absorption intensity and Kerr rotation angle of a crystal of GdFeCo. Kerr rotation angle was determined by the rotating-analyzer ellipsometry method (Fig. 1). Figure 2(a) shows a schematic drawing of the sample system. A 20 nm-thick Gd<sub>21</sub>(Fe<sub>90</sub>Co<sub>10</sub>)<sub>79</sub> film was grown on a Ta/Si(SiO<sub>2</sub>) substrate and capped with a 2 nm-thick Ta layer.

Figure 2(b) shows absorption spectrum of the GdFeCo sample that shows peaks of various core-levels of Ta, Fe, and Co atoms. In the measurements, perpendicular magnetic field of +/- 0.5 T was applied with a permanent magnet. As shown in the figure, the simulated Fe 3*p* spectra, based on the resonant scattering theory [1], almost completely reproduces spectral feature of the Fe 3*p* absorption peak. The Kerr rotation angles ( $\theta_k$ 's) of the Fe *M*-shell absorption edge were evaluated as in Fig. 2(c). The  $\theta_k$  value becomes as large as 3-4 degrees at the photon energy (*hν*) around 50 eV and it is reasonably reproduced by the simulation [1]. The discrepancy at *hν* > 60 eV is likely due to the contribution from the Co 3*p* level that has not been considered in the calculation. On the other hand, the difference at the pre-edge in Fig.2(c) seemingly originates from the film structure that has been reported previously in the Ni nanofilm [1]. The smaller  $\theta_k$  value of the Fe *M*-edge, compared with the Ni *M*-edge, was likely due to the smaller spin-orbit interaction for the lighter element.

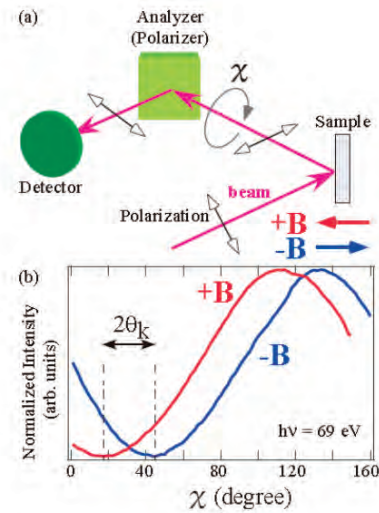


Fig.1. (a) Geometry for rotating-analyzer ellipsometry (RAE) to measure the polar MOKE. The light beam is *p*-polarized by the surface, and the magnetic field (**B**) is applied along the surface normal. (b) Typical results of the intensity variation with rotation angle,  $\chi$ . The Kerr rotation angle,  $\theta_k$ , can be determined from  $2\theta_k = |\theta(+B) - \theta(-B)|$ .

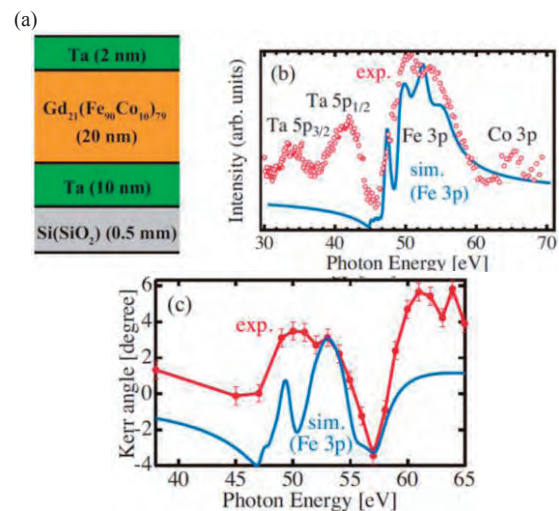


Fig.2. (a) Schematic drawing of the GdFeCo sample system. (b) The absorption spectrum at *hν*=30-70 eV. (c) Photon energy dependence of the Kerr-rotation angle ( $\theta_k$ ).

[1] Sh. Yamamoto *et. al.*, Phys. Rev. B. **89** (2014) 064423.

BL6B

## Infrared Spectroscopy of Photo-Induced Defects in Ce<sup>3+</sup>:GAGG Crystals

R. Inaba<sup>1</sup>, M. Kitaura<sup>1</sup>, K. Kamada<sup>2</sup>, S. Kurosawa<sup>2,3</sup>, A. Ohnishi<sup>1</sup> and K. Hara<sup>4</sup>

<sup>1</sup>Department of Physics, Faculty of Science, Yamagata University, Yamagata 990-8560, Japan

<sup>2</sup>New Industry Creation Hatchery Center, Tohoku University, Sendai 980-8579, Japan

<sup>3</sup>Institute for Materials Research, Tohoku University, Sendai 980-8577, Japan

<sup>4</sup>Research Institute of Electronics, Shizuoka University, Hamamatsu 422-8529, Japan

The Ce-doped Gd<sub>3</sub>Al<sub>2</sub>Ga<sub>3</sub>O<sub>12</sub> (Ce:GAGG) crystal was developed as a scintillator for radiation detector. These crystals exhibit a high light yield, high-energy resolution, and short decay time, as compared to other inorganic scintillator crystals [1]. On the other hand, it has been pointed out that trapping of photo-excited carriers due to crystal defects causes the occurrence of phosphorescence and decrease in light yield [2,3]. In order to improve the performance of scintillators, it is necessary to clarify the origin of crystal defects. We have measured infrared (IR) absorption spectra of Ce:GAGG crystals under UV-irradiation.

Ce:GAGG crystals were grown from a melt in oxygen or hydrogen atmosphere by the CZ method. The concentration of cerium ion was set to 1.0 mol%. Experiment was performed at the beamline BL6B. The UV-irradiation was performed at 3.31 eV with a picosecond light pulser, which is located in the Ce<sup>3+</sup> 4*f* → 5*d*<sub>2</sub> absorption band. The sample temperature was set to 9K.

Figure 1 shows stationary IR absorption spectra of oxygen- and hydrogen-annealed Ce:GAGG crystals. As indicated by a blue line, the IR absorption spectrum of oxygen-annealed Ce:GAGG crystal is structureless. On the other hand, one can see a broad band above 6000 cm<sup>-1</sup> in the IR absorption spectrum drawn with a black line.

Figure 2 shows IR absorption spectra of an oxygen-annealed Ce:GAGG crystal. A black line represents the IR absorption spectrum without UV-irradiation. When UV-irradiation is turned on, the IR spectrum exhibits a broad band above 6000 cm<sup>-1</sup>, as indicated by a blue line. This band is the same as the stationary IR absorption band for a hydrogen-annealed Ce:GAGG crystal, which was shown in Fig. 1.

The UV-irradiation at 3.31 eV results in the creation of excited electrons in the conduction band and Ce<sup>4+</sup> ions [2-4]. The excited electrons will be captured immediately by lattice imperfections [2]. Therefore, it is likely that the photo-induced IR absorption band in Fig. 1 is caused by the formation of trapped electrons.

There are few candidates for the origin of trapped electrons in multicomponent oxides with garnet structure. The present experiment demonstrates that the photo-induced IR absorption band for an oxygen-annealed Ce:GAGG crystal is the same as the stationary IR absorption band for a hydrogen-annealed Ce:GAGG crystal. In general, it

has been accepted that oxygen vacancies are easily introduced in hydrogen-annealed oxide crystals. On this basis, we assign the photo-induced IR absorption band to electrons trapped at oxygen vacancies. This finding is valuable as a guiding principle to grow high-quality scintillator crystals.

A part of this work was carried out under the Cooperative Research Project Program of the Research Institute of Electrons, Shizuoka University.

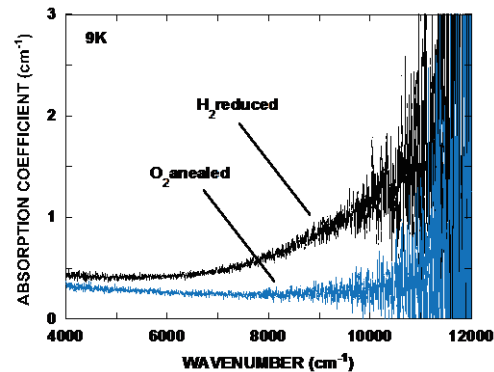


Fig. 1. Stationary IR absorption spectrum of oxygen- and hydrogen-annealed Ce:GAGG crystals measured at 9K.

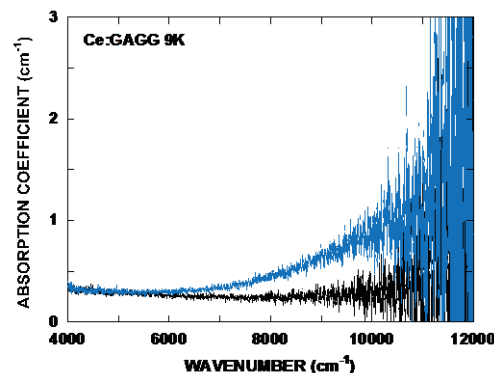


Fig. 2. IR absorption spectrum of an oxygen annealed Ce:GAGG crystal measured at 9K under UV-irradiation (blue line). The data obtained under unirradiation was also shown (black line).

- [1] K. Kamada *et al.*, *J. Cryst. Growth* **352** (2012) 88.
- [2] M. Kitaura *et al.*, *J. Appl. Phys.* **115** (2014) 083517.
- [3] A. Satoh, *et al.*, *Jpn. J. Appl. Phys.* **53** (2014) 05FK01.
- [4] P. Dorenbos, *J. Lumi.* **134** (2014) 310.

BL6B

## Formation Mechanism of Ultrashallow Thermal Donors Formed in Carbon- and Hydrogen-Doped Czochralski Silicon Crystals

A. Hara and T. Awano

Department of Electronic Engineering, Tohoku Gakuin University, Tagajo 985-8537, Japan

We previously reported on ultrashallow thermal donors (USTDs) in carbon- and hydrogen-doped Czochralski silicon (CZ Si) crystals [1]. The following formation mechanism was tentatively proposed: in the first stage, STD(H)s are formed at a high rate; in the second stage, carbon diffuses in a thermally activated process via an interstitial or interstitialcy mechanism and modulates the electronic structure of STD(H)s by combining with them to form USTDs. In this study, we evaluated the formation process of USTDs in order to clarify the previously proposed model.

Figure 1 shows the behavior of USTDs and STD(H)s after carbon- and hydrogen-doped CZ Si crystals were annealed at 480 °C for various durations of time [1]. USTDs were slowly generated, and their spectral intensity increased with the annealing time up to 40 h. However, some lines for the group-1 USTDs began to reduce their intensity after further annealing, and a strong line eventually became dominant. In contrast, one strong line was dominant in the group-2 USTDs. The STD(H) line intensities were strong even after short-term annealing for 3 h and were maximized after annealing for 10 h. This indicates that the formation speed of STD(H)s is very high compared to that of USTDs. It is significant that the STD(H) lines began to decrease in intensity when the annealing continued beyond 10 h.

To investigate the generation of USTDs and reduction of STD(H)s at 480 °C for various annealing times, as shown in Fig. 1, we used Lorentzian curve fitting to examine the variation in area intensity of each line. For the group-1 USTDs, an area intensity of  $1s-2p_{\pm}$  lines was used. For the group-2 USTDs,  $1s-2p_0$  lines were used for curve fitting because of the following reasons. The  $1s-3p_{\pm}$  spectral lines of the group-1 USTDs and  $1s-2p_0$  lines of the STD(H)s overlapped with the  $1s-2p_{\pm}$  lines of the group-2 USTDs. According to the effective mass theory, the ratio of intensity between the  $1s-2p_0$  and  $1s-2p_{\pm}$  lines should be 4:10. Thus, we determined the area intensity of the  $1s-2p_{\pm}$  lines of group-2 to be 2.5 times the area intensity of the  $1s-2p_0$  spectral lines derived from curve fitting. The curves of the  $1s-2p_{\pm}$  STD(H) lines were fitted by using two main peaks and five satellite lines.

Figure 2 summarizes the variation in area intensity of the  $1s-2p_{\pm}$  lines for the group-1 and group-2 USTDs and the STD(H)s; the figure also shows the sum of these donors as a function of the annealing time at 480 °C. The summation of the USTD and

STD(H) line areas showed a weak dependency on the annealing time when the duration was longer than 10 h at 480 °C. This result supports our model, which shows that STD(H)s are changed to USTDs.

In summary, we validated our model for the formation mechanism of USTDs based on the variations in the area intensities of USTDs and STD(H)s using curve fitting. In the first stage, STD(H)s form at a high rate; in the second stage, carbon modulates the electronic structure of STD(H)s by combining with them to form USTDs.

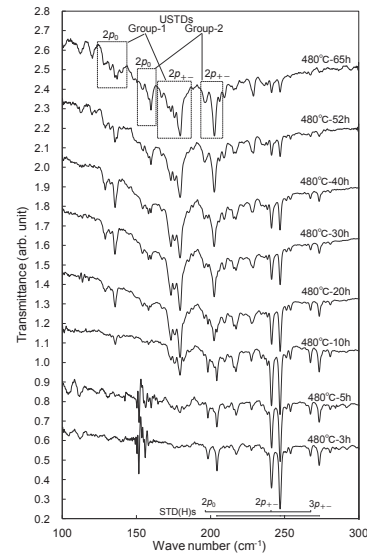


Fig. 1. Variation in USTD and STD(H) spectra in carbon- and hydrogen-doped CZ Si as function of annealing duration at 480 °C.

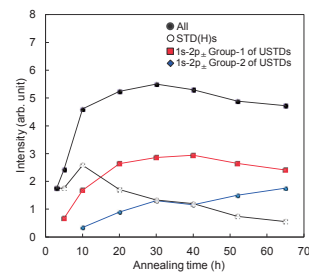


Fig. 2. Variation in spectral intensity area for STD(H)s, group-1 and group-2 USTDs, and the sum of these as function of annealing duration at 480 °C.

[1] A. Hara and T. Awano: UVSOR ACTIVITY REPORT 2013 **41** (2014) 88.

BL6B

## Domain Structure of Alkali Niobate Piezoelectrics by Far-Infrared Reflective Method

Y. Taniguchi, T. Yamazaki, M. Kato and K. Kakimoto

Graduate School of Engineering, Nagoya Institute of Technology, Nagoya 466-8555, Japan

Orthorhombic (Na,K)NbO<sub>3</sub>(NKN) piezoelectrics have attracted much attention as substitute materials for Pb(Zr,Ti)O<sub>3</sub>. We have examined that Li-doped NKN revealed the existence of a monoclinic *Pm* phase, and concluded that the *Pm* phase is the main factor of good piezoelectric properties[1][2]. However, there is no detailed report about the domain structure of NKN, which could explain the origins of the improved properties. Electrical measurements, like the impedance measurement, allow only for the evaluation of grains and grain boundaries. However, it is impossible to evaluate domains and domain walls. Therefore, spectroscopic methods need to be used, because they provide the structural deformation of the perovskite structure at a local scale about NbO<sub>6</sub> octahedron and alkali-ion movements. Via Raman spectroscopy, large changes in the vicinity of domain walls have been obtained, both in the Raman shift and its peak intensity. In this work, we evaluated the domain wall from the change of the permittivity using Infrared(IR) reflectivity measurements.

(Na<sub>0.55</sub>K<sub>0.45</sub>)(Nb<sub>0.995</sub>Mn<sub>0.005</sub>)O<sub>3</sub> crystals were prepared by the floating zone method. The obtained crystals were orthorhombic and had stripe domains with a width of ~ 50 μm. The samples were cut and polished for IR measurements. By means of a FT-IR spectrometer (Bruker, VERTEX 70v), IR measurements were performed every 10 μm vertically to the domain structure by using a line mapping technique. The spectra were fitted by the following equation:

$$\varepsilon(\omega) = \varepsilon_{\infty} + \sum_n \frac{\omega_{pn}^2}{\omega_{on}^2 - \omega^2 - i\gamma_n\omega} \quad (1)$$

where,  $\varepsilon_{\infty}$  is the high-frequency dielectric constant,  $\omega_p$  and  $\omega_o$  the plasma and longitudinal frequencies, and  $\gamma$  the damping constant. The complex dielectric function is related to the reflectivity spectrum by the equation

$$R = |\sqrt{\varepsilon(\omega)} - 1| / |\sqrt{\varepsilon(\omega)} + 1|^2 \quad (2)$$

Figure 1 shows the IR reflectivity spectra of Mn-NKN crystals at R.T. using two apertures of different diameter. The spectra in the case of the aperture with a diameter of 0.5 mm showed no change. In comparison, when the diameter is 0.25 mm, the spectra slightly changed with the position of the measurement. This result shows that the structure evaluation of domains and domain walls is enabled by using the aperture with the smaller diameter.

Figure 2 shows the permittivity of Mn-NKN crystals at different positions. With the diameter of 0.25 mm, the permittivity  $\varepsilon'$  showed a maximum value at the 0 μm position. The main reason for this behavior could be the multitude of the polar axis at the domain wall. This result suggests that the domain wall could be evaluated via the increase of the permittivity during IR reflectivity measurement.

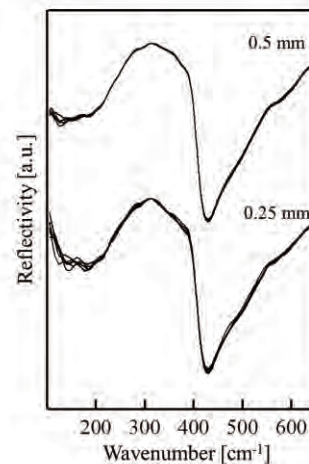


Fig. 1. IR reflectivity spectra of Mn-NKN crystals at R.T. using the aperture diameters of 0.5 mm and 0.25 mm

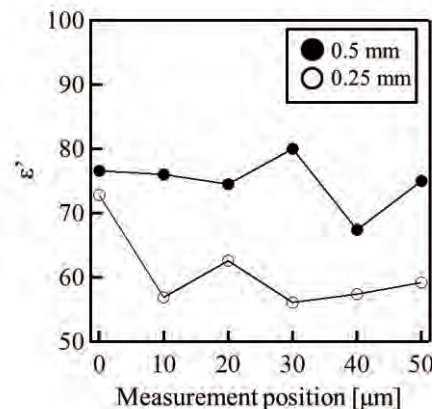


Fig. 2. Permittivity of Mn-NKN crystals at R.T. at different positions for the aperture diameters of 0.5 mm and 0.25 mm

[1] T. Nishi, K. Tsuchida, K. Kato, N. Kato, M. Watanabe and K. Kakimoto, UVSOR Activity Report 2012 **40** (2013) 140.

[2] T. Yamazaki, M. Kato, K. Tsuchida and K. Kakimoto, UVSOR Activity Report 2013 **41** (2014) 87.

BL6B

## Spatial Distribution of Carrier Density of $\text{Sm}_{1-x}\text{Y}_x\text{S}$ ( $x = 0.17$ )

 S. Kamei<sup>1</sup>, H. Takao<sup>1</sup>, Y. Ohtsubo<sup>2,1</sup>, H. Miyazaki<sup>3</sup>, K. Imura<sup>4</sup>, N. K. Sato<sup>4</sup> and S. Kimura<sup>2,1</sup>
<sup>1</sup> Department of Physics, Osaka University, Toyonaka 560-0043, Japan

<sup>2</sup> Graduate School of Frontier Biosciences, Osaka University, Suita 565-0871, Japan

<sup>3</sup> Department of Frontier Materials, Nagoya Institute of Technology, Nagoya 466-8555, Japan

<sup>4</sup> Department of Physics, Nagoya University, Nagoya 464-8603, Japan

Physical properties of some materials are drastically changed at the first-order phase transition by tuning external parameters of temperature, pressure, magnetic field, and chemical pressure. At the first-order transition, phase separations as well as phase coexistence are sometimes observed [1]. Since the phase separation is strongly related to the origin of the first-order transition, the origin of the phase separations is under debate in some materials.

Samarium monosulfide  $\text{SmS}$  is known to be a material with a pressure-induced first-order insulator-to-metal transition accompanied with the color change from black to golden-yellow, namely black-golden phase transition (BG transition), at the critical pressure of about 0.7 GPa [2]. The origin of the BG transition is known as the valence transition from  $\text{Sm}^{2+}$  with larger ionic radius to  $\text{Sm}^{3+}$  with smaller radius owing to the external pressure. When a part of  $\text{Sm}^{2+}$ -ions are replaced to  $\text{Y}^{3+}$ -ions of smaller ionic radius, namely  $\text{Sm}_{1-x}\text{Y}_x\text{S}$ , a similar BG transition is realized at ambient pressure [3]. At the border of the BG transition of  $x \sim 0.17$ , the black and golden phase separation (BG separation) is observed [4]. To investigate the origin of the BG separation, we measured a micro X-ray fluorescence (XRF) imaging (10- $\mu\text{m}$  step) of Y  $K\alpha$  line to check the spatial distribution of Y-atoms. In addition, to clarify the relation of the insulator-to-metal transition to the BG transition, the carrier density distribution was also measured by using an IR micro-imaging (6.25- $\mu\text{m}$  step, about 26,000 points in total) [5]. The obtained reflectivity spectra at all measured points were fitted by the combination of the Drude and Lorentz functions using a nonlinear least-square method and the spatial distribution of the effective carrier density

( $N_{\text{eff}}$ ) in the Drude function was mapped on the sample surface.

Figure 1a shows the visible image of the BG separation of  $\text{Sm}_{0.83}\text{Y}_{0.17}\text{S}$ . Some golden-yellow areas, which indicate the appearance of the golden phase, are observed. The spatial distribution of the Y-ion probed by the XRF imaging is shown in Fig. 1b. The spatial distribution is almost flat on the whole sample surface except for the sample edge. The Y-ion distribution at golden-yellow areas is similar to that at black areas (for instance, the open solid circles in Fig. 1). This implies that the BG transition as well as the BG separation does not originate from the spatial concentration distribution of Y-ions.

Figure 1c shows the spatial distribution of  $N_{\text{eff}}$ .  $N_{\text{eff}}$  at the golden-yellow area reasonably increases from that at the black area. However, we can recognize that some part of the black area has larger  $N_{\text{eff}}$  than the other black area (for instance, the open dashed circle in Fig. 1), i.e., the metallic conduction appears even in the black phase. This result suggests that the insulator-to-metal transition of  $\text{Sm}_{1-x}\text{Y}_x\text{S}$  does not relate to the BG transition.

[1] e.g. L. Zhang *et al.*, Science **298** (2002) 805.

[2] P. Wachter, In Handbook on the Physics and Chemistry of Rare Earth, edited by K. A. Gschneidner *et al.*, (North-Holland, Amsterdam, 1994), Vol. 19, p. 383.

[3] K. Imura *et al.*, J. Korean Phys. Soc. **62** (2013) 2028.

[4] S. Kimura *et al.*, UVSOR Activity Report 2013 **41** (2014) 90.

[5] S. Kimura *et al.*, UVSOR Activity Report 2012 **40** (2013) 45.

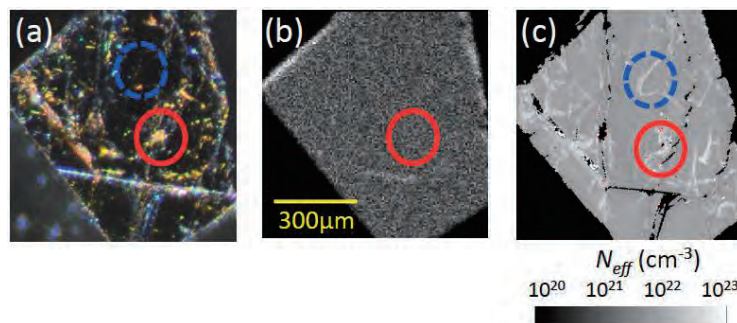


Fig. 1. (a) Visible image of a measured sample of  $\text{Sm}_{0.83}\text{Y}_{0.17}\text{S}$ . (b) Spatial distribution of the intensity of the Y  $K\alpha$  line probed by X-ray fluorescence imaging. (c) Spatial distribution of the effective carrier density ( $N_{\text{eff}}$ ) from the Drude and Lorentz fitting of reflectivity spectra. Open solid (red) and dashed (blue) circles indicate the points of a typical golden phase area and a black phase area with different carrier density, respectively, discussed in the text.

BL7U

## Local Electron-Phonon Coupling in Organic Single Crystals: Angle-Resolved Ultraviolet Photoemission Study

F. Bussolotti<sup>1</sup>, J. Yang<sup>2</sup>, T. Yamaguchi<sup>2</sup>, Y. Nakayama<sup>2</sup>, H. Ishii<sup>2</sup>, M. Matsunami<sup>1</sup>, N. Ueno<sup>2</sup> and S. Kera<sup>1,2</sup>

<sup>1</sup>Department of Photomolecular Science, Institute of Molecular Science, Okazaki 444-8585, Japan,

<sup>2</sup>Department of Nanomaterial Science, Graduate School of Advanced Integration Science, Chiba University, Chiba 263-8522, Japan

A detailed understanding of the electronic and transport properties of organic semiconductors is crucial for the optimization of any real organic-based (opto)electronic devices. Despite huge research efforts important open issues still remain, as mainly related to the role played by the electronic delocalization and electron-phonon coupling effects on the charge transport mechanism in organic materials [1]. In this work, we clearly revealed the impact of electron-phonon coupling on the electronic band dispersion of rubrene single crystals (SCs) by angle-resolved ultraviolet photoelectron spectroscopy (ARUPS).

The ARUPS study was conducted at BL7U. The photon energy ( $h\nu$ ) was set to  $h\nu=8$  eV. During photoemission measurements the SCs were continuously irradiated with laser light (photon energy=3.06 eV, power=14 mW) to avoid sample charging [2]. The energy and angular resolution was 10 meV and  $0.15^\circ$  respectively.

Figure 1(a) shows the UPS spectra of the highest occupied molecular orbital (HOMO) of rubrene SC as acquired along the  $\Gamma Y$  symmetry direction at 307 K (room temperature). In particular, a “kink”-like dispersive behavior is observed at  $\theta \sim 20^\circ$ . This striking spectral feature is more clearly revealed by the  $E(k_{\parallel})$  band mapping of the HOMO dispersion [Fig. 1(b)]. The kink structure is centered at  $k_{\parallel}^{\text{kink}} = \sim 0.23 \text{ \AA}^{-1}$  with an energy width of  $\sim 130$  meV, which nearly coincides with the characteristic energy of the rubrene intramolecular vibrations ( $h\nu_0^{\text{rub}} = 130$  meV) [3]. Upon crossing the kink structure (from  $\Gamma$  to  $Y$ ) a clear broadening of the HOMO peak is observed [Fig. 1(c), left panel].

The occurrence of kink structures in the electronic band dispersions of organic molecular solids was theoretically predicted by Ciuchi *et al.* [4] as a result of the interaction of electrons with high frequency intramolecular vibrations [4]. This *local* electron-phonon coupling introduces “cuts” in the electronic band dispersion at multiple of the intramolecular vibrational energy, resulting in kink structures as those observed in the present rubrene SC.

According to the above picture, electron-phonon scattering events are allowed only for  $k_{\parallel} > k_{\parallel}^{\text{kink}}$  (i.e. at higher binding energies) where they cause the observed increase of the HOMO linewidth [Fig. 1(c), left panel]. These *local* electron-phonon coupling

effects are substantially temperature independent in the [307K–110K] temperature range ( $kT < 26$ meV) as the rubrene intramolecular vibrations ( $h\nu_0^{\text{rub}}=130$  meV) cannot be excited when  $kT \ll h\nu_0^{\text{rub}}$ .

According to our ARUPS results, the electronic band structure of rubrene SC is significantly affected by *local* electron-phonon coupling effects. The most salient spectral features come from the interaction of electrons with high-frequency intramolecular vibrations which causes the appearance in (i) kink structure in the electron band dispersion and (ii) scattering of higher binding energies electrons.

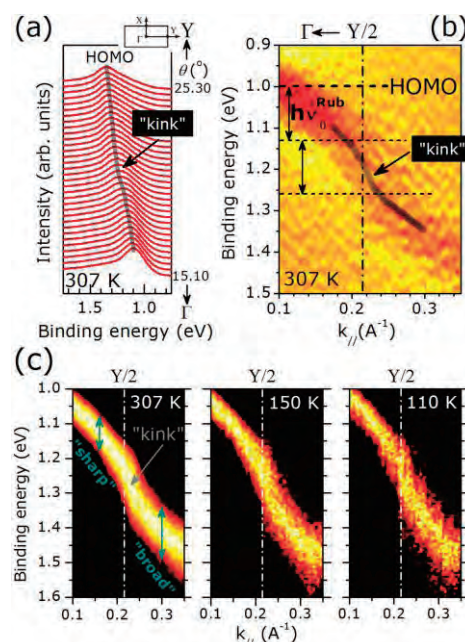


Fig. 1. (a)  $\theta$ -dependence of the HOMO-UPS spectra of rubrene single crystal along  $\Gamma Y$  direction (see inset) ( $h\nu=8$  eV). (b)  $E(k_{\parallel})$  map of the HOMO band dispersion (second derivative intensity plot,  $\Gamma Y$  direction). (c)  $E(k_{\parallel})$  map of the HOMO band dispersion at 307 K, 150 K and 110 K. The spectral intensities were normalized to the intensity of the HOMO peak.

[1] N. Ueno *et al.*, Prog. Surf. Sci. **83** (2008) 490.

[2] S. Machida *et al.*, Phys. Rev. Lett. **104** (2010) 156401.

[3] S. Duhm *et al.*, Adv. Mat. **24** (2012) 901.

[4] S. Ciuchi *et al.*, Phys. Rev. Lett. **106** (2011) 166406.

BL7U

## Valence Band Dispersion of the Pentacene Single Crystal

Y. Nakayama<sup>1</sup>, M. Yamamoto<sup>2</sup>, Y. Mizuno<sup>2</sup>, M. Matsunami<sup>3</sup>, H. Ishii<sup>2,4</sup> and N. Ueno<sup>2</sup>

<sup>1</sup>Department of Pure and Applied Chemistry, Faculty of Science and Technology, Tokyo University of Science, Noda 278-8510, Japan

<sup>2</sup>Graduate School of Advanced Integration Science, Chiba University, Chiba 263-8522, Japan

<sup>3</sup>UVSOR Facility, Institute for Molecular Science, Okazaki 444-8585, Japan

<sup>4</sup>Center for Frontier Science, Chiba University, Chiba 263-8522, Japan

Pentacene (C<sub>22</sub>H<sub>14</sub>) is one of the most vigorously studied organic semiconductors because a practical magnitude of the field effect mobility of conductive holes ( $\mu_h > 1 \text{ cm}^2\text{V}^{-1}\text{s}^{-1}$ ) at room temperature (RT) was discovered for the first time for organic thin film transistors [1]. In particular, the single crystal phase of pentacene is attracting notable interest because further greater  $\mu_h$  ( $35 \text{ cm}^2\text{V}^{-1}\text{s}^{-1}$  at RT and over  $50 \text{ cm}^2\text{V}^{-1}\text{s}^{-1}$  at 225 K) was reported [2]. As a primary factor for such excellent electric conduction properties, the valence band dispersion structures of the pentacene single crystal (Pn-SC) have been intriguing researchers of fundamental as well as applied science fields. However, experimental demonstration of the valence band structures of *insulating* organic semiconductor single crystal samples has been problematic due to “sample charging”. Photoconductivity of organic semiconductors provides one solution against this drawback, actually *k*-integrated density-of-states of the Pn-SC were disclosed by means of photoelectron spectroscopy under laser light illumination [3,4]. In the present study, we elucidated the valence band structures of the Pn-SC by a photoconductivity-assisted angle-resolved ultraviolet photoelectron spectroscopy (ARUPS) technique.

Oblong plates (typically several mm<sup>2</sup> wide and a few  $\mu\text{m}$  thick) of the Pn-SC produced by a physical vapor transport technique were selected and posted individually onto conductive carbon tape to prepare specimens. Ag glue was additionally pasted at the rim of each crystal to ensure good electric conductivity. ARUPS measurements were carried out at BL7U in UVSOR, where the excitation photon energy ( $h\nu$ ) was set at 10 eV in this study. In order to cancel sample charging, the sample was shined by continuous wave laser light (405 nm) during the measurements [5].

Figure 1(a) shows the ARUPS spectra taken at RT toward a diagonal direction of the surface Brillouin zone of the Pn-SC where the widest energy dispersion of the valence band is theoretically expected [6]. The upper and lower valence bands originating from the highest occupied states of two crystallographically inequivalent pentacene molecules exhibit clear energy dispersion to split each other by tilting the photoelectron take-off angle ( $\theta$ ) from the surface normal. It is worth mentioning that this dispersion direction is opposite to that of another crystalline polymorph (so called “thin-film” phase) of pentacene,

where the two bands split at the  $\Gamma$  point (normal emission) and degenerate each other for the grazing emission [7], but agrees with the trend of one other phase (“bulk” phase) [8]. Cooling the sample temperature down to 115 K resulted in expansion of the band width by *ca.* 20 % as shown in Fig. 1(b) and (c), which should be attributed to reduced electron-phonon coupling at lower temperature [9].

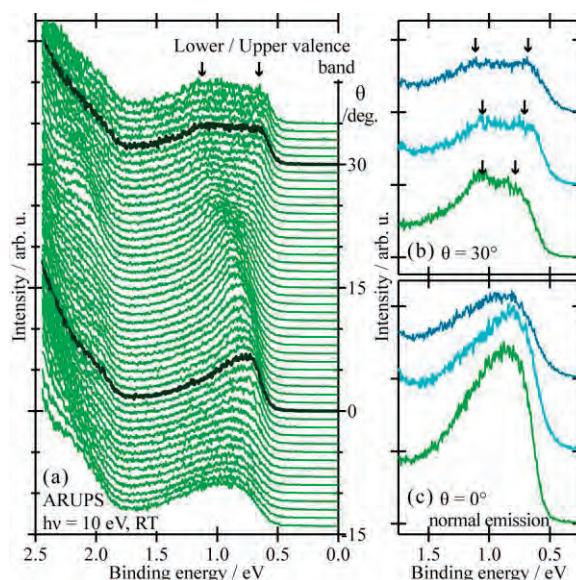


Fig. 1. (a) ARUPS spectra of a Pn-SC sample. (b) and (c) Temperature dependent evolution of UPS spectra (green: RT, light blue: 211 K, blue: 115 K) at electron take-off angles of 30° and 0°, respectively.

- [1] Y.-Y. Lin *et al.*, IEEE Electron Device Lett. **18** (1997) 606.
- [2] O. Jurchescu *et al.*, Appl. Phys. Lett. **84** (2004) 3061.
- [3] A. Vollmer *et al.*, Euro. Phys. J. E **17** (2005) 339.
- [4] Y. Nakayama *et al.*, Jpn. J. Appl. Phys. **53** (2014) 01AD03.
- [5] S. Machida *et al.*, Phys. Rev. Lett. **104** (2010) 156401.
- [6] H. Yoshida *et al.*, Phys. Rev. B **77** (2008) 235205.
- [7] M. Ohtomo *et al.*, Appl. Phys. Lett. **95** (2009) 123308.
- [8] H. Kakuta *et al.*, Phys. Rev. Lett. **98** (2007) 247601.
- [9] N. Koch *et al.*, Phys. Rev. Lett. **96** (2006) 156803.

BL7U

## Angle-Resolved Photoemission Study on Quasi-One Dimensional Organic Conductor (TMTTF)<sub>2</sub>PF<sub>6</sub>

T. Ito<sup>1,2</sup>, M. Mitamura<sup>1</sup>, H. Horikawa<sup>1</sup>, T. Hajiri<sup>1</sup>, S. Kimura<sup>3,4</sup> and T. Nakamura<sup>5</sup>

<sup>1</sup>Graduate School of Engineering, Nagoya University, Nagoya 464-8603, Japan

<sup>2</sup>Nagoya University Synchrotron Radiation Research Center, Nagoya University, Nagoya 464-8603, Japan

<sup>3</sup>Graduate School of Frontier Biosciences, Osaka University, Suita 565-0871, Japan

<sup>4</sup>Department of Physics, Osaka University, Suita 565-0871, Japan

<sup>5</sup>Institute for Molecular Science, Okazaki 444-8585, Japan

The Bechgaard salts (TMTCF)<sub>2</sub>X (C = S, Se; X = PF<sub>6</sub>, AsF<sub>6</sub>, etc.) belong to a family of quasi-one-dimensional (Q1D) organic conductors. These materials allow for a variety of ground states from antiferro magnetism, a Peierl's-like spin density wave, to a superconducting state by tuning the chemical pressure with the combination of TMTSF/TMTTF and anion X [1].

In this study, we have performed temperature dependent angle-resolved photoemission spectroscopy (ARPES) on single-crystalline (TMTTF)<sub>2</sub>PF<sub>6</sub> to clarify the relation between the electric structure and the thermodynamic properties. ARPES measurement were performed at UVSOR-III BL7U by utilizing the bulk-sensitive low photon energy ( $h\nu = 8\text{ eV}$ ) as well as the micro focus beam ( $15 \times 100 \mu\text{m}^2$ ).

Figure 1 (a) and (b) shows the ARPES spectra and image along the  $\Gamma X$  direction of (TMTTF)<sub>2</sub>PF<sub>6</sub> at  $T = 30\text{ K}$  (charge ordering state: CO). We found highly dispersive band (h) folded around  $k = 0.27 \text{ \AA}^{-1}$  (red arrow) at 0.4 eV, the dispersive broad feature (s) and the broad shoulder (p) below the Fermi level ( $E_F$ ). From the comparison with the previous ARPES study on (TMTSF)<sub>2</sub>X [2, 3], we have expected that the observed three features are attributed to holon, spinon and polaron band, respectively. It should be noted that the holon/spinon bands shift away from  $E_F$  relative to (TMTSF)<sub>2</sub>PF<sub>6</sub> in consistent with the insulating properties of (TMTTF)<sub>2</sub>PF<sub>6</sub> at CO states.

Figure 3 shows temperature dependent ARPES spectrum at  $k = 0.27 \text{ \AA}^{-1}$  from  $T = 30\text{ K}$  (CO), 100 K, 200 K (charge localization state: loc) to 300 K (metallic state: M) [4]. With increasing temperature, the main peak at 0.4 eV becomes weak and almost disappears at  $T = 300\text{ K}$ . As a result, the band structure at the metallic state dominates with the high-energy bound states (loc in Fig. 1) below 1 eV. On the other hand, we found that the spectral weight at  $E_F$  increases from  $T = 30\text{ K}$  to 300 K, which is consistent with the thermodynamic properties of (TMTTF)<sub>2</sub>PF<sub>6</sub>. We have found the good reproducibility of the observed temperature dependence with decreasing temperature, which ensure the less radiation damage effect during the present ARPES measurement.

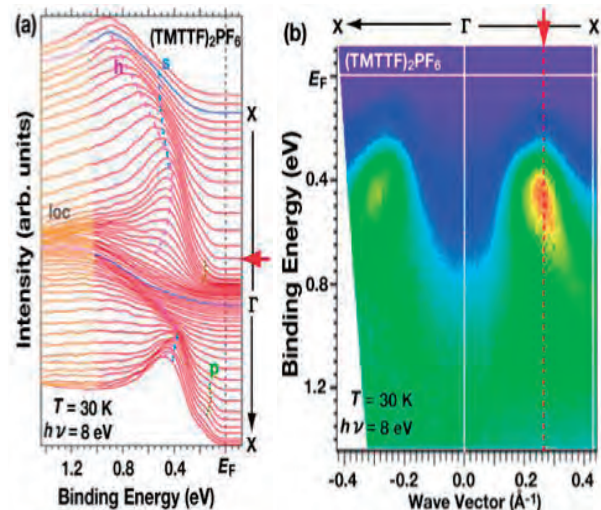


Fig. 1. ARPES spectra (a) and image of (TMTTF)<sub>2</sub>PF<sub>6</sub> along  $\Gamma X$  direction at  $T = 30\text{ K}$ . Dashed lines are guide for eyes. Red arrow indicates the top of the holon dispersion.

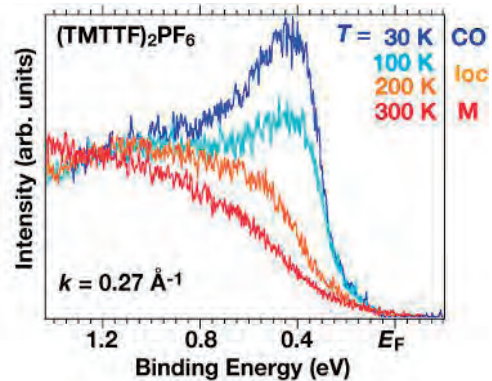


Fig. 2. Temperature dependent ARPES spectrum of (TMTTF)<sub>2</sub>PF<sub>6</sub> at the top of the holon dispersion ( $k = 0.27 \text{ \AA}^{-1}$ ).

[1] T. Ishiguro *et al.*, *Organic Superconductors* (Springer-Verlag, Berlin, 1998).

[2] S. Hirate *et al.*, UVSOR Activity Report 2011 **39** (2012) 97.

[3] M. Mitamura *et al.*, UVSOR Activity Report 2012 **40** (2013) 110.

[4] E. Rose *et al.*, *J. Phys.: Condens. Mat.* **25** (2013) 014006.

BL7U

## Carrier Concentration Dependence of Superconducting Gap of $\text{Bi}_{1.7}\text{Pb}_{0.4}\text{Sr}_2\text{Ca}_{1-x}\text{Y}_x\text{Cu}_2\text{O}_{8+\delta}$

H. Sakamoto<sup>1</sup>, A. Yamamoto<sup>2</sup> and T. Takeuchi<sup>2,3</sup>

<sup>1</sup>Department of Crystalline Materials Science, Nagoya University, Nagoya 464-8603, Japan

<sup>2</sup>Toyota Technological Institute, Nagoya 468-8511, Japan

<sup>3</sup>Promoting Individual Research to Nurture the Seeds of Future Innovation, Japan Science and Technology Agency, Tokyo 102-8666, Japan

Despite a huge number of investigations being performed after the discovery of high- $T_c$  cuprate superconductors, the collective excitation leading to the formation of Cooper-pairs has not been fully identified yet. In order to gain deep insight into such collective excitation, it is of great importance to know the temperature-, momentum-, and carrier concentration- dependences of superconducting gap. Unfortunately, however, the pseudogap developing at the underdoped condition has made it difficult to reveal the temperature-, momentum-, and carrier concentration- dependences of superconducting gap. In this study, therefore, we carefully investigated the energy-width of superconducting-gap  $\Delta(\varphi, p) = \Delta_0(p)\cos\varphi$  for  $\text{Bi}_{1.7}\text{Pb}_{0.4}\text{Sr}_2\text{Ca}_{1-x}\text{Y}_x\text{Cu}_2\text{O}_{8+\delta}$  using ultra-high-energy-resolution laser induced angle resolved photoemission spectroscopy (ARPES) measurements. Here  $\varphi$  and  $p$  indicate the angle from the  $(0, 0)$ - $(\pi, \pi)$  direction and the introduced hole-concentration from the half-filled condition at  $p = 0$ . By additionally employing the synchrotron radiation ARPES measurements at BL7U in UVSOR, we estimated the carrier concentration of the employed samples using the area surrounded by the Fermi surface.

Figure 1 shows a symmetrized  $\mathbf{k}_F$ -ARPES spectrum of  $\text{Bi}_{1.7}\text{Pb}_{0.4}\text{Sr}_2\text{Ca}_{0.9}\text{Y}_{0.1}\text{Cu}_2\text{O}_{8+\delta}$  at  $\varphi \approx 23^\circ$  as a typical example. The magnitude of  $\Delta(\varphi, p)$  was defined as the energy difference between two peaks in a symmetrized spectrum. The magnitude of  $\Delta(23^\circ, p)$  of  $\text{Bi}_{1.7}\text{Pb}_{0.4}\text{Sr}_2\text{Ca}_{0.9}\text{Y}_{0.1}\text{Cu}_2\text{O}_{8+\delta}$  was determined to be  $\sim 56$  meV. In the same manner as,  $\Delta(23^\circ, p)$ ,  $\Delta(\varphi, p)$  was precisely determined at various angles of  $\varphi$ .

By plotting  $\Delta(\varphi, p)$  as a function of  $\cos\varphi$ , we quantitatively evaluated  $\Delta_0(p)$  for there different samples possessing different value of  $p$ . The determined  $\Delta_0(p)$  was plotted in Fig. 2. as a function of  $p$  together with those previously determined for  $\text{Bi}_2(\text{Sr,RE})_2\text{CuO}_{6+d}$  (RE = La, Nd, Sm).

We found, in our previous study, that  $\Delta_0(p)$  of  $\text{Bi}_2(\text{Sr,RE})_2\text{CuO}_{6+d}$  falls on a universal curve regardless of the rare earth elements involved in the samples: it obviously increases with decreasing hole

concentration at overdoped region and turns out to be reduced with decreasing hole concentration after becoming maximal at around  $p = 0.23$  holes/Cu. Notably,  $\Delta_0(p)$  of present samples ( $\text{Bi}_{1.7}\text{Pb}_{0.4}\text{Sr}_2\text{Ca}_{1-x}\text{Y}_x\text{Cu}_2\text{O}_{8+\delta}$ ) shows a fairly different behavior from the universal curve observed for  $\text{Bi}_2(\text{Sr,RE})_2\text{CuO}_{6+d}$ . The much larger magnitude of  $\Delta_0(p)$  of the present samples than that of  $\text{Bi}_2(\text{Sr,RE})_2\text{CuO}_{6+d}$  would be closely related with the difference in the maximum critical temperature:  $T_{c-\text{max}} \sim 90$  K of  $\text{Bi}_{1.7}\text{Pb}_{0.4}\text{Sr}_2\text{Ca}_{1-x}\text{Y}_x\text{Cu}_2\text{O}_{8+\delta}$  and  $T_{c-\text{max}} \sim 40$  K of  $\text{Bi}_2(\text{Sr,RE})_2\text{CuO}_{6+d}$ .

It would be more important to note that  $\Delta_0(p)$  of present samples shows a shape peak at around  $p \sim 0.16$  while that of  $\text{Bi}_2(\text{Sr,RE})_2\text{CuO}_{6+d}$  exhibits a shallow hump in the  $\Delta_0 - p$  plot. The mechanism leading to the different carrier concentration dependence of  $\Delta_0(p)$  would be closely related to the difference in critical temperature of Cooper-pair formation.

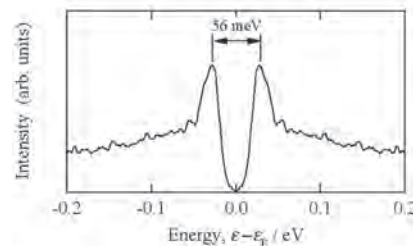


Fig. 1. Symmetrized ARPES spectrum at  $\mathbf{k}_F$  measured for  $\text{Bi}_{1.7}\text{Pb}_{0.4}\text{Sr}_2\text{Ca}_{0.9}\text{Y}_{0.1}\text{Cu}_2\text{O}_{8+\delta}$  at around  $\varphi = 23^\circ$ . The temperature of measurement was  $\sim 13$  K.

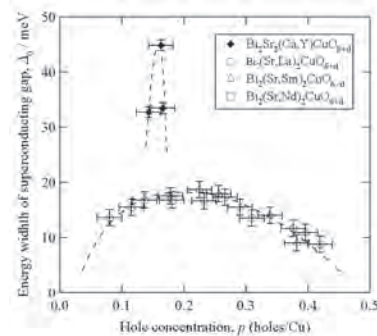


Fig. 2. Hole-concentration dependence of  $\Delta_0$  determined for  $\text{Bi}_{1.7}\text{Pb}_{0.4}\text{Sr}_2\text{Ca}_{1-x}\text{Y}_x\text{Cu}_2\text{O}_{8+\delta}$  and  $\text{Bi}_2(\text{Sr,RE})_2\text{CuO}_{6+d}$ .

BL7U

## Angle-Resolved Photoemission Study of Heusler-Type $\text{Fe}_2\text{V}_{1+x}\text{Al}_{1-x}$ Alloys

H. Miyazaki, K. Ando, W. Nagasaka and Y. Nishino

Department of Frontier Materials, Nagoya Institute of Technology, Nagoya 466-8555, Japan

Band structure calculations of  $\text{Fe}_2\text{VAl}$  alloy have predicted that a pseudo-gap is formed around the Fermi level [1]. Because of the possession of a sharp pseudo-gap across the Fermi level,  $\text{Fe}_2\text{VAl}$ -based alloys have attracted a great deal of interest as potential candidates for next-generation thermoelectric materials [2]. The peak temperature of the n-type thermoelectric power factor of previous Fe-based Heusler alloys is around 300 - 400 K [3]. For the application of thermoelectric materials to power generation, it is desirable that the peak temperature of both the n- and p-type be increased to 400-600 K. Recently, the substitution of Al or V atoms with V or Al atoms in the off-stoichiometric  $\text{Fe}_2\text{V}_{1+x}\text{Al}_{1-x}$  compounds has proven to improve significantly the p- and, especially, n-type thermoelectric properties, such as electronic resistivity and Seebeck coefficient, and allows a shift of the peak performances towards interesting higher temperatures (300 - 600K) [4]. In order to clarify the origin of the improvement in the thermoelectric properties for the off-stoichiometric  $\text{Fe}_2\text{V}_{1+x}\text{Al}_{1-x}$  alloys, we thus performed high-resolution three-dimensional angle-resolved photoemission spectroscopy (3D-ARPES) measurements to investigate the change in the electronic structure due to the V/Al off-stoichiometry.

SR-PES measurements were carried out in the beamline BL7U of the UVSOR-III. Photoemission spectra were recorded at 10 K. Clean surfaces for 3D-ARPES measurements were obtained by *in-situ* fracturing with a knife edge at 10 K under ultra-high vacuum. Fermi level and total energy resolution were determined by the Fermi edge of evaporated gold films. The total energy and momentum resolutions for the 3D-ARPES measurement were set to 15 meV and  $0.006 \text{ \AA}^{-1}$  at the X point ( $h\nu = 26 \text{ eV}$ ).

Figure 1(a) and (b) shows the second derivative 3D-ARPES images of  $\text{Fe}_2\text{V}_{1.03}\text{Al}_{0.97}$  (electron-doping) and  $\text{Fe}_2\text{V}_{0.97}\text{Al}_{1.03}$  (hole-doping) alloys along X- $\Gamma$  line, respectively. We observed three dispersion of the band around X point, which is consistent with the band structure calculation. All bands of  $\text{Fe}_2\text{V}_{0.97}\text{Al}_{1.03}$  alloy shift to lower binding energy side compared to that of  $\text{Fe}_2\text{V}_{1.03}\text{Al}_{0.97}$  alloy. This indicates that, the number of valence electrons around Fe, V and Al atoms decreases with increasing Al content (hole doping), and that the core level of Fe, V and Al gradually shifts to lower binding energy side because of the chemical potential shift. However, the energy dispersion ( $\sim 30 \text{ meV}$ ) of  $\text{Fe}_2\text{V}_{1.03}\text{Al}_{0.97}$  alloy is smaller than that ( $\sim 70 \text{ meV}$ ) of  $\text{Fe}_2\text{V}_{0.97}\text{Al}_{1.03}$  alloy. This result indicates that the electronic structure near

the Fermi level is modified due to the off-stoichiometric effect and the pseudo-gap widens. According to band structure calculations, a wider pseudo gap leads to a further shift in the peak temperature of the maximum thermoelectric power to the higher temperature side [5]. Therefore, it is thought that the origin of the improvement in n-type Seebeck coefficient and its peak temperature should be attributed to the modification in the electronic structure due to the off-stoichiometric effect.

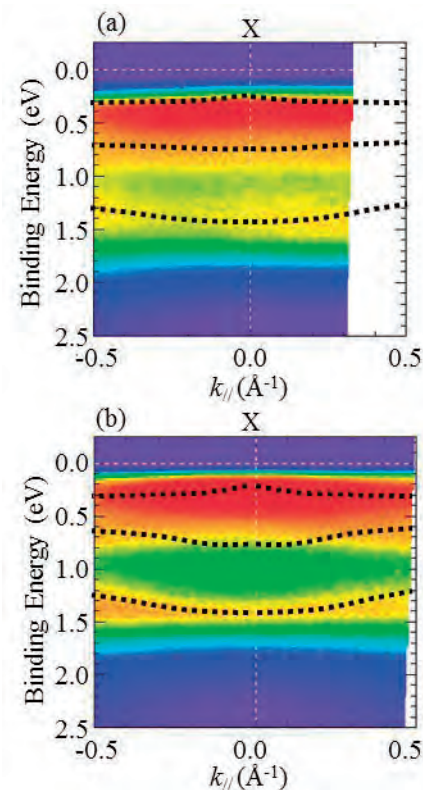


Fig. 1. Second derivative 3D-ARPES images of  $\text{Fe}_2\text{V}_{1.03}\text{Al}_{0.97}$  (electron-doping) and  $\text{Fe}_2\text{V}_{0.97}\text{Al}_{1.03}$  (hole-doping) alloys along X- $\Gamma$  line. The dashed lines indicate the peaks in the second-derivative spectra that correspond to the shoulder and peaks in the spectra.

- [1] G. Y. Guo, G. A. Botton, and Y. Nishino, *J. Phys.: Condens. Matter* **10** (1998) L119.
- [2] Y. Nishino, *The Science of Complex Alloy Phases* (Warrendale: TMS) (2005) 325.
- [3] Y. Nishino, S. Deguchi and U. Mizutani, *Phys. Rev. B* **74** (2006) 115115.
- [4] H. Miyazaki, S. Tanaka, N. Ide, K. Soda and Y. Nishino, *Mater. Res. Express* **1** (2014) 015901.
- [5] D. Do, M. Lee and S. D. Mahanti, *Phys. Rev. B* **84** (2011) 125104.

BL7U

## Angle-Resolved Photoemission Spectroscopy of YbB<sub>12</sub> (001) Surface

K. Hagiwara<sup>1</sup>, J. Kishi<sup>1</sup>, Y. Ohtsubo<sup>2,1</sup>, H. Miyazaki<sup>3</sup>, T. Ito<sup>4</sup>, M. Matsunami<sup>5</sup>,  
F. Iga<sup>6</sup> and S. Kimura<sup>2,1</sup>

<sup>1</sup>Department of Physics, Osaka University, Toyonaka 560-0043, Japan

<sup>2</sup>Graduate School of Frontier Biosciences, Osaka University, Suita 565-0871, Japan

<sup>3</sup>Department of Frontier Materials, Nagoya Institute of Technology, Nagoya 466-8555, Japan

<sup>4</sup>Department of Materials Engineering, Nagoya University, Nagoya 464-8603, Japan

<sup>5</sup>UVSOR Facility, Institute for Molecular Science, Okazaki 444-8585, Japan

<sup>6</sup>Department of Physics, Ibaraki University, Mito 310-0056, Japan

Ytterbium dodecaboride YbB<sub>12</sub> is known as one of typical Kondo insulators/semiconductors (KIs), which has a tiny energy gap owing to the hybridization between conduction and localized 4*f* electrons, namely *c-f* hybridization [1]. Since so many experimental and theoretical studies on the physical properties have been performed over three decades, the overall physical properties have been revealed. The electronic structure has also been investigated by using optical conductivity [2], angle-integrated photoemission spectroscopy (AIPES) [3], time-resolved AIPES [4], and so on. However, the band dispersion as well as *E-k* curves probed by angle-resolved photoemission spectroscopy (ARPES) along the high symmetry lines has never been clarified experimentally because the sample cannot be cleaved along principal axes. Here, we report the ARPES result of a well-defined surface of YbB<sub>12</sub>.

A single crystalline sample was fabricated by a floating-zone method. The sample was cut along the (001)-plane and polished up to a mirror surface by using a diamond lapping film sheet. The clean sample surface was obtained by annealing indirectly heated by SiC plate at the sample temperature of 1250 °C under an ultra-high vacuum better than 5×10<sup>-8</sup> Pa. The obtained low-energy electron diffraction (LEED) image is shown in Fig. 1. The LEED image indicates the square lattice pattern that is the same as the bulk crystal.

The obtained ARPES image near the Fermi level (*E<sub>F</sub>*) at the excitation photon energy of 16 eV is shown in Fig. 2. The observed highly dispersive bands at the binding energy below 0.3 eV mainly originates from the Yb 5*d* conduction band because of the higher cross-section at the photon energy than expected other bands, for instance Yb 4*f*. The peaks of momentum-distribution curves (MDCs) and energy-distribution curves (EDCs), which indicate the trace of the band dispersion, are plotted by open circles and triangles, respectively. The trace indicates that the conduction band becomes gentle below the binding energy of 0.1 eV suggesting that the conduction band is hybridized to localized Yb 4*f* bands located near *E<sub>F</sub>*. The energy gap between the bonding and antibonding states of the *c-f* hybridization is expected to be about 50 meV, which

is consistent with that observed in the optical conductivity spectrum [2].

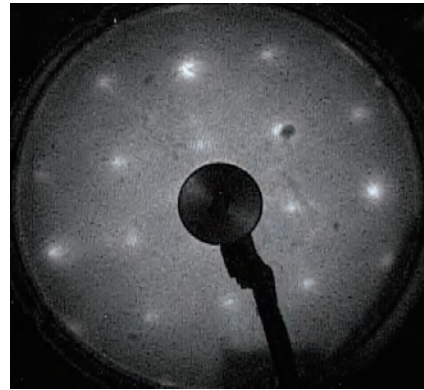


Fig. 1. LEED pattern of the YbB<sub>12</sub> (001) surface with an electron energy of 26.3 eV. Spots represent diffractions of 1×1.

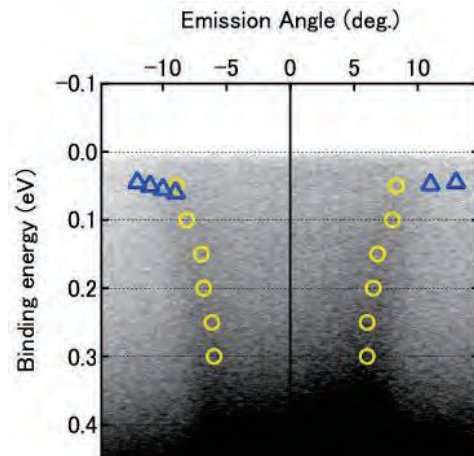


Fig. 2. ARPES image of the YbB<sub>12</sub> (001) surface along the (100) direction at the excitation photon energy of 16 eV. Open circles and triangles are peaks taken from the MDCs and EDCs, respectively.

[1] F. Iga *et al.*, J. Magn. Magn. Mater. **177–181** (1998) 337.

[2] H. Okamura *et al.*, J. Phys. Soc. Jpn. **74** (2005) 1954.

[3] T. Susaki *et al.*, Phys. Rev. Lett. **77** (1996) 4269.

[4] M. Okawa *et al.*, arXiv: 1407.0578.

BL7U

## Quadratic Fermi Node in a 3D Strongly Correlated Semimetal

T. Kondo<sup>1</sup>, M. Nakayama<sup>1</sup>, R. Chen<sup>2</sup>, J. J. Ishikawa<sup>1</sup>, E.-G. Moon<sup>2</sup>,  
 W. Malaeb<sup>1</sup>, Y. Ishida<sup>1</sup>, M. Matsunami<sup>3</sup>, S. Kimura<sup>3,4</sup>,  
 S. Nakatsuji<sup>1</sup>, L. Balents<sup>5</sup> and S. Shin<sup>1</sup>

<sup>1</sup>ISSP, University of Tokyo, Kashiwa, 277-8581, Japan

<sup>2</sup>Physics Department, University of California, Santa Barbara, California 93106, USA

<sup>3</sup>UVSOR Facility, Institute for Molecular Science, Okazaki 444-8585, Japan

<sup>4</sup>Graduate School of Frontier Biosciences, Osaka University, Suita 565-0871, Japan

<sup>5</sup>Kavli Institute for Theoretical Physics, Santa Barbara, California 93106, USA

Following the discovery of topological insulators, the next frontier is the regime in which both spin-orbit coupling and correlation effects are strong. Theory has suggested that the pyrochlore iridates ( $Ln_2Ir_2O_7$ ;  $Ln$ =rare earth elements), a family of cubic  $5d$  transition metal oxides, realize both band inversion [1,2], the essential ingredient of topological insulators, and strong correlations. The phenomenological suggestion is that the Fermi surface of  $Pr_2Ir_2O_7$  contains a single Fermi node at the  $\Gamma$  point protected by cubic and time-reversal symmetries, which emerges as the touching point of two quadratically dispersing “conduction” and “valence” bands [Fig.1(a) and Fig.2(e)]. If the assumption is correct, the  $Pr_2Ir_2O_7$  could be a “parent” state tunable to new-types of strongly correlated topological phases [Fig.1(b)-(d)] [1,2]. As the ionic radius of  $Ln$  site increases (for example,  $Ln=Nd$  and  $Eu$ ), the all-in-all-out antiferromagnetic order emerges, which causes the time-reversal symmetry breaking in bulk. This could provide a realization of Weyl fermions that obeys a two-component Dirac equation. It was also predicted to establish remarkable topological properties manifested by surface states in the form of Fermi arcs. The pyrochlore iridates study therefore has enormous potential to open up the next frontier of condensed matter physics.

By ARPES, we have experimentally realized the Fermi node state in  $Pr_2Ir_2O_7$  [see Fig.2]. A parabolic band-dispersion approaches  $E_F$  with increasing photon energies (or  $k_z$  values), and finally touches it at the  $\Gamma$  [Fig.2 (e)]. With a further increase of  $k_z$ , the dispersion gets away from  $E_F$  again, which signifies that the 3D band structure of  $Pr_2Ir_2O_7$  has a single Fermi point. Other scans of different  $k_z$  values up to the L point revealed no other states touching or crossing  $E_F$  [Fig.2(c)]. This satisfies the charge neutrality, and it could be a further evidence for the realization of the Fermi nodal state. As demonstrated in Fig.2(e), we found that our ARPES data is consistent with the result of band calculations.

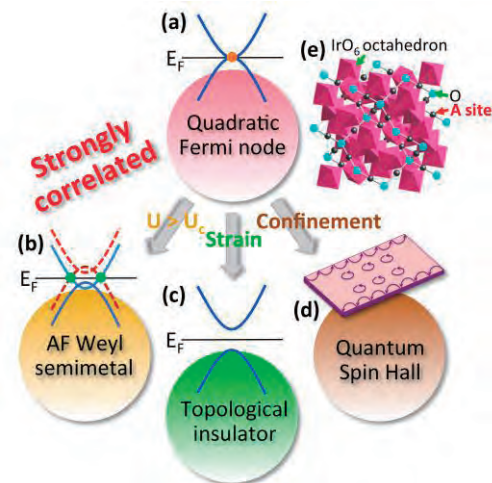


Fig. 1. Schematic diagram illustrating (a) the quadratic Fermi node state of  $Pr_2Ir_2O_7$  and its role as a parent of (b)-(d) interacting topological phases.

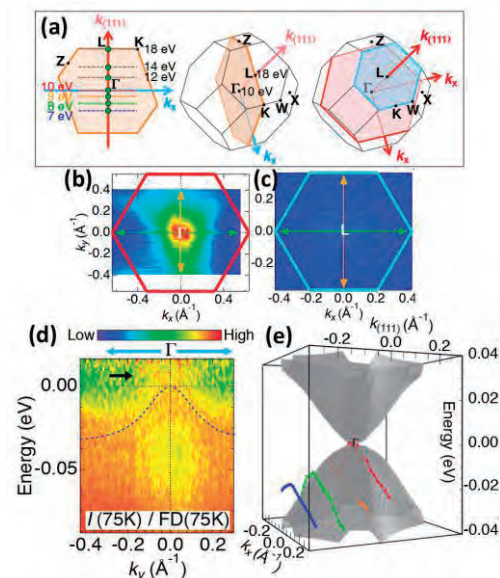


Fig. 2. (a) Brillouin zone. ARPES intensity maps around  $\Gamma$  (b) and L (c). (d) Band dispersion around  $\Gamma$ , divided by the Fermi function. (e) Comparison between ARPES data and band calculation.

[1] D. Pesin *et al.*, Nat. Phys. **6** (2010) 376.

[2] E.-G. Moon *et al.*, Phys. Rev. Lett. **111** (2013) 206401.

BL7U

## ARPES Study on the Stripe-Ordered $(\text{La,Nd,Sr})_2\text{CuO}_4$ Superconductor

K. Tanaka<sup>1</sup>, M. Matsunami<sup>1</sup>, S. Miyasaka<sup>2</sup> and S. Tajima<sup>2</sup>

<sup>1</sup>UVSOR Facility, Institute for Molecular Science, Okazaki 444-8585, Japan

<sup>2</sup>Department of physics, Osaka University, Toyonaka 560-0043, Japan

The “stripe order” is a periodic modulation of one-dimensional charge and spin densities observed in some hole-doped transition metal oxides. It was observed by means of neutron scattering, X-ray diffraction and so on [1,2]. In hole-doped La-214 cuprates, such as  $\text{La}_{2-x}\text{Ba}_x\text{CuO}_4$  (LBCO) and  $\text{La}_{2-x-y}\text{Nd}_y\text{Sr}_x\text{CuO}_4$  (LNSCO), represent this charge and magnetic order coexisting with superconductivity. Recently direct evidence for new charge density wave (CDW) order in  $\text{YBa}_2\text{Cu}_3\text{O}_{7-\delta}$  (YBCO) has been observed in high magnetic field using nuclear magnetic resonance [3] and in zero-field diffraction, with resonant soft x-ray and hard x-ray scattering (RSXS) [4]. Since the superconductivity often emerges in the proximity of, or in competition with, symmetry-breaking ground states such as antiferromagnetism or CDW, the stripe order also has attracted much interests again.

Despite the intense interest and volume of research, there were not many angle-resolve photoemission (ARPES) studies on stripe samples. There were only a few studies on LBCO samples [5,6], which is mainly because it is hard to obtain a sharp peak in ARPES spectrum to discuss the detail of the superconducting gap size. Moreover, the carrier concentration and the strength of the stripe order change simultaneously by changing Ba concentration  $x$  in LBCO, which makes it difficult to understand the effect of the stripe order on the electronic structure, because the electronic structure is sensitive to the carrier concentration in cuprates. To figure out the intrinsic electronic structure of the stripe order, we choose LNSCO system, where the strength of the stripe order solely can be controlled by Nd concentration  $y$ . In this study, to clarify the intrinsic electronic structure of the stripe order, we tried to seek the best ARPES measurement condition for LNSCO samples, namely, an energy and a polarization of the incident light.

LNSCO single crystal ( $x = 0.16$ ,  $y = 0.1$ ) was grown by a traveling solvent floating-zone (TSFZ) method. As-grown sample was annealed on the gold plate in  $\text{O}_2$  atmosphere at 800 degree for 1 week and quenched to the room temperature to make the hole concentration uniform. Superconducting transition temperature of the sample was determined as  $T = 35$  K from the onset in the magnetization measurements. The ARPES measurements were carried out at beamline BL7U of UVSOR-III at the Institute for Molecular Science, using an MBS A-1 analyzer. The energy resolution was set to 10 meV and the angular resolution was about  $0.17^\circ$ . The Fermi level ( $E_F$ ) was

calibrated using an evaporated gold film.

Figure 1 shows photon energy dependence of spectra from 14 eV to 40 eV at nodal  $k_F$  at 1<sup>st</sup> Brillouin Zone (BZ) taken at temperature 12 K. Here the polarization of the light was set along  $(\pi,0)$ - $(0,\pi)$  direction. One can clearly see the peak structure at photon energy 20 and 36 eV. In those photon energies, the Fermi arc can be clearly seen in the Fermi surface mapping (not shown). We also performed measurements with polarization along  $(0,0)$ - $(\pi,\pi)$  direction, however, there were almost no peak and the whole spectral intensity was suppressed. This polarization dependence is consistent with previous calculation [5].

We clarify that the photon energies of 20 and 36 eV can be used for LNSCO measurements at BL7U to perform the detailed superconducting gap study.

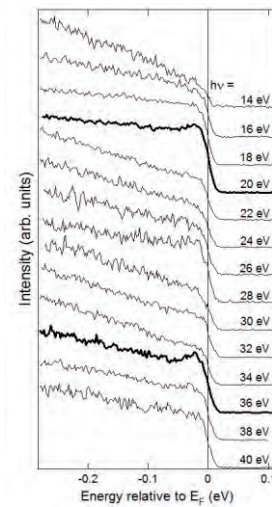


Fig. 1. Photon energy dependence of ARPES spectra of  $\text{La}_{1.74}\text{Nd}_{0.1}\text{Sr}_{0.16}\text{CuO}_4$  at nodal  $k_F$  at 1<sup>st</sup> BZ taken at temperature 12 K.

- [1] J. M. Tranquada *et al.*, Nature, **375** (1995) 561.
- [2] M. Hucker *et al.*, Phys. Rev. B **83** (2011) 104506.
- [3] T. Wu *et al.*, Nature, **477** (2011) 191.
- [4] G. Ghiringhelli *et al.*, Science **337** (2012) 821.
- [3] T. Valla *et al.*, Science **314** (2006) 1914.
- [4] R. H. He *et al.*, Nature Physics **5** (2009) 119.
- [5] A. Bansil *et al.*, Phys. Rev. Lett. **83** (1999) 5154.

BL7U

## ARPES Studies of Hydrogen Exposed MoS<sub>2</sub>

S. Cho<sup>1</sup>, B. Kim<sup>1</sup>, B. Kim<sup>1</sup>, Y. Kim<sup>1</sup>, Y. Koh<sup>1</sup>, J. Seo<sup>1</sup>, J. Kwon<sup>1</sup>, M. Matsunami<sup>2</sup>, K. Tanaka<sup>2</sup>,  
S. R. Park<sup>3</sup> and C. Kim<sup>1</sup>

<sup>1</sup>*Institute of Physics and Applied Physics, Yonsei University, Seoul, Korea*

<sup>2</sup>*Editorial Board, UVSOR Facility, Institute for Molecular Science, Okazaki 444-8585, Japan*

<sup>3</sup>*Department of physics, Incheon National University, Incheon 406-772, Korea*

The physics associated with transition metal dichalcogenides (TMDCs) is one of the most intriguing issues in condensed matter physics. These materials have several interesting aspects inter physical properties, especially the direct to indirect band gap transition from monolayer to bulk and spin band splitting at the K-point. [1,2] There are many studies on the electronic structures of the monolayer TMDCs because of the direct band gap. [3,4,5] At these days, monolayer MoS<sub>2</sub> with direct band gap can be manufactured and it is interested in a variety of areas, such as field effect transistor, optoelectronic applications and so on. But thorough systematic studies on the electronic structures of bulk TMDCs regarding those issues have not been done.

In the early 21 century, molybdenum disulfide (MoS<sub>2</sub>) was used by catalyst for hydrodesulfurization which mean capture and remove sulfur from the crude oil called thiophene by hydrogen sulfide. During this process, there is intermediate state that only sulfur released from MoS<sub>2</sub> such as defect state. We mainly interested in this intermediate state which was known for the mid gap state between conduction band and valence band. [6]

We bought the MoS<sub>2</sub> single crystal from the SPI then we made the cell with low vacuum. For the hydrogen treatment, we put the MoS<sub>2</sub> in the cell and flow the hydrogen under 20 bar pressure at about 350K for 10 hours. [7] Samples were cleaved in situ at room temperature and the chamber pressure was better than  $5 \times 10^{-11}$  Torr. ARPES spectra were acquired with a hemispherical photoelectron analyzer (MBS A-1). We used linearly polarized light with 40eV photon energy.

We present the electronic structure studies of hydrogen exposed MoS<sub>2</sub> by angle resolved photoemission in UVSOR. Figure 1a is the  $\Gamma$ -K fine cut raw data of hydrogen exposed MoS<sub>2</sub>. To see band dispersion more clearly, Fig. 1b is shown as the second derivative data of Fig. 1a. In the K-point, there is a band splitting about 170meV due to strong spin-orbit coupling. [8] It is well matched by theoretical prediction for size of band splitting. The dotted white lines in Fig. 1b are guide to the eye indicating the band dispersions. It was recently reported that the number of band in topmost valence band at  $\Gamma$ -point are corresponding to be the number of layers. [3] The bulk MoS<sub>2</sub> case, it has a one thick band at  $\Gamma$ -point. In our data of Fig. 1b, the valence band at  $\Gamma$ -point shows five distinguished dispersions.

Therefore we assume that the bulk MoS<sub>2</sub> turns into the one of multilayer near surface after high pressure hydrogen treatment.

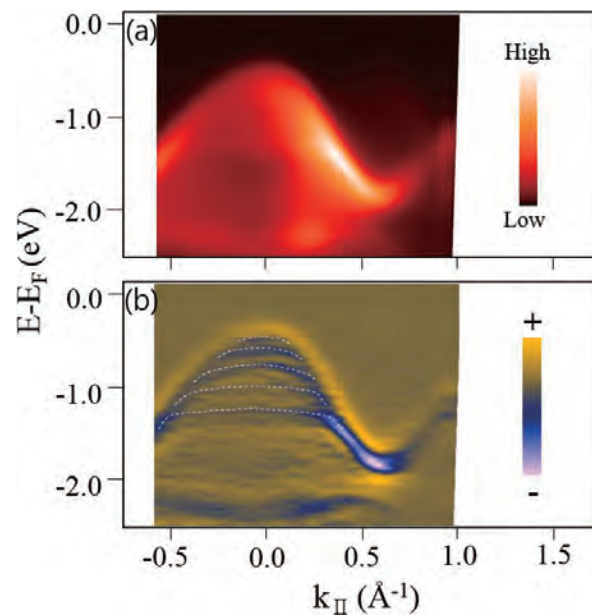


Fig. 1. (a)  $\Gamma$ -K fine cut raw data of hydrogen exposed MoS<sub>2</sub>. Right side is intensity plot of raw data. (b)  $\Gamma$ -K fine cut second derivative data of hydrogen exposed MoS<sub>2</sub>. Right side is sign plot of second derivative data.

- [1] Q. H. Wang *et al.*, Nat. Nanotechnol. **7** (2012) 699.
- [2] Z. Y. Zhu *et al.*, PRB. **84** (2012) 153402.
- [3] Y. Zhang *et al.*, Nat. Nanotechnol. **9** (2014) 111.
- [4] B. Radisavljevic *et al.*, Nat. Nanotechnol. **6** (2011) 147.
- [5] H. J. Conley *et al.*, Nano Lett. **13** (2013) 3626.
- [6] D. Liu *et al.*, Appl. Phys. Lett. **105** (2014) 213508.
- [7] B. H. Kim *et al.*, RCS Advances **3** (2013) 18424.
- [8] J. E. Padilha *et al.*, PR **90** (2014) 205420.

BL7U

## Non-Uniform Temperature-Dependent Band Shift of an Iron Pnictide Superconductor LiFeAs

 T. Hajiri<sup>1,2</sup>, T. Ito<sup>1,3</sup>, M. Matsunami<sup>2,4</sup>, B. H. Min<sup>5</sup>, Y. S. Kwon<sup>5</sup>, K. Kuroki<sup>6</sup> and S. Kimura<sup>2,6,7</sup>
<sup>1</sup>Graduate School of Engineering, Nagoya University, Nagoya 464-8603, Japan

<sup>2</sup>UVSOR Facility, Institute for Molecular Science, Okazaki 444-8585, Japan

<sup>3</sup>Nagoya University Synchrotron Radiation Research Center, Nagoya University, Nagoya, 464-8603, Japan

<sup>4</sup>School of Physical Sciences, SOKENDAI (The Graduate University for Advanced Studies), Okazaki 444-8585, Japan

<sup>5</sup>Department of Emerging Materials Science, DGIST, Daegu 711-873, Republic of Korea

<sup>6</sup>Department of Physics, Graduate School of Science, Osaka University, Toyonaka 560-0043, Japan

<sup>7</sup>Graduate School of Frontier Biosciences, Osaka University, Suita 565-0871, Japan

Iron pnictide superconductors are recently attracted in the change of physical properties above superconducting temperature ( $T_c$ ), such as the in-plane anisotropic resistivity [1], the softening of the  $C_{66}$  mode [2], the orbital-polarized electronic structure between  $d_{xz}$  and  $d_{yz}$  orbitals [3], and the appearance of a pseudogap [4]. Thus, it is considered that the electronic structure as well as the physical property above  $T_c$  is closely related to the appearance of the superconductivity, the electronic structure above  $T_c$  should be investigated to elucidate the origin of the superconductivity of the iron pnictides. In this report, we show the temperature-dependent angle-resolved photoemission spectroscopy (ARPES) results of LiFeAs ( $T_c \sim 19.7$  K) using UVSOR BL7U “SAMRAI” end-station.

Figures 1(a)-1(d) show the ARPES image at the  $\Gamma$  ( $h\nu = 23$  eV) and Z ( $h\nu = 35$  eV) points along the  $\Gamma$ -M and Z-A directions at  $T = 100$  K (above  $T_c$ ) and 12 K (below  $T_c$ ) taken by using  $S$  polarization. There are two hole bands at both of the  $\Gamma$  and Z points; the outer and inner hole bands are attributed to  $d_{xy}$  and  $d_{yz}$  orbitals, respectively [5]. Figures 1(e) and 1(f) show the comparison of each band dispersion at two temperatures of  $T = 100$  and 12 K at the  $\Gamma$  and Z points, respectively. At the  $\Gamma$  point in Fig. 1(e), the observed two bands do not shift with temperature. At the Z point in Fig. 1(f), on the other hand, the inner hole band rigidly shifts to the higher binding energy side by 28 meV with decreasing temperature, though the outer hole band has almost no temperature dependence. Figures 1(g) and 1(h) show the temperature-dependent ARPES images divided by a Fermi-Dirac function at the  $\Gamma$  and Z points, respectively. It is clear that the energy of the top of the inner hole band at the Z point shifts below  $T = 40$  K, but that at the  $\Gamma$  point is constant with temperature.

Recent ultrafast optical measurement reports an appearance of the pseudogap like feature below  $T = 55$  K due to antiferromagnetic fluctuations [6]. Indeed, the spin fluctuation is enhanced with decreasing temperature below about  $T = 50$  K [7]. These temperatures are consistent with that of an appearance of the orbital-dependent band shift, i.e., the band shift

is considered to be strongly related to the spin fluctuation.

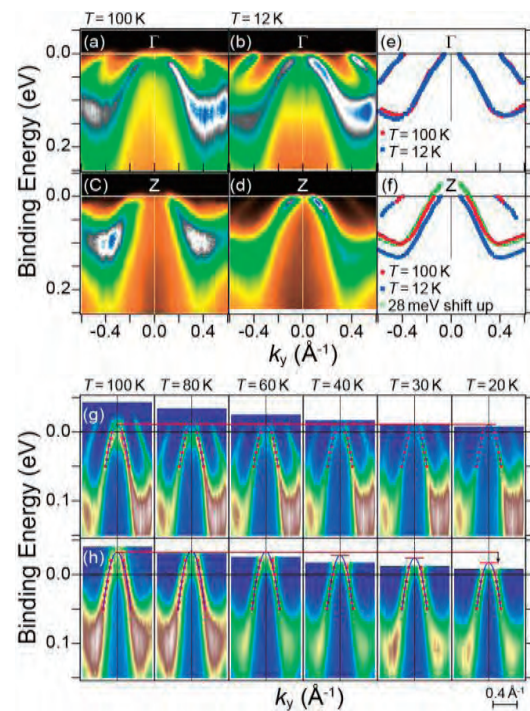


Fig. 1. (a-d) ARPES images along  $\Gamma$ -M/Z-A directions obtained by using  $S$  polarization at  $T = 100$  and 12 K. (e, f) Comparison of each band dispersion. (g, h) Temperature-dependent ARPES images divided by a Fermi-Dirac function.

[1] M. Nakajima *et al.*, Phys. Rev. Lett. **109** (2012) 217003.

[2] M. Yoshizawa *et al.*, J. Phys. Soc. Jpn. **81** (2012) 024604.

[3] M. Yi *et al.*, Proc. Natl. Acad. Sci. **108** (2011) 6878.

[4] T. Shimojima *et al.*, Phys. Rev. B **89** (2014) 045101.

[5] T. Hajiri *et al.*, Phys. Rev. B **85** (2012) 094509.

[6] K.-H. Lin *et al.*, arXiv:1407.3539 (2014).

[7] L. Ma, J. Zhang, G. F. Chen and W. Yu, Phys. Rev. B **82** (2010) 180501(R).

BL7U

## Angle Resolved Photoemission Spectroscopy of Iron Pnictide Superconductor $\text{NdFeP}_{1-x}\text{As}_x(\text{O},\text{F})$

A. Takemori<sup>1</sup>, S. Miyasaka<sup>1</sup>, M. Uekubo<sup>1</sup>, T. Kobayashi<sup>1</sup>, S. Tajima<sup>1</sup>, T. Hajiri<sup>2,3</sup>,  
M. Matsunami<sup>3,4</sup> and K. Tanaka<sup>3,4</sup>

<sup>1</sup>Department of Physics, Graduate School of Science, Osaka University, Toyonaka 560-0043, Japan

<sup>2</sup>Department of Crystalline Materials Science, Graduate School of Engineering, Nagoya University, Nagoya 464-8603, Japan

<sup>3</sup>UVSOR Facility, Institute for Molecular Science, Okazaki 444-8585, Japan

<sup>4</sup>School of Physical Sciences, The Graduate University for Advanced Studies (SOKENDAI), Okazaki 444-8585, Japan

The iron-based superconductors are multiband systems and have various Fermi surface states. These compounds show unconventional superconductivity with high superconducting transition temperature ( $T_c$ ) and have been extremely investigated by many experimental and theoretical groups. Recently, we studied the transport properties in 1111-type P/As solid solution system,  $R\text{FeP}_{1-x}\text{As}_x\text{O}_{1-y}\text{F}_y$  ( $R=\text{La}, \text{Pr}$  and  $\text{Nd}$ ). The results have indicated that this system has two different  $T_c$ -rising mechanism, related to two different Fermi surface states and nesting conditions below and above  $x=0.6\sim 0.8$ . [1, 2] To clarify  $x$ -dependent change of electronic structures and Fermi surfaces, we have investigated the angle resolved photoemission spectroscopy using single crystals of  $\text{NdFeP}_{1-x}\text{As}_x(\text{O},\text{F})$  with  $x=0.4, 0.8$  and  $1.0$  for F concentration  $y\sim 0.1$ .

The single crystals of  $\text{NdFeP}_{1-x}\text{As}_x(\text{O},\text{F})$  were grown by high pressure technique using cubic anvil press and self-flux method. [3]  $T_c$  of the single crystals in the present work were 12 K for  $x=0.4$ , 23 K for  $x=0.8$  and 44 K for  $x=1.0$ , respectively. The angle resolved photoemission spectroscopy were measured at BL7U of UVSOR facility in Institute for Molecular Science. The measurements of Fermi surfaces and electronic band dispersion around  $\Gamma$  and M points were performed at 12 K using incident light with the energy of 36 eV.

The results of the angle resolved photoemission spectroscopy indicate the existence of three hole and two electron Fermi surfaces in  $x=0.4$ , and two hole and two electron Fermi surfaces in  $x=0.8$  and  $1.0$  samples. These Fermi surfaces have two dimensional features (cylindrical shapes), and the hole and electron Fermi surfaces are located around  $\Gamma$  and M points, respectively. The present experiments have clearly revealed that the change of Fermi surface state occurs around  $x=0.8$ . The orbital characters of these Fermi surfaces and electronic bands have been assigned by the polarization-dependent angle resolved photoemission spectroscopy [4], and the  $d_{xz}$  band particularly shows the systematic and important  $x$  dependence. Figure 1 shows the band dispersion around  $\Gamma$  point of  $\text{NdFeP}_{1-x}\text{As}_x(\text{O},\text{F})$  with  $x=0.4, 0.8$  and  $1.0$  by the  $P$ -polarization measurement. In this

polarization configuration, the bands with  $d_{xz}$  and  $d_z^2$  orbital characters have been observed, and the  $d_{xz}$  band exists very near  $\Gamma$  point. As shown in this figure, the  $d_{xz}$  band crosses the Fermi energy and resultantly the  $d_{xz}$  hole Fermi surface exists around  $\Gamma$  point at  $x=0.4$ . The energy level of  $d_{xz}$  band decreases with increasing As concentration  $x$ , and this band almost sinks below Fermi energy around  $\Gamma$  point in the  $x=0.8$  sample. With further increasing  $x$ , this  $d_{xz}$  Fermi surface completely disappears at  $x=1.0$ . The clear changes of Fermi surfaces and electronic structures around  $x=0.8$  are related with the  $x$ -dependent changes of transport and other properties, and support the scenario of two  $T_c$ -rising mechanisms and two Fermi surface states in this system.

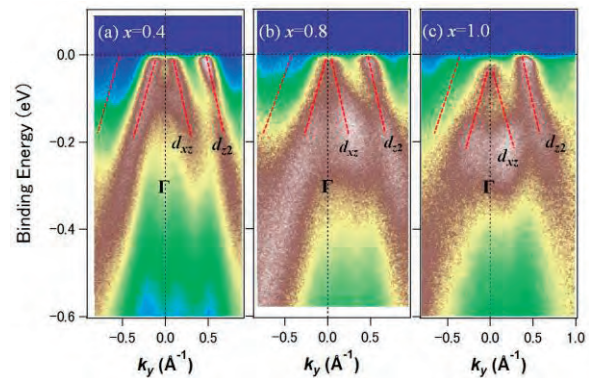


Fig. 1. Band dispersions along  $\Gamma$ -M direction of  $\text{NdFeP}_{1-x}\text{As}_x(\text{O},\text{F})$  with (a)  $x=0.4$ , (b)  $0.8$  and (c)  $1.0$  by the  $P$ -polarization configuration measurement. [4] The broken red lines are guide for eyes and indicate the bands with  $d_{xz}$  and  $d_z^2$  orbital characters around  $\Gamma$  point.

[1] S. Miyasaka *et al.*, J. Phys. Soc. Jpn. **82** (2013) 124706.

[2] K. T. Lai *et al.*, Phys. Rev. B **90** (2014) 064504.

[3] A. Takemori *et al.*, JPS Conf. Proc. **1** (2014) 012111.

[4] Y. Zhang *et al.*, Phys. Rev. B **83** (2011) 054510.

BL7U

## Polarization Dependent ARPES Study on Iron-Based Superconductor $K_xFe_{2-y}Se_2$

M. Sunagawa<sup>1</sup>, K. Terashima<sup>1,2</sup>, M. Tanaka<sup>3</sup>, H. Takeya<sup>3</sup>, Y. Takano<sup>3</sup>,  
K. Suzuki<sup>4</sup>, H. Usui<sup>4</sup>, K. Kuroki<sup>4</sup>, T. Wakita<sup>1,2</sup>, Y. Muraoka<sup>1,2</sup> and T. Yokoya<sup>1,2</sup>

<sup>1</sup>The Graduate School of Natural Science and Technology and Research Laboratory for Surface Science, Okayama University, Okayama 700-8530, Japan

<sup>2</sup>Research Center of New Functional Materials for Energy Production, Storage, and Transport, Okayama University, Okayama 700-8530, Japan

<sup>3</sup>National Institute for Material Science, Tsukuba 305-0047, Japan

<sup>4</sup>Department of Physics, Osaka University, Toyonaka 560-0043, Japan

An accurate description of the overall electronic structure is extremely important for understanding the mechanism of superconductivity. For iron-arsenide superconductors, their Fermi surface (FS) topology consists of hole- and electron-like FSs at the Brillouin zone center and corner, respectively. Theoretical studies based on weak-coupling approach have proposed that spin fluctuations arising from the FS nesting can realize a  $s_{\pm}$  superconducting state [1,2]. A nearly isotropic  $s$ -wave superconducting gap and a spin resonance peak at the nesting vector measured by ARPES and neutron scattering measurements [3,4], respectively, are consistent with the  $s_{\pm}$  superconducting state.

However, this theory has faced a serious challenge ever since the discovery of alkali-metal doped iron-selenide superconductors (AFS), where only electron-like FSs with nodeless superconducting gap have been observed by ARPES [5-7]. These results are not consistent with the  $d$ -wave symmetry expected by some of weak-coupling theories [8-10]. Therefore, it remains open whether the weak-coupling theories are suitable for explaining the superconductivity in AFS.

The low-lying electronic structure in iron-based materials consists of multi-band with different orbital character. Due to the photoemission selection rule, the spectral intensity of the bands exhibits photon polarization dependence. Moreover, in several iron-based superconductors, it has been reported that the strength of band intensity also depends on the excitation photon energy. So, there is a possibility that a hole-like FS actually exists and has eluded previous ARPES experiments because of the significant photon polarization and/or photon energy dependence of spectral intensity. Previously, we performed ARPES measurements with careful tuning of photon energy and photon polarization on a high quality single crystal of  $K_{0.62}Fe_{1.7}Se_2$  [11], and we succeeded to observe a hole-like band with approaching  $E_F$  in two different momentum regions around the  $\Gamma$  point, suggesting the possible presence of a hole-like FS in  $K_xFe_{2-y}Se_2$  [12].

In the present research, we performed the temperature-dependent ARPES study on  $K_xFe_{2-y}Se_2$

with tuning the photon polarization at BL-7U of UVSOR, and confirmed the reproducibility of the observation of the hole-like band, as shown in Fig 1.

We acknowledge M. Matsunami and K. Tanaka for technical assistance in this photoemission experiment.

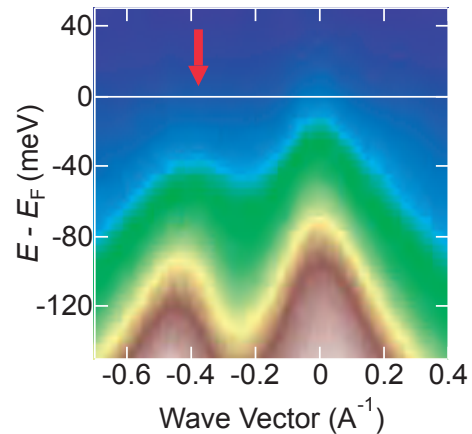


Fig. 1. ARPES  $E$ - $k$  map along  $\Gamma$ -X line taken with p-polarized 23 eV photon at  $T = 80$  K. In Fig.1, red arrow indicates the new hole-like band.

- [1] I. I. Mazin *et al.*, Phys. Rev. Lett. **101** (2008) 057003.
- [2] K. Kuroki *et al.*, Phys. Rev. Lett. **101** (2008) 087004.
- [3] P. Richard *et al.*, Rep. Prog. Phys. **74** (2011) 124512.
- [4] A. D. Christianson *et al.* Nature **456** (2008) 930.
- [5] M. Xu *et al.*, Phys. Rev. B **85** (2012) 220504.
- [6] D. Mou *et al.*, Phys. Rev. Lett. **106** (2011) 107001.
- [7] X. -P. Wang *et al.*, Europhys. Lett. **99** (2012) 67001.
- [8] I. I. Mazin, Phys. Rev. B **84** (2011) 02459.
- [9] M. Khodas *et al.*, Phys. Rev. Lett. **108** (2012) 247003.
- [10] A. Kreisel *et al.*, Phys. Rev. B **88** (2013) 094522.
- [11] T. Ozaki *et al.*, Europhys. Lett. **98** (2012) 27002.
- [12] M. Sunagawa *et al.*, submitted.

BL7U

## CD-ARPES Studies on Rashba & Dresselhaus Effects

W. Jung<sup>1</sup>, S. Cho<sup>1</sup>, Y. Kim<sup>1</sup>, B. Kim<sup>1</sup>, J. Seo<sup>1</sup>, J. Kwon<sup>1</sup>, M. Matsunami<sup>2</sup>, K. Tanaka<sup>2</sup>,  
S. R. Park<sup>3</sup> and C. Kim<sup>1</sup>

<sup>1</sup>*Institute of Physics and Applied Physics, Yonsei University, Seoul, Korea*

<sup>2</sup>*Editorial Board, UVSOR Facility, Institute for Molecular Science, Okazaki 444-8585, Japan*

<sup>3</sup>*Department of physics, Incheon National University, Incheon 406-772, Korea*

Semiconductor materials have recently been extensively studied for their spintronic applications. An important example is spin-field-effect transistor (spin-FET) proposed by Datta and Das [1] in light of controllability of spin precession motion of electrons through the Rashba and Dresselhaus spin-orbit coupling effects. [2,3,4]. Based on previous work, orbital angular momentum (OAM) plays a vital role in the Rashba effect. We expect OAM in these materials also has strong influence on the Dresselhaus effect, therefore, in turn on the spintronic properties.

Compound semiconductors such as CdTe and InSb have zinc blende structure with inversion symmetry breaking (ISB) in the bulk. They have three hole bands at the valence band top located at the  $\Gamma$ -point. They are defined as heavy and light hole bands with  $J=3/2$ , and a split off band with  $J = 1/2$ . The energy splitting ( $\Delta$ ) between  $J=3/2$  and  $1/2$  states due to spin-orbit coupling is on the order of hundred meV. To describe the complex spin configuration of these bands, they normally apply Dresselhaus Hamiltonian. However, the conventional Dresselhaus Hamiltonian does not consider OAM. Therefore, we aimed to investigate the OAM configuration in these bands of CdTe by using circular dichroism (CD) ARPES. We also performed density function theory calculation to theoretically study the role of OAM in the Rashba and Dresselhaus effect in these materials.

CdTe single crystals were purchased as wafers. ARPES measurement was performed at the beam line 7U of UVSOR-III. Samples were cleaved in situ at room temperature and the chamber pressure was better than  $5 \times 10^{-11}$  Torr. ARPES spectra were acquired with a hemispherical photoelectron analyzer (MBS A-1). We used horizontally polarized as well as left- and right-circularly polarized (LCP and RCP) light.

The dispersion of heavy and light hole bands are clearly seen in  $\Gamma$ -X high symmetry cut data taken by horizontal polarized light with 24 eV photon energy as shown in Fig. 1a. Figure 1b is the CD-pattern. The CD-pattern is defined as the subtraction data from RCP and LCP (RCP-LCP). The dotted black line is a guide to the eye, indicating the dispersion of the light hole band. We can only confirm the CD-pattern of light hole band because the heavy hole band is not clearly seen in low photon energy region. The CD-pattern of light hole band seems to have mirror-symmetry breaking about the  $\Gamma$ -point.

The above observation means that the OAM has

similar textures to the spin textures of Dresselhaus type, implying the existence of OAM in this system. It also implies that OAM plays an important role in the Dresselhaus effect. To confirm more precise OAM texture, we will obtain the energy constant contour data using CD-ARPES.

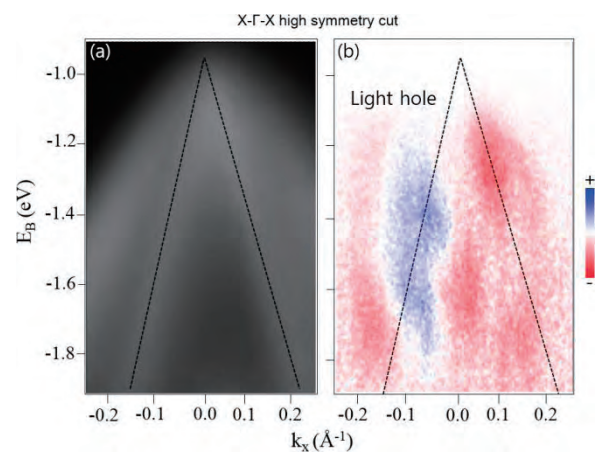


Fig. 1. ARPES results from CdTe (110) bulk state measured with 24 eV photon (a) and CD pattern of one with 9.75 eV (b) at the  $\Gamma$ -point.

- [1] S. Datta *et al.*, Appl. Phys. Lett. **56** (1990) 665.
- [2] Y. A. Bychkov *et al.*, JETP Lett. **39** (1984) 78.
- [3] J. Schliemann *et al.*, PRL. **90** (2003) 146801.
- [4] X. Cartoixà, D *et al.*, APL. **83** (2003) 1462.
- [5] S. R. Park *et al.*, PRL **107** (2011) 156803.
- [6] B. Y. Kim *et al.*, PRB **85** (2012) 195402.

BL7B

## Electronic Structures and Reflectance Spectra of AZnF<sub>3</sub> (A=Na, K, Rb) Single Crystals

S. Ishii<sup>1</sup>, S. Tanaka<sup>1</sup>, A. Yamaji<sup>2</sup>, S. Tanaka<sup>3</sup>, S. Kurosawa<sup>2,4</sup>, S. Watanabe<sup>5</sup>, M. Kitaura<sup>1</sup>, A. Ohnishi<sup>1</sup> and M. Sasaki<sup>1</sup>

<sup>1</sup>Department of Physics, Faculty of Science, Yamagata University, Yamagata 990-8560, Japan

<sup>2</sup>Institute for Materials Research, Tohoku University, Sendai 980-8577, Japan

<sup>3</sup>Department of Electric and Electronic Engineering, Faculty of Science and Engineering, Kinki University, Higashi-Osaka 577-8502, Japan

<sup>4</sup>New Industry Creation Hatchery Center, Tohoku University, Sendai 980-8579, Japan

<sup>5</sup>Department of Materials, Physics and Energy Engineering, Graduate School of Engineering, Nagoya University, Nagoya 464-8063, Japan

Studies on Auger-free luminescence (AFL) are of importance in both sides of basic science and industrial application. In this viewpoint, we have looked for new types of AFL materials so far [1, 2]. The present study is an extension of such previous studies; the possibility of AFL in AZnF<sub>3</sub> (A=Na, K, Rb) crystals has been investigated by measurements of reflection and x-ray photoelectron spectroscopy (xps) spectra.

The crystals of NaZnF<sub>3</sub>, KZnF<sub>3</sub>, and RbZnF<sub>3</sub> were grown from melt by a micro puling-down method. Reflectance spectra of NaZnF<sub>3</sub>, KZnF<sub>3</sub>, and RbZnF<sub>3</sub> crystals are shown in Figs. 1(a)-1(c), respectively. These data were measured at 8 K. The lowest energy reflectance peak due to excitonic transition locates around 10 eV. Since the peak position is independent of alkali metals, it is likely that such excitonic transition occurs by F 2*p* → Zn 4*s* transitions. The reflectance spectrum of NaZnF<sub>3</sub> is structureless in the energy region above 10 eV, and is different from the reflectance spectra of KZnF<sub>3</sub> and RbZnF<sub>3</sub>. According to Ref. 3, the outermost core bands of NaZnF<sub>3</sub>, KZnF<sub>3</sub>, and RbZnF<sub>3</sub> are mainly of alkali *p* orbitals. The binding energies are estimated to be 25, 12, and 9 eV, respectively. In NaZnF<sub>3</sub>, the electronic transition from the outermost core band does not occur in the energy region below 30 eV, and thus the reflectance spectrum exhibits only tail. In KZnF<sub>3</sub> and RbZnF<sub>3</sub>, the transitions from outermost core bands are observed as many peaks in the reflectance spectra.

There is a general rule on the occurrence of AFL. It is observed in the case that the band gap energy is larger than the energy difference between the valence band top and the outermost core band top. This rule is satisfied in KZnF<sub>3</sub>. Although KZnF<sub>3</sub> is expected to be an AFL material, AFL has not yet been found at present.

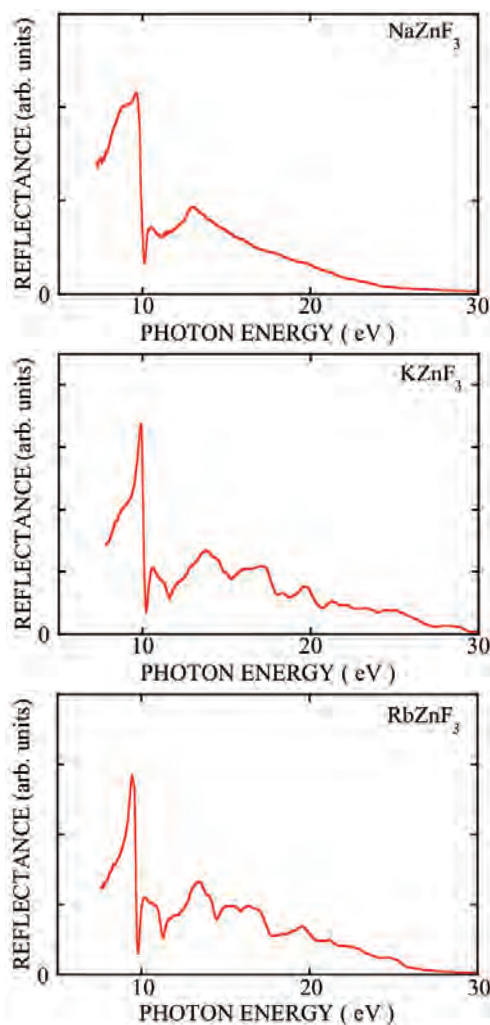


Fig. 1. Reflectance spectra of NaZnF<sub>3</sub> (upper), KZnF<sub>3</sub> (middle), RbZnF<sub>3</sub> (lower) single crystals measured at 8 K.

[1] A. Ohnishi *et al.*, J. Lumi. **132** (2012) 2639.

[2] M. Kitaura *et al.*, Phys. Status Solidi C **10** (2008) 993.

[3] J. F. Moulder, W. F. Stickle, P. E. Sobol and K. D. Bomben, *Hand- book of X-Ray Photoelectron Spectroscopy*, edited by J. Chastain Perkin-Elmer Corporation, Eden Prairie, MN, 1992.

BL7B

## Luminescence and Scintillation Properties of CdF<sub>2</sub> Crystal

T. Yanagida<sup>1,2</sup>, Y. Fujimoto<sup>2</sup>, M. Koshimizu<sup>2</sup> and K. Fukuda<sup>3</sup>

<sup>1</sup>*Kyushu Institute of Technology, Fukuoka 808-0196, Japan*

<sup>2</sup>*Department of Applied Chemistry, Graduate School of Engineering, Tohoku University, Sendai 980-8579, Japan*

<sup>3</sup>*Tokuyama Corp., Shunan 745-8648 Japan*

Auger-free luminescence (AFL) is a luminescence process in which a valence electron radiatively recombine with an outermost core hole. Typical decay time constant of the AFL is subnanosecond or on the order of nanoseconds. Owing to the fast decay, insulator crystals exhibiting the AFL is often used as fast scintillators. The AFL has been observed in various insulators, mainly halide crystals.

Among the halide crystals, the occurrence of the AFL was predicted in CdF<sub>2</sub> [1]. Scintillation properties of CdF<sub>2</sub> crystals have been reported in several papers [2-4]. Fast scintillation components has been observed, however, the ascription of these components to the AFL is not conclusive. In this report, the luminescence and scintillation properties of a single crystal of CdF<sub>2</sub>, with an emphasis on the luminescence properties under vacuum ultraviolet (VUV) photon irradiation.

Single crystal of CdF<sub>2</sub> was grown by Tokuyama Corp. The luminescence and excitation spectra of CdF<sub>2</sub> was obtained by using VUV light as an excitation source at BL7B, UVSOR. Temporal profiles of photoluminescence was obtained at UVSOR operated in a single bunch mode. Radioluminescence (RL) spectrum was obtained under X-ray irradiation. Temporal profile of scintillation was obtained by a single photon counting technique using a pulsed X-ray as an excitation source.

Figure 1 shows the RL spectrum. We observed a prominent band at 420 nm and a shoulder at ca. 350 nm.

Figure 2 shows the excitation spectra monitored at 350 nm. The excitation band maxima were located between 200 and 300 nm. This is also the case for the monitoring wavelength of 420 nm. Taking into account the band gap energy, this excitation band is judged to be located within the band gap. In addition, the band was hardly observed under VUV irradiation.

Figure 3 shows the temporal profile of luminescence at 420 nm. A fast component was observed. The fast components in scintillation can be ascribed to this luminescence component.

The results mentioned above indicate that the fast scintillation component in CdF<sub>2</sub> cannot be ascribed to the AFL but to the defects or impurities.

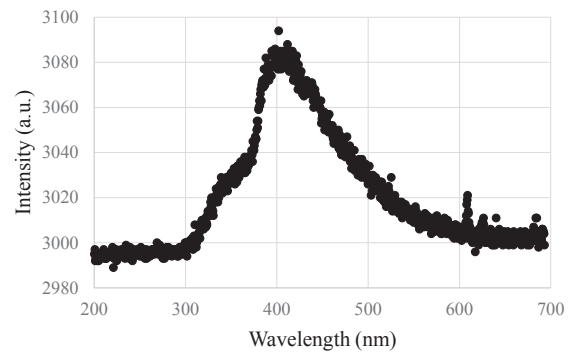


Fig. 1. Radioluminescence spectrum.

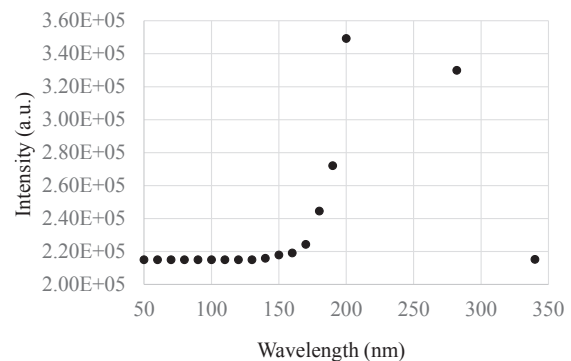


Fig. 2. Excitation spectra monitored at 350 nm.

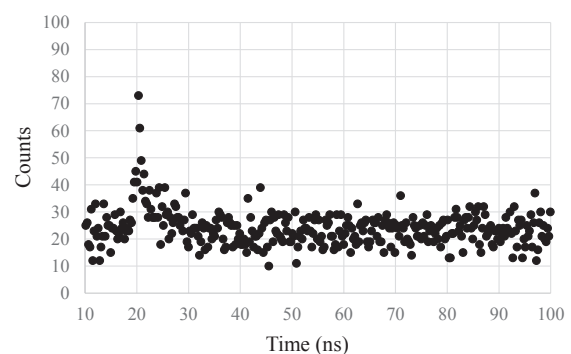


Fig. 3. Temporal profile of luminescence at 420 nm.

[1] J. Andiessen, P. Dorenbos and C. W. E. Van Eijk, *Radiat. Meas.* **24** (1995) 347.

[2] R. V. Jones and J. H. Pollard, *Proc. Phys. Soc.* **79** (1962) 358.

[3] S. E. Derenzo, W. W. Moses, J. L. Cahoon and R. C. C. Perera, *IEEE Trans. Nucl. Sci.* **37** (1990) 203.

[4] E. Radzhabov and R. Shendrik, *IEEE Trans. Nucl. Sci.* **61** (2014) 402.

BL7B

## Reflection Spectra of Ternary Zinc Bismuth Phosphate Glasses in the Ultraviolet Region

N. Kitamura

National Institute of Advanced Industrial Science and Technology, Ikeda 563-8577, Japan

Bismuth phosphate glasses, which have high refractive index and low deformation temperature, are candidate materials for producing high performance optical components such as compact lenses and diffractive optics. It is of interest that a zinc bismuth phosphate glass system has two distinct glass-forming regions; orthophosphate and isolated phosphate structures are dominant in the region that the atomic ratio O/P is higher than 3.5 and metaphosphate and pyrophosphate structures are dominant in the region of O/P < 3.5 [1,2]. We have reported the glass structure and local structure around bismuth ions in a previous work [2,3]. However, the energy level in the glass system is not clear yet. In the present study, reflectivity of the bismuth phosphate glasses has been measured to investigate compositional dependence of the band structure in the vacuum ultraviolet region.

Ternary  $x\text{ZnO}-(30-x/2)\text{Bi}_2\text{O}_3-(70-x/2)\text{P}_2\text{O}_5$  glasses ( $x=10, 20$  and  $30$  mol%) and  $(85-3x/2)\text{ZnO}-x\text{Bi}_2\text{O}_3-(15+x/2)\text{P}_2\text{O}_5$  glasses ( $x=15, 20$  and  $25$  mol%) were prepared by using a conventional liquid-quench method. Nominal chemical compositions are plotted in the glass forming region of the present system as shown in Fig. 1. Reflectivity of optically polished samples was measured in the photon energy region of 4-18 eV with an incident angle of  $10^\circ$  at the BL7B. Figure 2 shows reflection spectra of the binary and un-doped  $x\text{ZnO}-(30-x/2)\text{Bi}_2\text{O}_3-(70-x/2)\text{P}_2\text{O}_5$  glasses. Distinct reflection peak and broad contour were respectively observed at around 5 eV and 6-8 eV. The peak and contour are assigned to the  $6s^2 \rightarrow 6s^1 6p^1$  transition in the  $\text{Bi}^{3+}$  ion [2, 4]. We know that transitions from the ground state ( $^1S_0$ ) to excited states  $^3P_0$  and  $^3P_2$  are spin-forbidden. Therefore, the lower distinct peak is expected to the  $^1S_0 \rightarrow ^3P_1$  transition and the next contour could be due to the  $^1S_0 \rightarrow ^1P_1$  transition. K-K transformed absorption peaks having Gaussian shape have been fitted to these reflection spectra by least square method. The first peak assigned to the  $^1S_0 \rightarrow ^3P_1$  transition was located at 4.9 eV and the position was almost constant in spite of large change in ZnO and  $\text{Bi}_2\text{O}_3$  concentration.

On the other hand, reflection spectra of ternary  $(85-3x/2)\text{ZnO}-x\text{Bi}_2\text{O}_3-(15+x/2)\text{P}_2\text{O}_5$  glasses are shown in Fig. 3. The first peaks located around 4.2 eV and shifted toward lower energy side with the increase of ZnO content. In the previous work [5], we have found that the fraction of the Bi-O bond having short length in  $\text{BiO}_6$  polyhedra increased with increasing ZnO content. The low energy shift of the first band might be due to the change in local structure around bismuth ions.

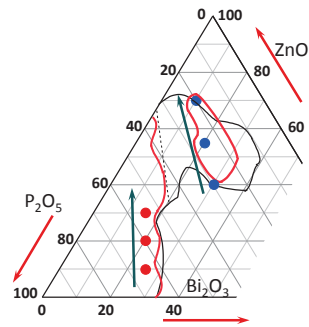


Fig. 1. Glass forming region and chemical compositions of glass of the present system.

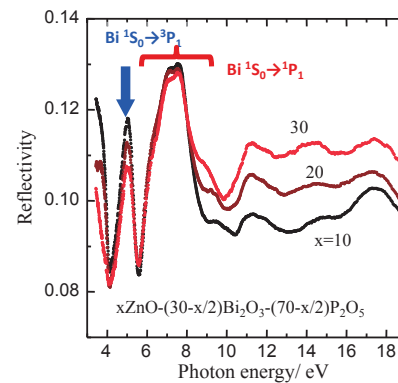


Fig. 2. Reflection spectra of ternary  $x\text{ZnO}-(30-x/2)\text{Bi}_2\text{O}_3-(70-x/2)\text{P}_2\text{O}_5$  glasses.

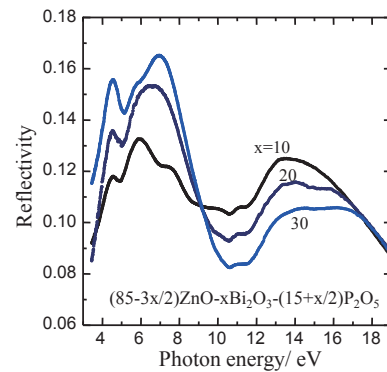


Fig. 3. Reflection spectra of ternary  $(85-3x/2)\text{ZnO}-x\text{Bi}_2\text{O}_3-(15+x/2)\text{P}_2\text{O}_5$  glasses.

[1] B. Elouadi *et al.*, Phase Trans. **13** (1988) 219.  
 [2] N. Kitamura *et al.*, Mater. Sci. Eng. B **161** (2009) 91.  
 [3] N. Kitamura and K. Fukumi, J. Ceram. Soc. Jpn. **121** (2013) 355.  
 [4] G. Blasse and A. Bril, J. Chem. Phys. **48** (1968) 217.  
 [5] N. Kitamura, *et al.*, 23th International Congress on Glass 2013, in preparation.

BL7B

## Control of Spectral Response Using Compound Fluoride Materials $\text{Ca}_x\text{Sr}_{1-x}\text{F}_2$

S. Otani, H. Ishikawa, M. Yanagihara and S. Ono  
*Nagoya Institute of Technology, Nagoya 466-8555, Japan*

Vacuum ultraviolet (VUV) light source is used in various applications such as surface treatment, optical cleaning of semiconductor substrates and sterilization. Accordingly, the detector for monitoring the light source is also required. Currently, many researchers developed VUV detectors based on oxide, nitride and diamond. However, the detectors require the filters for cutting off deep-UV when being used for monitoring of the light source. On the other hand, our group is proceeding to development of the VUV detectors using fluorides [1, 2]. Some fluorides have extremely wider band gap than oxides and nitrides so that they transmit deep-UV region [3]. Until now, we achieved filterless VUV detectors by applying such fluorides. And spectral response of the detectors varies according to band gap of the material. Therefore, we may realize the detectors possessing arbitrary response region by controlling band gap of the material. Here, we report on controlling band gap of compound fluoride materials  $\text{Ca}_x\text{Sr}_{1-x}\text{F}_2$  and spectral response of filterless VUV photoconductive detectors.

$\text{Ca}_x\text{Sr}_{1-x}\text{F}_2$  crystals were grown by Bridgman method and they were controlled composition ratio as  $\text{Ca}_{0.85}\text{Sr}_{0.15}\text{F}_2$  and  $\text{Ca}_{0.5}\text{Sr}_{0.5}\text{F}_2$ . The transmission spectrum of  $\text{Ca}_x\text{Sr}_{1-x}\text{F}_2$  crystals was measured in beamline BL7B at the UVSOR facility. Absorption coefficient was calculated by measuring transmission spectrum of UV region, as shown in Fig. 1. Herewith, band gaps of  $\text{Ca}_{0.85}\text{Sr}_{0.15}\text{F}_2$  and  $\text{Ca}_{0.5}\text{Sr}_{0.5}\text{F}_2$  were calculated as 10.09 eV and 9.93 eV, respectively. Therefore, band gap of  $\text{Ca}_x\text{Sr}_{1-x}\text{F}_2$  is expanded by increasing composition ratio of  $\text{CaF}_2$  in the crystals.

Filterless VUV photoconductive detectors were fabricated by depositing a pair of interdigitated aluminum electrodes on the crystals. Spectral responses of the detectors were also measured in beamline BL7B at the UVSOR facility. The detectors of  $\text{Ca}_{0.85}\text{Sr}_{0.15}\text{F}_2$  and  $\text{Ca}_{0.5}\text{Sr}_{0.5}\text{F}_2$  responded until below 151 nm and 156 nm, respectively. The result shows the response region of the detectors shift to the short-wavelength by expanding band gap of the crystals.

In summary, we found capable of controlling the size of band gap of  $\text{Ca}_x\text{Sr}_{1-x}\text{F}_2$  crystals. Additionally, the spectral response change of filterless VUV photoconductive detectors was observed by using  $\text{Ca}_x\text{Sr}_{1-x}\text{F}_2$  crystals.

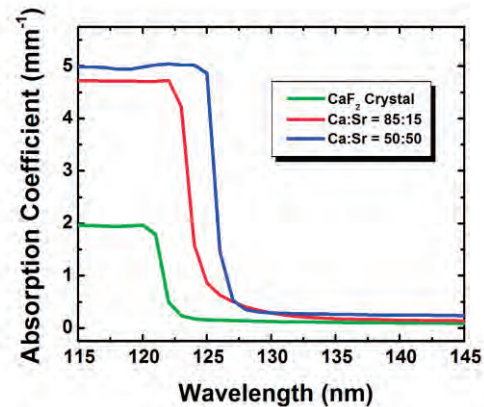


Fig. 1. Transmission spectrum of  $\text{Ca}_x\text{Sr}_{1-x}\text{F}_2$  crystals.

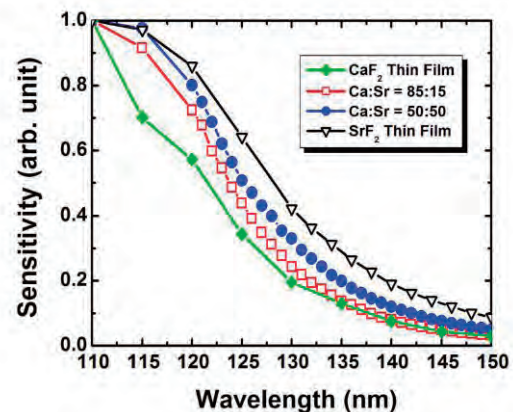


Fig. 2. Spectral responses of the detectors using  $\text{Ca}_x\text{Sr}_{1-x}\text{F}_2$ .

- [1] M. Ieda, T. Ishimaru, S. Ono, K. Yamanoi, M. Cadatal, T. Shimizu, N. Sarukura, K. Fukuda, T. Suyama, Y. Yokota, T. Yanagida and A. Yoshikawa, *Jpn. J. Appl. Phys.* **51** (2012) 022603.
- [2] T. Ishimaru, M. Ieda, S. Ono, Y. Yokota, T. Yanagida and A. Yoshikawa, *Thin Solid Films* **534** (2013) 12.
- [3] S. Ono, R. E. Ouenzerfi, A. Quema, H. Murakami, N. Sarukura, T. Nishimatsu, N. Terakubo, H. Mizuseki, Y. Kawazoe, A. Yoshikawa and T. Fukuda, *Jpn. J. Appl. Phys.* **44** (2005) 7285.

BL7B

## Optical Spectroscopy of $\text{Ba}(\text{Fe}_{1-x}\text{Co}_x)_2\text{As}_2$ in Vacuum-Ultraviolet Energy Region

M. Nakajima, S. Miyasaka and S. Tajima

Department of Physics, Osaka University, Toyonaka 560-0043, Japan

Iron-based superconductors show high transition temperatures as high as 55 K, which is the second highest record after copper-oxide high-temperature superconductors, and have attracted much attention.  $\text{BaFe}_2\text{As}_2$  is one of the representative parent compounds of iron-based superconductors and exhibits a magnetostructural phase transition at  $T = 140$  K. With Co substitution for Fe, the magnetostructural order is suppressed and superconductivity emerges. Thus, how the electronic structure evolves with doping (chemical substitution) is one of the most important issues, and the investigation of the electronic structure over wide energy range by the measurements of the reflectivity spectra is essential.

In this beamtime, we measured reflectivity spectra of single-crystalline  $\text{Ba}(\text{Fe}_{1-x}\text{Co}_x)_2\text{As}_2$  ( $x = 0, 0.1,$  and  $0.25$ ) for an energy range from 2 eV to 35 eV at room temperature using BL7B. The measurement was performed for  $x = 0.25$  using the light polarized parallel and perpendicular to FeAs layers (denoted as  $E \perp c$  and  $E // c$ , respectively) and for  $x = 0$  and 0.1 using the light of  $E \perp c$ . Reflectivity measurement in this energy region is necessary to understand the comprehensive electronic structure including valence bands away from the Fermi energy and to obtain reliable optical parameters derived from the Kramers-Kronig transformation for multi-band/orbital systems such as iron-based materials [1] or copper oxides [2], since a number of intraband and interband excitations overlap in the same energy region and extend up to 10 eV or higher.

Figure 1 shows the in-plane reflectivity spectra ( $E \perp c$ ) for  $x = 0, 0.1,$  and  $0.25$ . For all the three compositions, three distinct reflectivity edges are clearly observed at  $< 2, \sim 10,$  and  $\sim 25$  eV. Each edge indicates the end point of a series of intraband or interband excitations. The lowest-energy edge corresponds to the plasma edge of free carriers. In the present energy range, the lower limit of which is  $\sim 2$  eV, only a tail of the edge is seen. With Co doping, an energy showing a dip shifts to a higher energy region, indicating that Co substitution increases electron carrier density. The second edge probably corresponds to the transition from  $\text{As}4s$  to  $\text{Fe}3d$ . A height of a peak at  $\sim 7$  eV decreases with increasing the Co content. This might result from a Lifshitz transition due to electron (Co) doping. The formation of the third edge observed at  $\sim 25$  eV is contributed by the excitations involving all the valence electrons.

Polarization dependence of the reflectivity spectra for  $x = 0.25$  is shown in Fig. 2. An overall feature is

similar, but fine structures are smeared for  $E // c$ , indicating that these structures result from excitations parallel to FeAs layers. The most prominent difference is observed for the 7-eV peak. The clearer peak for  $E \perp c$  implies that the in-plane response is dominant for the transition from  $\text{As}4s$  to  $\text{Fe}3d$ .

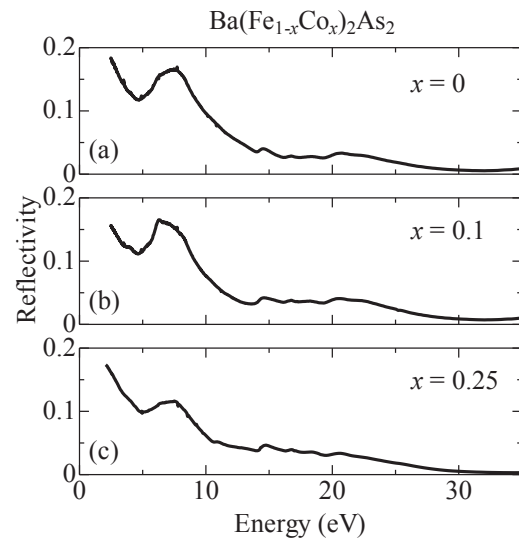


Fig. 1. Reflectivity spectra of  $\text{Ba}(\text{Fe}_{1-x}\text{Co}_x)_2\text{As}_2$  up to 35 eV for (a)  $x = 0$ , (b) 0.1, and (c) 0.25.

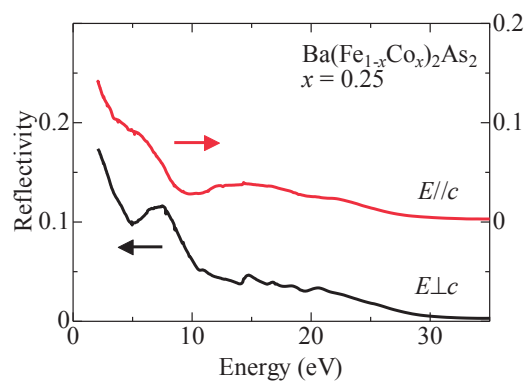


Fig. 2. Reflectivity spectra of  $\text{Ba}(\text{Fe}_{0.75}\text{Co}_{0.25})_2\text{As}_2$  for the polarization parallel and perpendicular to the FeAs layers. The spectrum for  $E // c$  is offset to avoid overlapping.

[1] M. Nakajima *et al.*, Proc. Natl. Acad. Sci. U.S.A. **108** (2011) 12238.

[2] S. Tajima *et al.*, J. Opt. Soc. Am. B **6** (1989) 475.

BL7B

## Influence of Niobium Concentration on the Reflection Spectra for Ternary Niobium Bismuth Phosphate Glasses

N. Kitamura<sup>1</sup>, K. Fukumi<sup>1</sup>, Y. Hisano<sup>2</sup>, N. Hirao<sup>2</sup>, S. Tuji<sup>2</sup>, A. Uchiyama<sup>2</sup> and H. Kozuka<sup>2</sup>

<sup>1</sup>National Institute of Advanced Industrial Science and Technology, Ikeda 563-8577, Japan

<sup>2</sup>Kansai University, Suita 564-8680, Japan

BaO-Nb<sub>2</sub>O<sub>5</sub>-P<sub>2</sub>O<sub>5</sub> glass is one of niobium phosphate glass systems having a wide glass forming region with high Nb<sub>2</sub>O<sub>5</sub> contents<sup>1</sup>. In this system, NbO<sub>x</sub> polyhedra construct glass network structure with PO<sub>4</sub> tetrahedra. Since the glass shows high refractive index due to high niobium concentration. It is of interest for the application to optical glasses in precision optical devices. However, the glass with high niobium content gives yellowish and blue colours and the relationship between optical properties, such as refractive index, dispersion, absorption edge, etc., and structure around niobium ions or connection of niobium-oxygen polyhedra in the network structure are not clear yet. In the present study, reflectivity of the bismuth phosphate glasses has been measured to investigate compositional dependence of the band structure in the vacuum ultraviolet region.

Ternary xNb<sub>2</sub>O<sub>5</sub>-(100-x)Ba(PO<sub>3</sub>)<sub>2</sub> glasses (x=0, 15, 35 and 50 mol%) and ternary xNb<sub>2</sub>O<sub>5</sub>-50BaO-(50-x)P<sub>2</sub>O<sub>5</sub> glasses (x=0, 10, 20 and 30 mol%) were prepared by using a conventional liquid-quench method. Reflectivity of optically polished samples was measured in the photon energy region of 4-25 eV with an incident angle of 10° at the BL7B. Figure 1 shows reflection spectra of the xNb<sub>2</sub>O<sub>5</sub>-(100-x)Ba(PO<sub>3</sub>)<sub>2</sub> glasses. Strong reflection peak was observed at around 9.5 eV and 22 eV, and a weak shoulder at 12-18 eV was observed for the glasses with low Nb<sub>2</sub>O<sub>5</sub> content. The peak are assigned to the transition from O 2p and P 3p states to Nb 4d and Ba 5d states from a report of DFT calculation for barium niobium phosphate compounds [2]. The origin of the higher band at 22 eV is not clear yet. The weak shoulder around 12-18 eV suppressed with increasing Nb<sub>2</sub>O<sub>5</sub> content. Therefore, the shoulder could be due to the Ba 5d state. In a crystal which NbO<sub>6</sub> polyhedra construct chain-like structure, Ba 5d state locates at higher energy side than Nb 5d state [2]. This does not contradict the present results. The 9.5 eV peak became broad with the increase of Nb<sub>2</sub>O<sub>5</sub> content. Low energy shift of absorption edge and yellowish color [3] might be due to the broadening of this band.

On the other hand, reflection spectra of ternary xNb<sub>2</sub>O<sub>5</sub>-50BaO-(50-x)P<sub>2</sub>O<sub>5</sub> glasses are shown in Fig. 2. As shown in the figure, the similar peaks and shoulder were observed. The weak shoulder around 12-18 eV suppressed with increasing Nb<sub>2</sub>O<sub>5</sub> content. The 9.5 eV band broadened with the increase of Nb<sub>2</sub>O<sub>5</sub> content too. The broadening of the 9.5 eV band

might be due to the distortion of NbO<sub>6</sub> polyhedra which was found by Raman, FT-IR and XAFS measurements of these glasses [3].

This work was supported by Nippon Sheet Glass Foundation for Materials Science and Engineering.

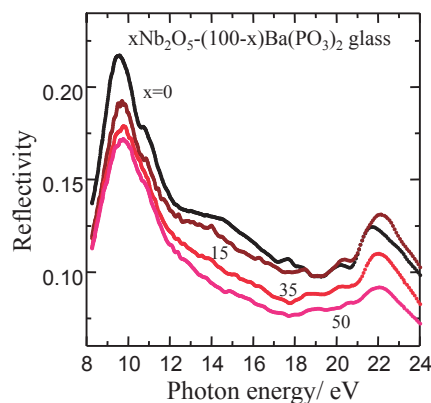


Fig. 1. Reflection spectra of ternary xNb<sub>2</sub>O<sub>5</sub>-(100-x)Ba(PO<sub>3</sub>)<sub>2</sub> glasses.

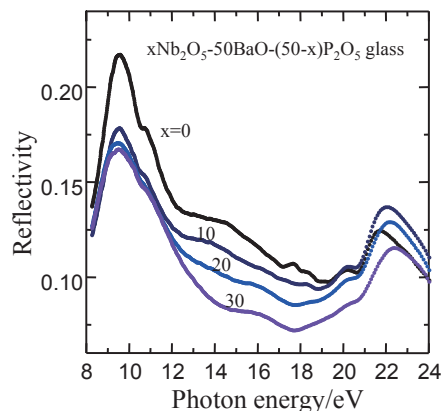


Fig. 2. Reflection spectra of ternary xNb<sub>2</sub>O<sub>5</sub>-50BaO-(50-x)P<sub>2</sub>O<sub>5</sub> glasses.

- [1] N. Shcheglova and T. V. Avlas, *Fiz. Khim. Stekla* **16** (1990) 879.
- [2] I. Cho *et al.*, *Eur. J. Inorg. Chem.* **2011** (2011) 2206.
- [3] N. Kitamura *et al.*, Extended abstract 1st Int. Nat'l. Conf. Phosphate glasses, Pardvice, 2014.

BL8B

## Ultraviolet Photoelectron Spectra of $\text{Ce}_2@C_{80}$ and $\text{La}_2@C_{80}$

T. Miyazaki<sup>1</sup>, S. Okita<sup>1</sup>, T. Ohta<sup>1</sup>, H. Yagi<sup>1</sup>, R. Sumii<sup>2</sup>, H. Okimoto<sup>3</sup>, Y. Ito<sup>3</sup>,  
H. Shinohara<sup>3</sup> and S. Hino<sup>1</sup>

<sup>1</sup>Graduate School of Science and Engineering, Ehime University, Matsuyama 790-8577, Japan

<sup>2</sup>Institutes for Molecular Science, Okazaki 444-858, Japan

<sup>3</sup>Graduate School of Science, Nagoya University, Nagoya 464-8602, Japan

Fullerene cages often encapsulate metal atoms.  $C_{80}$  endohedral fullerenes attract attention because of the reasons such as empty  $I_h-C_{80}$  is not stable and cannot be isolated [1] but it becomes stable upon encapsulation of metal atoms [2]. Early theoretical calculation on  $\text{La}_2@C_{80}$  suggested that entrapped two La atoms rotated in the  $D_{2h}-C_{80}$  cage. Vibrational mode analysis using DFT calculation of  $\text{La}_2@C_{80}$  suggested  $D_{3d}$  symmetry that is the global minimum in total energy.  $\text{Ce}_2@C_{80}$  was isolated and its predicted geometry was not  $D_{2h}$  but  $D_{3d}$ . The reason of  $\text{Ce}_2@C_{80}$  having  $D_{3d}$  geometry was attributed to specific bonding condition of Ce atoms to the cage: they bonded to C atoms on the opposite side of  $C_6$  axis of  $C_{80}$ . We succeeded to measure ultraviolet photoelectron spectra (UPS) of  $\text{La}_2@C_{80}$  and  $\text{Ce}_2@C_{80}$ . In this report their UPS will be presented and they are compared with simulated spectra obtained from DFT calculation.

The UPS were measured using a photoelectron spectrometer at BL8B2 of UVSOR. Energy calibration of the spectra was carried out using the Fermi edge of a gold-deposited sample disk before the UPS measurements of  $\text{La}_2@C_{80}$  and  $\text{Ce}_2@C_{80}$ . Molecular orbitals of  $\text{La}_2@C_{80}$  and  $\text{Ce}_2@C_{80}$  were calculated with a Gaussian 03 program module. Their geometry was optimized at the Hartree-Fock level using the CEP-31G basis set. Simulated spectra generated by broadening the calculated Eigen values at the Hartree-Fock level with Gaussian functions of 0.2 eV full width at half maximum.

Figure 1 shows the UPS of  $\text{La}_2@C_{80}$  and  $\text{Ce}_2@C_{80}$  obtained with  $h\nu = 30\text{eV}$ . The spectral onset of  $\text{La}_2@C_{80}$  and  $\text{Ce}_2@C_{80}$  was 0.77 and 0.89 eV below the Fermi level, respectively. Except for the onset energy, their UPS are almost identical. There are 10 structures labeled A to J in their UPS. Their relative intensity is almost the same. The bars in Fig. 1 indicate the calculated ionization energies (Eigenvalues of occupied states). Scale of the simulated spectra and Kohn-Sham orbital energies is shifted by 4.4 eV for an easy comparison. The simulated spectra generated from  $D_{3d}$  and  $D_{2h}$  geometry seem to reproduce the UPS; the first four structures A – D are well reproduced and deeper structures F – J are also reproduced reasonably well. Only attractive difference in the simulated spectra might be associated with the position of the HOMO; the HOMO of  $\text{Ce}_2@C_{80}$  appears at slightly shallower

than the HOMO-1 or -2, whereas that of  $\text{La}_2@C_{80}$  locates rather close to the HOMO-1. From these data, present findings suggest that the simulated spectra obtained from  $D_{3d}$  geometry reproduced the UPS of  $\text{Ce}_2@C_{80}$  and  $\text{La}_2@C_{80}$  very well.

The UPS of  $\text{La}_2@C_{80}$  are the same as those of  $\text{Ce}_2@C_{80}$ , both have the same electronic structure. Comparison of the UPS with theoretically generated simulation spectra indicates that the most plausible structure of  $\text{Ce}_2@C_{80}$  and  $\text{La}_2@C_{80}$  has  $D_{3d}$  symmetry. Charge population analysis suggests  $\text{Ce}_2^{6+}@C_{80}^{6-}$  and  $\text{La}_2^{6+}@C_{80}^{6-}$  oxidation state.

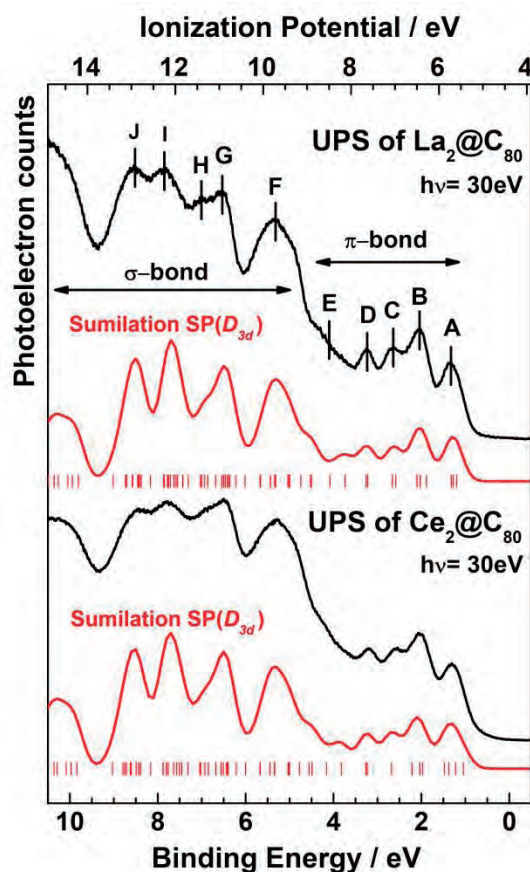


Fig. 1. Simulation spectra from the optimized  $D_{3d}$  structure and ultraviolet photoelectron spectra of  $\text{La}_2@C_{80}$  and  $\text{Ce}_2@C_{80}$ .

[1] F. H. Hennrich, *et al.*, *Angew. Chem. Int. Ed.* **35** (1996) 1732.

[2] M. M. Alvarez, *et al.*, *J. Phys. Chem.* **95** (1991) 10561.